



School of Physical Sciences

NUMERICAL SIMULATIONS OF RESTARTING
RADIO JETS FROM ACTIVE GALACTIC NUCLEI

by

Patrick Yates, B.Sc.

November, 2016

Submitted in fulfilment of the requirements
for the Bachelor of Science with Honours

I declare that this thesis contains no material which has been accepted for a degree or diploma by the University or any other institution, except by way of background information and duly acknowledged in the thesis, and that, to the best of my knowledge and belief, this thesis contains no material previously published or written by another person, except where due acknowledgement is made in the text of the thesis.

Signed: _____
Patrick Yates

Date: _____

This thesis may be made available for loan and limited copying in accordance with the *Copyright Act 1968*

Signed: _____
Patrick Yates

Date: _____

ABSTRACT

Feedback from Active Galactic Nuclei on the host environment is required to maintain the delicate heating/cooling balance in massive galaxies over the latter half of the Hubble time. The process usually invoked is kinetic feedback from radio jets, which do work on their host hot atmospheres through supersonic outflows, shocks and gas uplifting. An open question is whether the efficiency of this feedback mode depends on the jet duty cycle.

I investigated the energetic and morphological effects of different environments and different numbers of jet outbursts. I carried out numerical hydrodynamic simulations of radio jets using the PLUTO simulation code. These radio jets were simulated in both cluster and poor group environments, corresponding to different dark matter halo masses, with a hydrostatic equilibrium gas density profile. In each simulation, the same total energy is injected at the same time-averaged rate (i.e. using the same average jet power), but using a different number of jet outbursts. I quantified the fraction of injected energy that couples to the surrounding gas, and compared AGN feedback efficiencies in different energy injection scenarios. Finally I created mock surface brightness plots of the radio jets in order to look for observational signatures of restarting jets.

ACKNOWLEDGEMENTS

I am grateful for the support of my family, friends and colleagues during my Honours year. I am indebted to my supervisors, Dr. habil Martin Krause and Dr. Stas Shabala, for their help and support throughout the year, as well as their faith in my research and comments on my thesis chapters. I could not have completed this thesis without the support of my partner, Lauren Jones, who encouraged me throughout the year. My family has also been a constant source of support during this year. I would also like to acknowledge the support given to me by my fellow Honours students, as well as PhD students. Finally I would like to thank those who proof-read the final thesis and provided comments, particularly Honor Yearsley, Brian Yates and Jennifer Yates.

Contents

Contents	i
List of Tables	v
List of Figures	vii
1 Introduction	1
1.1 Galaxy Formation and Evolution	1
1.1.1 Cosmology	2
1.1.2 Dark Matter Profile	3
1.1.3 Gas Density Profile	3
1.1.4 AGN Feedback	5
1.2 Observations of Radio Sources	9
1.2.1 FR Classification System	9
1.2.2 Observations	11
1.2.3 Comparing Observations and Simulations	12
1.2.4 Double-Double Radio Galaxies	12
1.3 Models of Astrophysical Jets	14
1.3.1 Analytic/Semi-analytic Jet Models	14
1.3.2 Analytic/Semi-Analytic Bubble Models	16
1.3.3 Numerical Simulations	18
1.4 Simulations of Astrophysical Fluid Flows	20
1.5 A Brief History of Astrophysical Hydrodynamics	21
1.6 Reliability of Numerical Simulations of AGN Jets	22

CONTENTS

1.7	Summary	24
2	Numerical Simulations with PLUTO	25
2.1	Length Scales	26
2.2	Simulation Grid	27
2.2.1	Boundary Conditions	29
2.3	Jet Injection Method	30
2.4	Absence of Magnetic Fields	31
2.5	Restarting the jet	32
2.6	Realistic Gas Density Profiles	33
2.6.1	Concentration Parameter	34
2.6.2	Gas Density Distribution	34
2.7	Jet Parameters	36
2.8	Simulation Times	37
2.9	Simulation Runs	37
3	Radio Jets in Different Environments	45
3.1	Morphology	46
3.1.1	Shocks	47
3.1.2	Hotspot and Backflow	49
3.1.3	Cocoon and Instabilities	50
3.1.4	Jet Evolution	52
3.1.5	Simulation reliability	60
3.2	Energy Components and Distribution	64
3.3	Feedback Efficiency	67
3.4	Surface Brightness	71
3.5	Size-Luminosity Diagram	77
3.6	The King Gas Density Profile	79
3.7	Summary	84
4	Intermittent Radio Jets	87
4.1	Morphology	88

CONTENTS

4.2 Energy Components and Distribution	98
4.3 Feedback Efficiency	98
4.4 Surface Brightness	102
4.5 Size-Luminosity Diagram	106
4.6 Summary	108
5 Conclusions	111
A The Hydrostatic Equilibrium Gas Density Profile	115
B Radio Jets with Two and Three Outbursts	119
BIBLIOGRAPHY	135

List of Tables

2.1	Table of environment parameters	43
2.2	Table of constant parameters	43
2.3	Table of run parameters	44

List of Figures

1.1	Makino gas density profile	6
1.2	Gas density profile with self-gravity	7
1.3	FR I/II division	10
1.4	Radio contour plot of DDRG B 1834+620	13
1.5	Basic radio source morphology	16
1.6	M87 bubbles	17
1.7	Jet parameter convergence	23
1.8	Comparison between experimental results and numerical simulations	24
2.1	Simulation grid	40
2.2	PLUTO grid and ghost zones	41
2.3	Ramp timescale	41
2.4	Concentration parameter models	42
2.5	Makino and King gas density profiles	42
3.1	Density maps of jet in cluster and poor group environments	46
3.2	Pressure maps of jet in cluster and poor group environments	48
3.3	Radial velocity maps of jet in cluster and poor group environments	50
3.4	Azimuthal velocity maps of jet in cluster and poor group environments	51
3.5	Evolution of lobe length for single outburst jet in both a cluster and a poor group environment	52
3.6	Evolution of lobe properties for a single outburst jet in both a cluster and a poor group environment	53
3.7	Evolution of density for single outburst jet in a cluster environment	56

LIST OF FIGURES

3.8	Evolution of density for a single outburst jet in a poor group environment	57
3.9	Evolution of pressure for a single outburst jet in a cluster environment	58
3.10	Evolution of pressure for a single outburst jet in a poor group environment	59
3.11	Resolution study of jet in a constant density environment	61
3.12	Evolution of lobe length for different ramping timescales	62
3.13	Evolution of lobe length for different injection points	63
3.14	Injected energy for the single outburst jet in a cluster environment .	64
3.15	Injected energy for the single outburst jet in a poor group environment	65
3.16	Feedback efficiency for a single outburst jet in both a cluster and a poor group environment	67
3.17	Feedback efficiency for different tracer cutoffs	68
3.18	Surface brightness map for the single outburst jet in a cluster environment	74
3.19	Surface brightness map for the single outburst jet in a poor group environment	75
3.20	Size-luminosity diagram for the single outburst jet in the cluster and poor group environments	78
3.21	Evolution of lobe length for one and four outburst jets, in the King cluster and poor group environments	80
3.22	Evolution of density for the single outburst jet in the King cluster environment	82
3.23	Evolution of density for the single outburst jet in the King poor group environment	83
4.1	Outburst tracer map for the four outburst jet in the cluster environment	88
4.2	Outburst tracer map for the four outburst jet in the poor group environment	89
4.3	Evolution of lobe length for multiple outburst jets in the cluster environment	91
4.4	Evolution of lobe length for multiple outburst jets in the poor group environment	92
4.5	Resolution study for the two outburst jet in the cluster environment	92

LIST OF FIGURES

4.6	Evolution of density for the four outburst jet in the cluster environment	94
4.7	Evolution of density for the four outburst jet in the poor group environment	95
4.8	Evolution of pressure for the four outburst jet in the cluster environment	96
4.9	Evolution of pressure for the four outburst jet in the poor group environment	97
4.10	Injected energy for the four outburst jet in the cluster environment	99
4.11	Injected energy for the four outburst jet in the poor group environment	99
4.12	Feedback efficiency for multiple outbursts jets in the cluster environment	100
4.13	Feedback efficiency for multiple outbursts jets in the poor group environment	101
4.14	Surface brightness maps for multiple outburst jets in the cluster environment	103
4.15	Surface brightness maps for multiple outburst jets in the poor group environment	104
4.16	Size-luminosity diagram for the four outburst jet in both the cluster and poor group environments	106
B.1	Evolution of density for the two outburst jet in the cluster environment	120
B.2	Evolution of pressure for the two outburst jet in the cluster environment	121
B.3	Evolution of density for the three outburst jet in the cluster environment	122
B.4	Evolution of the pressure for the three outburst jet in the cluster environment	123
B.5	Evolution of the density for the two outburst jet in the poor group environment	124
B.6	Evolution of the pressure for the two outburst jet in the poor group environment	125
B.7	Evolution of the density for the three outburst jet in the poor group environment	126
B.8	Evolution of the pressure for the three outburst jet in the poor group environment	127
B.9	Injected energy for the two outburst jet in the cluster	128

LIST OF FIGURES

B.10 Injected energy for the three outburst jet in the cluster	128
B.11 Injected energy for the two outburst jet in the poor group	129
B.12 Injected energy for the three outburst jet in the poor group	129
B.13 Feedback efficiency for the two and three outburst jets in the cluster	130
B.14 Feedback efficiency for the two and three outburst jets in the poor group	131
B.15 Surface brightness maps for the two and three outburst jets in the cluster	132
B.16 Surface brightness maps for the two and three outburst jets in the poor group	133

CHAPTER 1

Introduction

In this chapter I introduce the current view of galaxy formation and evolution in Section 1.1, and then examine observations of radio sources and models of astrophysical jets in Section 1.2 and Section 1.3 respectively. Finally I provide a brief overview of the hydrodynamic equations in Section 1.4, introduce numerical simulation codes in Section 1.5 and examine the reliability of numerical simulations of astrophysical jets in Section 1.6.

1.1 Galaxy Formation and Evolution

I begin with a brief overview of the theory of galaxy formation, looking at it from the viewpoint of semi-analytic modelling. The current cosmological theories are introduced in Section 1.1.1 and the universal density profile of dark matter halos assembled from hierarchical clustering is discussed in Section 1.1.2, which has implications on the distribution of baryonic matter as discussed in Section 1.1.3. Section 1.1.4 introduces Active Galactic Nuclei and the important role these objects play in galaxy formation and evolution.

1.1. GALAXY FORMATION AND EVOLUTION

1.1.1 Cosmology

The cosmological model favoured by the majority of astrophysicists is the Lambda cold dark matter (Λ CDM) variant of the standard model. In this model, dark matter is cold and collisionless, with a mass-energy density fraction of approximately 25%, dark energy, Λ , has a mass-energy density of approximately 70%, while the remaining 5% is baryonic matter. These values of $\Omega_M = 0.3$ for matter density and $\Omega_\Lambda = 0.7$ for energy density give a total density parameter of $\Omega = 1$, indicating the universe is flat. Interested readers are referred to a review by Somerville & Davé (2015, Section 1.2) for a short introduction to cosmology. The first evidence of dark matter was published in Zwicky (1933) (see Zwicky, 2009, English reprint), to account for the velocity dispersions in the Coma galaxy cluster. The observed velocity dispersions of the cluster require a large average density, approximately 400 times larger than the density determined from measurements of the luminosity, suggesting that some form of non-luminous dark matter must be present within the cluster.

Dark matter forms the foundations of the current theory for galaxy formation, originating with White & Rees (1978), wherein a hierarchical model of galaxy formation was proposed. In this model, dark matter clumps hierarchically collapse onto one another to form a self-similar dark matter distribution, which makes up the dominant mass component of the galaxy. The observed sizes, morphologies and luminosities of galaxies are determined by baryonic matter which is condensed and cooled in the centre of the gravitational potential well formed during the hierarchical collapse process. This model produces galaxies with a luminous central region, surrounded by a dark matter halo. The model proposed in White & Rees (1978) was extended in White & Frenk (1991) to analytic methods that could be used to study the properties of galaxies formed using the hierarchical clustering model.

1.1. GALAXY FORMATION AND EVOLUTION

1.1.2 Dark Matter Profile

The structure of dark matter halos formed through hierarchical clustering has been extensively investigated with N-body simulations. The series of papers by Navarro, Frenk & White (Navarro et al., 1994, 1996, 1997), hereafter (NFW1; NFW2; NFW3), were particularly influential in exploring the structure of dark matter halos. In NFW2, Navarro, Frenk & White carry out N-body simulations for dark matter halo masses ranging from $\sim 3 \times 10^{11} M_\odot$ to $\sim 3 \times 10^{15} M_\odot$. They found that the density profiles of CDM halos can be fitted with the function given in Equation (1.1), where $r_s = r_{200}/c$ is the characteristic radius and $\rho_{crit} = 3H(z)^2/8\pi G$ is the critical density of the universe at redshift z . δ_c , given in Equation (1.2) and c are two dimensionless parameters. δ_c is referred to as the characteristic density, while c is the concentration parameter, discussed in more detail in Section 2.6.1.

$$\frac{\rho(r)}{\rho_{crit}} = \frac{\delta_c}{(r/r_s)(1+r/r_s)^2} \quad (1.1)$$

$$\delta_c = \frac{200}{3} \frac{c^3}{(\ln(1+c) - c/(1+c))} \quad (1.2)$$

The authors extended this research in NFW3 to examine a broader range of cosmologies, halo masses and initial density fluctuations. Navarro, Frenk & White found that the shape of the halo density profile is independent of these parameters and that there is always a strong correlation between the halo mass and characteristic density. This suggests that in their simulations, halos formed through a hierarchical clustering process have a universal density profile, the Navarro-Frenk-White (NFW) profile, given by Equation (1.1).

1.1.3 Gas Density Profile

The universal density profile for a dark matter halo given in Navarro et al. (1997) was used by Makino et al. (1998) to derive an analytic density profile for the hot

1.1. GALAXY FORMATION AND EVOLUTION

gas in a cluster, under the assumption that this gas was in hydrostatic equilibrium with the gravitational potential derived from the dark matter halo. The steps for solving the hydrostatic equilibrium equation of an isothermal gas cloud with temperature T_x as shown in Equation (1.3) are given in Appendix A.

$$\frac{kT_x}{\mu m_p} \frac{d \ln \rho_g}{dr} = -\frac{GM(r)}{r^2} \quad (1.3)$$

The resulting profile, Equation (1.4), produces a similar distribution to the isothermal β -model shown in Equation (1.5) which is able to approximate the gas density profile of X-ray clusters well, despite being purely empirical (Cavaliere & Fusco-Femiano, 1978; Vikhlinin et al., 2006). Figure 1.1 shows the shape of both the hot gas density profile and the universal dark matter halo profile. This approach was extended in Suto et al. (1998) to a more general framework for calculating the dark matter halo shape from the X-ray surface brightness profile.

$$\rho_g(r) = \rho_{g0} \exp \left\{ -\frac{27}{2} b \left[1 - \frac{\ln(1 + r/r_s)}{r/r_s} \right] \right\} \quad (1.4)$$

$$n_g(r) = \frac{n_{g0}}{[1 + (r/r_c)^2]^{3\beta/2}} \quad (1.5)$$

The derivation of the hot gas density profile made the assumption that the gas is isothermal, which is a good approximation, and is in fact the theoretically expected result due to the short timescale of thermal conduction. Another assumption made is that the self-gravity of the gas could be neglected, and so the only contribution to the gravitational potential was the mass of the dark matter halo. Neglecting self-gravity is found to be a reasonable assumption to make, as shown in Figure 1.2, taken from Suto et al. (1998). In Figure 1.2, B is $27b/2$, where b is defined in Equation (1.6), while R is the gas fraction, $R \equiv \rho_{g0}/(\delta_c \rho_{c0})$. The scaling parameter b changes steepness of the resulting gas density profile, as shown in Figure 1.1. Suto et al. (1998) showed that $(B, R) = (10, 5)$ and $(5, 1)$ are realistic values for the observed baryon fraction of clusters. In these regions, the self-gravity of the gas

1.1. GALAXY FORMATION AND EVOLUTION

is only slightly relevant and neglecting self-gravity does not produce significantly different results.

$$b(M) \equiv \frac{8\pi G \mu m_p \delta_c(M) \rho_{c0} r_s^2}{27kT_X} \quad (1.6)$$

One final consideration when computing the hot gas density profile from the dark matter halo distribution is the mass of stars. Neglecting the gravitational effects of stars can lead to underestimating hot gas mass by up to 65%, as shown in Capelo et al. (2010). Interestingly, the authors note that for increasingly large stellar mass fractions, the β -model is no longer able to reproduce the correct solution. This indicates that observed surface brightness profiles of galaxies that are found to be fitted by a β -model cannot have a stellar mass fraction much greater than 10%. The β -model becomes an increasingly bad approximation for poor environments (e.g. with a halo mass of less than $10^{13} M_\odot$) where the stellar mass fraction can be significantly higher than 10% as shown in McGaugh et al. (2010, Figure 2) and Giodini et al. (2009, Figure 5).

1.1.4 AGN Feedback

Every active galactic nuclei is powered by a supermassive black hole at the centre, see Soltan (1982). It is well accepted that outflows from AGN play some role in slowing cooling flows via heating (Alexander & Hickox, 2012; Fabian, 2012; Omma et al., 2004). Fabian (2012) provides a recent review of AGN feedback, including the two different modes that current research considers to be important, the radiative and kinetic modes. The kinetic mode is thought to involve heating of the gas via jet outflows from the AGN located at the core. These jets are generated from the accretion flow onto the black hole, and then do work on the surrounding gas as they inflate large cocoons. Theoretically the energy provided by the jets is more than enough to suppress cooling, however the details in how the jet energy couples to the environment is still an open problem. A standard approach in semi-analytic galaxy formation models is to calculate the “cooling luminosity” and offset it using

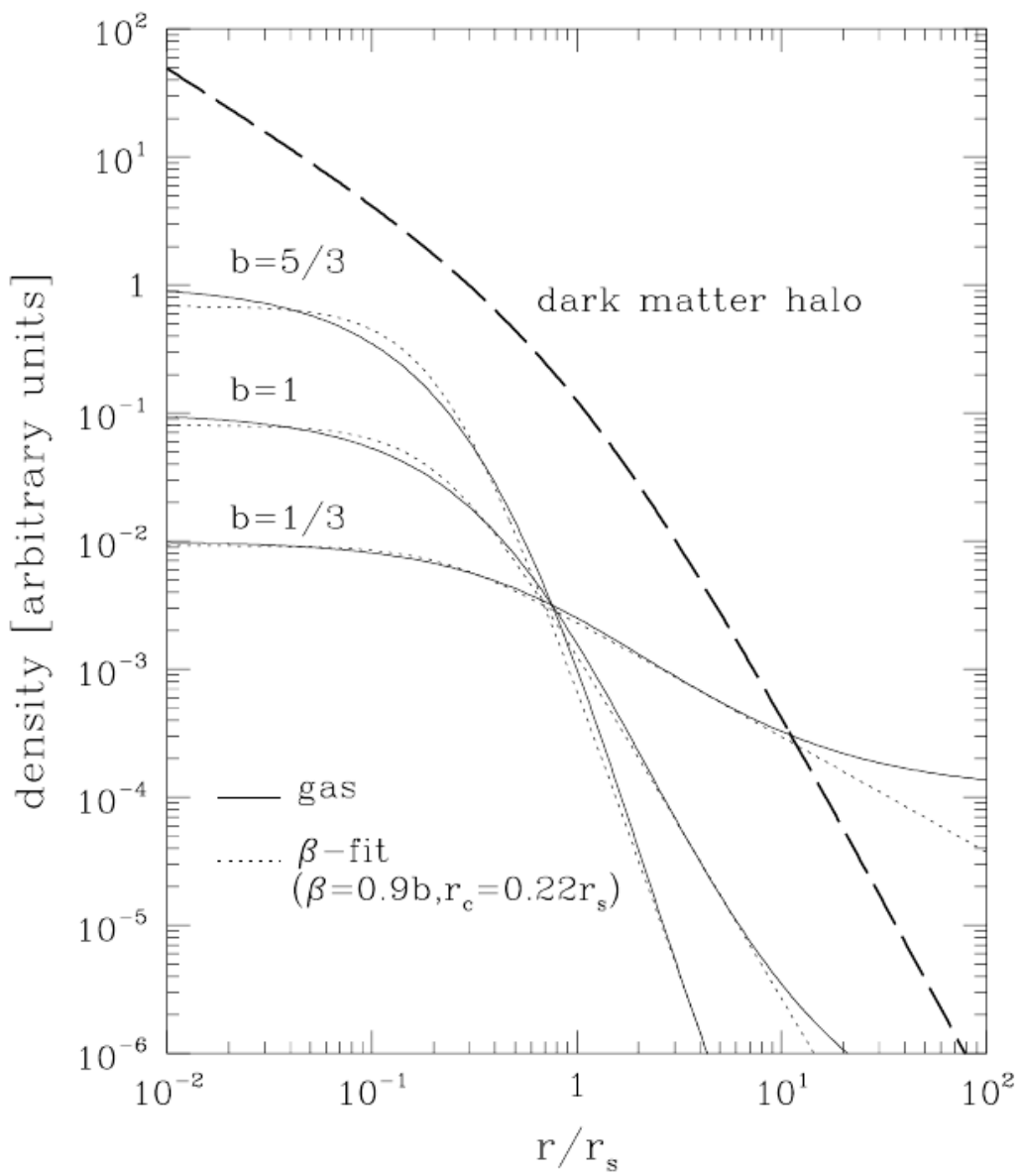


Figure 1.1: Makino gas density profile (solid lines), dark matter halo density profile (dashed line) and best-fit β -models (dotted lines). Credit: Makino et al. (1998, Figure 1)

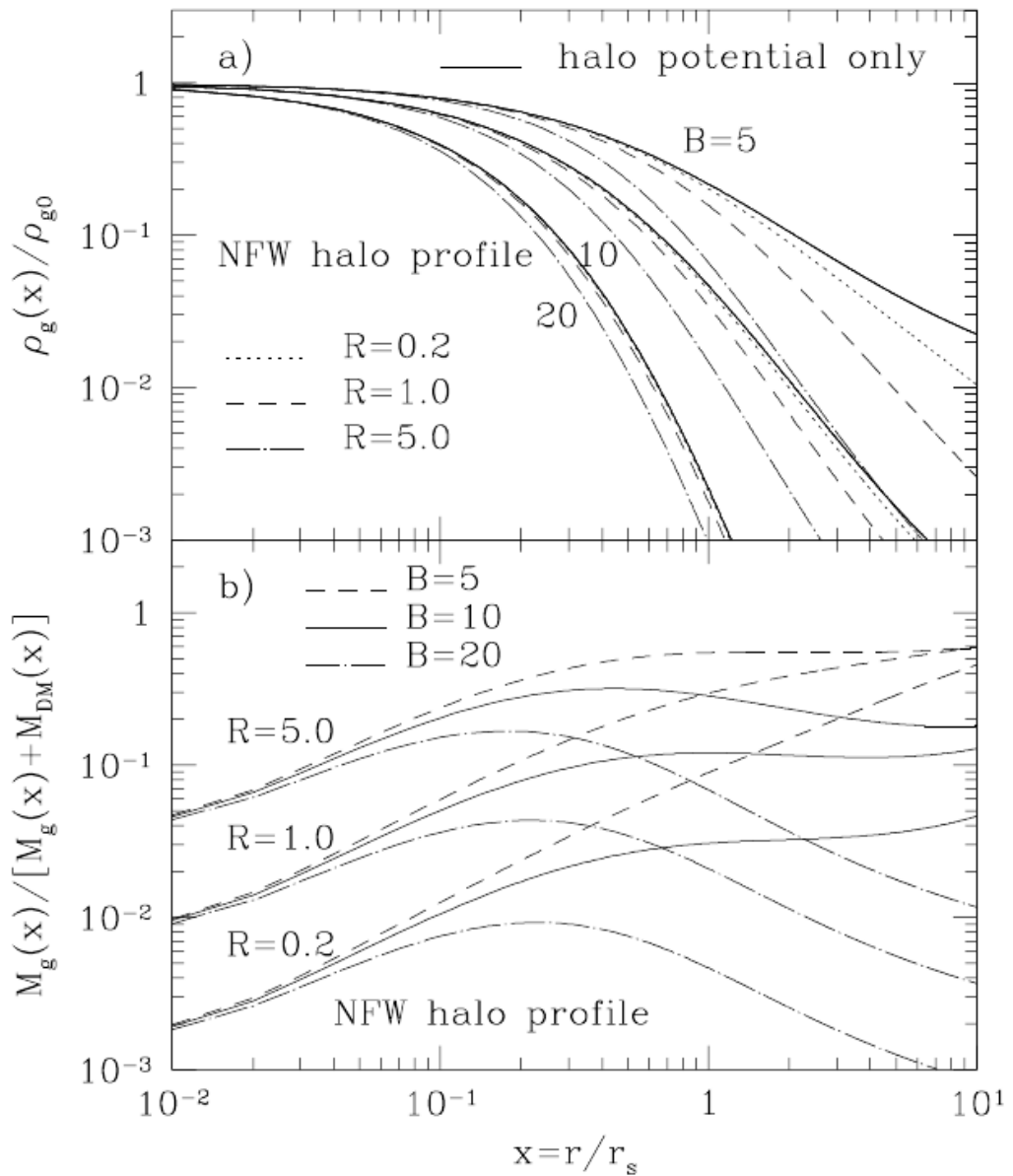


Figure 1.2: Top: Gas density profile with self-gravity. Bottom: Gas mass fraction. Credit: Suto et al. (1998, Figure 4)

1.1. GALAXY FORMATION AND EVOLUTION

the AGN luminosity, see e.g. Croton et al. (2006). These models are very efficient at largely truncating cooling within the cooling radius, however prescriptions of coupling the energy to the gas are very primitive. As found in Omma et al. (2004), a large portion of the jet energy is deposited beyond the cooling radius.

The heating/cooling balance of the AGN is debated (Fabian, 2012), with the simplest solution being that as the gas starts to cool the accretion rate increases, thus fuelling the jet. Similarly, as the jet strips the core of cold gas with its outflow, the accretion rate decreases and the jet runs out of fuel and stops. This simple solution assumes the accretion rate is given by standard Bondi accretion, which is a spherical accretion model first calculated by Bondi (1952). The Bondi accretion model gives an accretion rate of $\dot{M} = 4\pi\lambda(GM_{\text{BH}})^2\rho/c_s^3$ for a uniform gas density ρ and pressure, where c_s is the sound speed, G is the gravitational constant and M_{BH} is the black hole mass. Problems with this simplistic view include the excessively large lengthscales and timescales involved in the accretion process, which means that the required response in AGN activity due to changes in environment needed to preserve the heating/cooling balance would be delayed (Heckman & Best, 2014). A possible alternative accretion method is cold clump accretion which occurs on a much faster timescale. This allows the AGN to react to changes in the environment quicker to better maintain the heating/cooling balance. There is observational evidence that the heating/cooling balance is indeed maintained, see e.g. Best et al. (2007) and Cattaneo et al. (2009).

AGN feedback can have both positive and negative effects on star formation. The Centaurus A galaxy is a well-studied example of positive AGN feedback on the rate of star formation. Oosterloo & Morganti (2004) found that a large H I filament located 15 kpc from the centre of the galaxy showed evidence of interaction with the nearby radio jet, and that regions downstream of the interaction are star forming. Another filament located 8.5 kpc from the centre of Centaurus A was observed by Crockett et al. (2012), who found a significant population of newly formed stars along the tip of the filament. These authors proposed that the population of newly formed stars was due to weak bow shocks driven through the interstellar medium

1.2. OBSERVATIONS OF RADIO SOURCES

by the radio jet, which compresses the gas and triggers star formation.

On the negative feedback side, Tortora et al. (2009) used numerical simulations of a jet propagating through the interstellar medium to show that the star formation rate is initially enhanced, before being quenched. The negative effect of AGN feedback on star formation has been observed in Carniani et al. (2016). While statistically the sample size is small (only 4 quasars as of that paper), the star formation rates (traced using the narrow H α emission line) are significantly spatially anti-correlated with the outflow. However it is noted that the quasar outflows do not affect the entire galaxy, and it is possible they could increase star formation at the edges of the outflow cone due to compression of the gas. There is evidence for both positive and negative AGN feedback with respect to star formation, and the topic of AGN feedback as a whole is complex.

1.2 Observations of Radio Sources

Observations of radio sources and their interaction with the environment provide important constraints on the physics of feedback processes. In Section 1.2.1, I describe the morphologies of radio AGN, and introduce the Fanaroff-Riley morphological classification system, and then show how this classification system has been used along with observations of radio sources to link theoretical models to the underlying physical processes in Section 1.2.2. I introduce the reproduction of basic observed jet features with numerical simulations in Section 1.2.3 and then examine observational evidence for restarting jets in Section 1.2.4.

1.2.1 FR Classification System

Extragalactic radio jets are classified into two categories, according to their morphology (Fanaroff & Riley, 1974). FR I radio sources have hotspots close to the host galaxy, and exhibit a flaring profile, with emissivity decreasing with distance from the central engine. FR II radio sources terminate in hotspots that are usually

1.2. OBSERVATIONS OF RADIO SOURCES

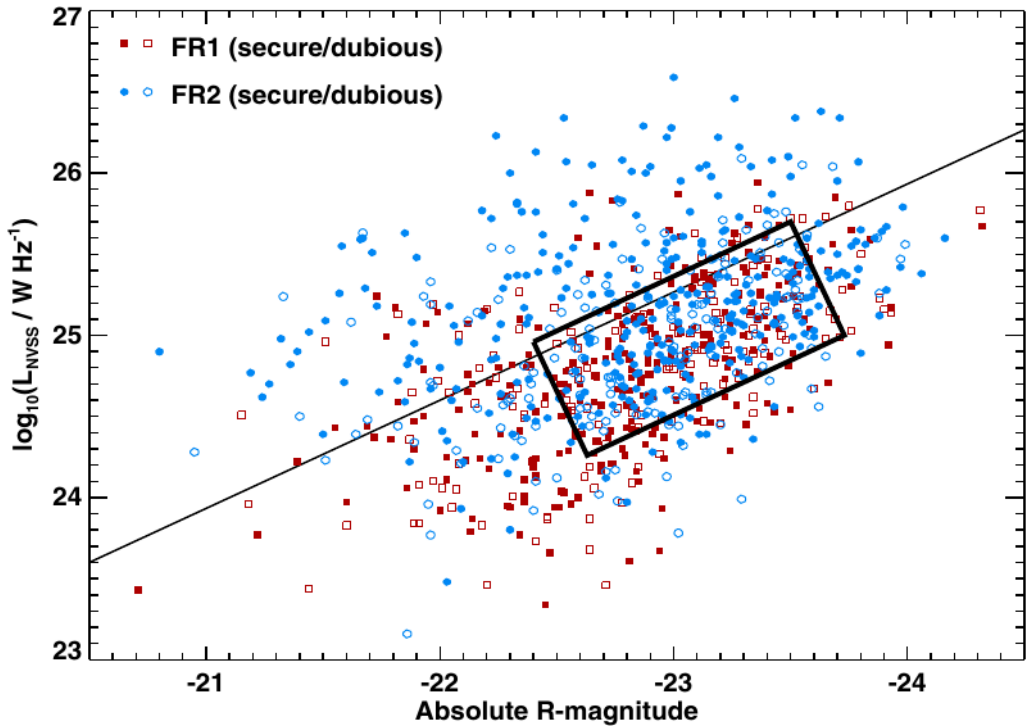


Figure 1.3: A recreation of the Owen & Ledlow (1994) plot for the SDSS radio sources. The square box outlines the "transition region", while the diagonal line is supposed to divide FR I radio sources from FR II radio sources, as in Owen & Ledlow (1994). Credit: Best (2009, Figure 4a)

a few hundred kiloparsecs from the centre of the host galaxy. Owen & Ledlow (1994) claimed that FR I sources are generally less luminous than FR II sources by looking at a large sample of radio sources from Abell clusters of galaxies in the radio luminosity vs absolute optical magnitude plane. The division may not be as clear as it originally seemed, however, as Best (2009) repeated the radio-optical plot from Owen & Ledlow (1994) but with data from the Sloan Digital Sky Survey (SDSS), and found the division between the two populations was not reproduced. There is, however, still a tendency for the two populations to be on their respective sides of the dividing line as shown in Figure 1.3.

1.2. OBSERVATIONS OF RADIO SOURCES

1.2.2 Observations

Observations play a key role in analysing numerical simulations, since a major aim is to accurately predict radio source properties based on observations, and also construct simulations that match known observations. The act of comparing observations and simulations is discussed in Section 1.3, but this section will present a brief overview of some recent observations.

Extragalactic radio jets and their host galaxies are observed through radio and X-ray emission from the core, jet and radio lobes. The X-ray emission is thought to be a combination of both synchrotron emission from relativistic particles accelerated by the jet and inverse-Compton emission from the scattering of photons by relativistic electrons.

Hardcastle et al. (2002) used deep *Chandra* observations of the FR I radio galaxy 3C 31 to measure density, temperature and pressure distributions within a few kpc of the host galaxy. They concluded that the X-ray emission from the core was likely to be the result of inverse-Compton scattering. Croston et al. (2005) looked at X-ray emission from the lobes of 33 classical double radio galaxies and quasars, using *Chandra* and *XMM-Newton*, and concluded among other things that the lobes of these sources do not contain an energetically dominant proton population, and that the X-ray emissions are likely a result of inverse-Compton scattering. Hardcastle et al. (2015) combined deep *Chandra* observations of the radio galaxy Pictor A with Australia Telescope Compact Array (ATCA) observations. The X-ray data spans a 15-year time period, and the spatial, temporal and spectral properties of the radio source are studied in detail. From this analysis, the X-ray emission from the jet is proposed to be synchrotron emission from the boundary layer, rather than inverse-Compton models. Taken together, these three studies indicate that the X-ray emission from the core and radio lobes is due to inverse-Compton processes, however X-ray emission from the jet itself is due to synchrotron processes.

1.2. OBSERVATIONS OF RADIO SOURCES

1.2.3 Comparing Observations and Simulations

Many comparisons of radio source observations with numerical simulations have been carried out. The key features of extragalactic radio jets are reproduced with numerical simulations, such as the bow shock, cocoon and radio lobes in both Krause (2003) and Donohoe & Smith (2016).

Parameter studies of the jet-intracluster medium interaction in the FR I source Hydra A were carried out in Nawaz et al. (2016, 2014), where the jet parameters were determined along with the precession angle and period of the jet such that numerical simulations reproduced i) curvature of the jet, ii) the bright knots along the jet tail, and iii) the jet to plume transition. Other comparisons include the numerical simulation of an X-ray cavity in the archetypal FR II source Cygnus A (Chon et al., 2012) and the numerical simulation of the FR I radio source 3C 31 (Perucho & Marti, 2007).

1.2.4 Double-Double Radio Galaxies

If jets are responsible for providing feedback to their host galaxy, this feedback is expected to eventually truncate black hole accretion and therefore jet production. We would therefore expect to observe some evidence of restarting jet activity. Schoenmakers et al. (2000a) define a double-double radio galaxy (DDRG) as a radio galaxy that “consists of a pair of double radio sources with a common centre. Furthermore, the two lobes of the inner radio source must have a clearly extended, edge-brightened radio morphology” (Schoenmakers et al., 2000a). Adopting this definition, they present four DDRG candidates of Mpc-size, in addition to finding another three sources from the literature that also are likely to be DDRGs. The radio contour plot for one of these DDRG candidates, B 1834+620, is shown in Figure 1.4. The most likely cause for the observed morphology is a restarting jet, though the authors also consider and subsequently reject the following two causes: a change in jet outflow direction; and backflow instabilities. A change in jet outflow direction is unlikely due to the alignment of the inner and outer structures, while

1.2. OBSERVATIONS OF RADIO SOURCES

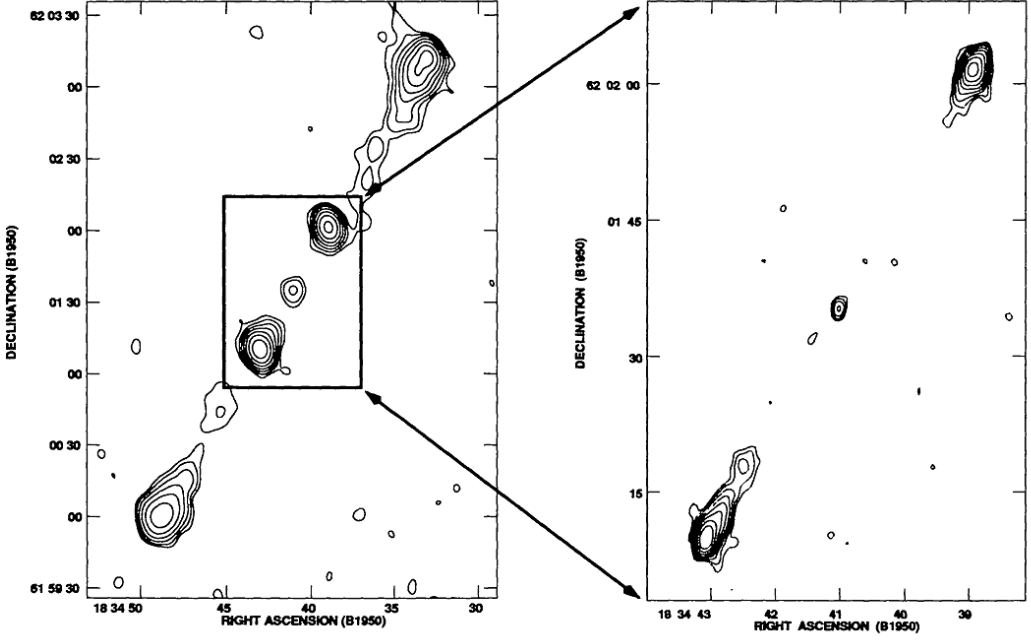


Figure 1.4: Radio contour plot of the DDRG B 1834+620. *Left:* 8.4 GHz VLA observations. *Right:* 1.4 GHz observations of the inner structure. The size of the outer structure is 1660 kpc, and the size of the inner structure is 420 kpc. Credit: Schoenmakers (2001, Figure 1).

backflow instabilities are unlikely due to the symmetry and two-sided nature of the inner DDRG structures.

The timescales of jet interruption can be constrained using the result shown by Kaiser et al. (2000), that the jet hotspots fade on timescales of $10^4 - 10^5$ yr. The model for DDRGs developed by Kaiser et al. (2000) is explained further in Section 1.3.1. In the case of the DDRG B 1834+620 (see Schoenmakers et al., 2000b) one hotspot is still visible in the outer structure, so the timescale of the jet interruption can be constrained to the range 1.1 – 6.4 Myr using the hotspot fading timescale. A much larger sample of radio galaxies was studied in Shabala et al. (2008), modelling the radio source active phase with a jet injection profile represented as a top hat function. The jet injection has durations t_{on} and t_{off} for the timescales of the on and off jet phases respectively. For stellar masses ranging

1.3. MODELS OF ASTROPHYSICAL JETS

from $10^{11} M_{\odot}$ and higher, a typical active timescale t_{on} is on the order of 10^6 yr, increasing with stellar mass as $t_{\text{on}} \propto M_*^{1.1}$. The typical quiescent timescale t_{off} is on the order of $10^7 - 10^8$ yr, decreasing with stellar mass (see Shabala et al., 2008, Table 4). The active timescale agrees with the fuel availability timescale given by cold gas accretion, indicating that the jet active phase is determined by the availability of fuel.

In summary, double-double radio galaxies provide strong evidence for the intermittency of radio jet activity. Typical double-double radio galaxies have an active timescale on the order of $t_{\text{on}} \sim 10^6$ yr while the timescale of the quiescent phase is on the order of $t_{\text{off}} \sim 10^7 - 10^8$ yr.

1.3 Models of Astrophysical Jets

Models of astrophysical jets provide the tools to connect observations with the underlying radio source and environment properties. In this section I introduce models for astrophysical jets in Section 1.3.1, followed by models for bubbles in Section 1.3.2. Finally I provide some examples for numerical simulations of radio jets in Section 1.3.3.

1.3.1 Analytic/Semi-analytic Jet Models

The first basic morphology models of FR II radio sources were those of Scheuer (1974) and Blandford & Rees (1974), which both proposed a relativistic outflow from a central region. A study of the structure, dynamics and thermodynamics of the radio source Cygnus A was done in Alexander & Pooley (1995) using multi-frequency radio observations as well as X-ray and optical data. These authors found that the jet is underdense with respect to the surrounding environment. An analytic self-similar model was developed in Kaiser & Alexander (1997) (the KA model), which has radio sources expanding into an environment with a smooth density profile given by a power-law. The jet is initially assumed to be an uncollimated

1.3. MODELS OF ASTROPHYSICAL JETS

outflow which then collimates due to a reconfinement shock. The basic FR II jet morphology of this model is shown in Figure 1.5, along with basic FR I morphology. Key features expected by this model include self-similarity of the radio source if it is expanding into a spherically symmetric environment that has a density profile less steep than $1/d^2$ (where d is the radial distance from the AGN), as well as the transition to turbulent flow for lower power jets, which would lead to FR I type morphologies. The model is extended in Kaiser et al. (1997) (the KDA model) to include energy losses from synchrotron processes due to relativistic electrons in the jet cocoon, allowing the calculation of radio emission from the radio source.

The assumption that the radio jets are self-similar does not hold for small ($< \text{kpc}$) scales, and the KA model (Kaiser & Alexander, 1997) is extended in Alexander (2006) to the jet evolution on sub-kpc scales. This extended model relies on the lengthscale L_1 , given in Equation (1.7). For distances from the core less than L_1 the jet is overdense with respect to the environment, while for distances greater than L_1 , the jet is underdense. Recollimation of the jet occurs somewhere past this lengthscale, on the order of $16L_1$.

$$\frac{L_1}{\text{pc}} = 25 \left(\frac{Q}{10^{39} \text{W}} \right)^{1/2} \left(\frac{n_x}{3 \times 10^{-5} \text{m}^{-3}} \right)^{-1/2} \left(\frac{v_j}{c} \right)^{-3/2} \quad (1.7)$$

An extension of the KDA analytic model to large radio sources is presented in Alexander (2002). A powerful FR II jet expanding into a cluster environment is considered, and the state of the intracluster medium (ICM) is studied with respect to temporal and thermal evolution. In this model the gas swept up by the jet accumulates at the edges of the cocoon and eventually mixes with the cocoon material because the contact surface develops Rayleigh-Taylor instabilities.

A semi-analytic model that combines both the model for FR II radio sources described in Kaiser & Alexander (1997) and the model for FR I radio sources described in Luo & Sadler (2010) is given in Turner & Shabala (2015). Advantages of this model over previous ones are the inclusions of both subsonic and supersonic cocoon expansion, the inclusion of Rayleigh-Taylor mixing of the cocoon with the

1.3. MODELS OF ASTROPHYSICAL JETS

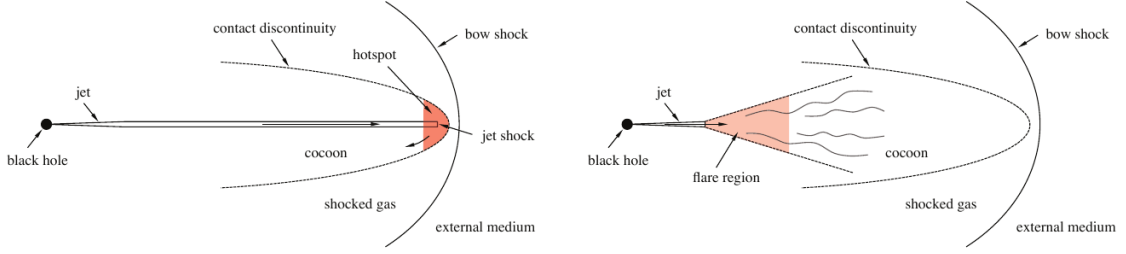


Figure 1.5: Basic radio source morphology. *Left:* FR II morphology. *Right:* FR I morphology. Credit: Turner & Shabala (2015, Figure 1)

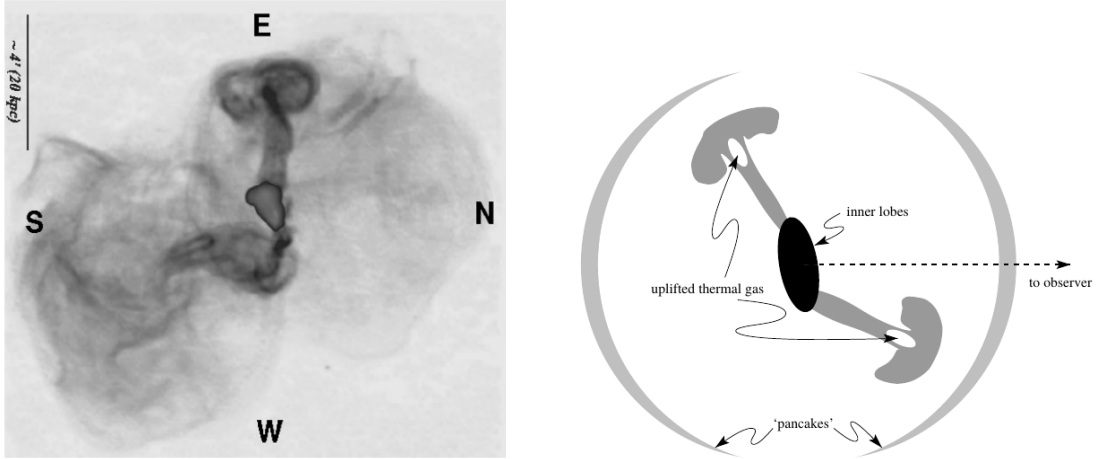
surrounding environment, and the use of arbitrary pressure profiles, including those based on semi-analytic galaxy formation models. This model expands the cocoon into an environment partitioned into small radial regions where the density and temperature are both approximated by simple power laws.

So far, the models mentioned have been for non-restarting jets; however models for the formation of DDRGs also exist. In Kaiser et al. (2000) an analytic model for restarting jet activity causing the formation of DDRGs is presented. In this model the interruption of the jet flow causes material from the environment to begin filling in the jet channel, passing through the cocoon boundary. The restarted jet then punches through this material and gives rise to the inner source structure. The inflow of material is required for the morphology of the restarted jet since the low density in the cocoon given by standard FR II models prevents the formation of the inner source structure, which is inconsistent with observations. The resulting model of a restarting jet production mechanism is consistent with the observations from Schoenmakers et al. (2000a).

1.3.2 Analytic/Semi-Analytic Bubble Models

The radio lobes inflated by low power jets become rising bubbles of gas that detach from the core when they are large enough, or after the jets switch off. A well-studied example of these bubbles is in the Perseus cluster, specifically the galaxy NGC 1275. These rising bubbles disturb the cooling flow within the inner 18 kpc

1.3. MODELS OF ASTROPHYSICAL JETS



(a) Radio halo of M87 at 327 MHz rotated 90° clockwise. Credit: Churazov et al. (2001, Figure 1, upper-left)

(b) Possible geometry of the source. Credit: Churazov et al. (2001, Figure 1, lower)

Figure 1.6: M87 bubbles.

(Boehringer et al., 1993). Observations of the Perseus cluster revealed what is thought to be sound waves propagating through the intracluster medium (Fabian et al., 2003). (Fabian et al., 2003) predict that the bubble's energy is continuously dissipated through these sound waves, which are caused by the bubbles.

Churazov et al. (2001) developed a model for these bubbles of hot gas with reference to the galaxy M87, which has bubbles as shown by the radio observations and possible source geometry in Figure 1.6. These bubbles rise through the gas at around half the speed of sound, and uplift the central gas to large distances, thereby doing work on the environment. The authors find that buoyant bubbles of cosmic rays are successful in reproducing the observed features of M87, see Figure 1.6. These bubbles affect the energetics of the host galaxy and may play a role in the heating/cooling balance of AGN feedback.

1.3.3 Numerical Simulations

The first self-consistent two-dimensional numerical simulation of a one-sided restarting jet was performed in Clarke & Burns (1991), using the ZEUS-2D computational code with the magneto-hydrodynamic (MHD) solver. These simulations in Clarke & Burns (1991) were carried out in a uniform ambient medium using a pressure-matched jet with an internal Mach number of $M = 6.0$ and a density ratio of $\eta = 0.1$. The toroidal and poloidal components of the magnetic field are also computed, in order to calculate synchrotron emissivity maps.

A series of in-depth numerical simulations using the PLUTO code have been carried out by Hardcastle & Krause (2013, 2014) and English et al. (2016), with the focus on simulating realistic radio lobes. The unique aspect of these simulations is the cluster environment they are carried out in, which is modelled using the standard isothermal β model as shown in Equation (1.8), rather than a simple constant density environment. Hardcastle & Krause (2013) looks at 2D hydrodynamical simulations and conclude that lobe growth is not self-similar and in fact the jet lobes come into pressure balance with the external pressure at the lobe mid-point during the simulations. The simulations can approximately reproduce 3C radio source radio luminosities, and show that FR II radio jets are ineffective at suppressing cooling due to their inability to couple effectively to the hot centre of the host galaxy, however the heating of localized pockets in other parts of the cluster is observed. The most interesting result with respect to AGN feedback is that they find that the ratio of energy stored in the lobes to energy stored in the shocked region is close to unity for all times.

$$n = n_0 \left[1 + \left(\frac{r}{r_c} \right)^2 \right]^{-3\beta/2} \quad (1.8)$$

Hardcastle & Krause (2014) extends the previous work to fully 3D magneto-hydrodynamic simulations. Most importantly, these simulations reproduce the result of Hardcastle & Krause (2013), i.e. that the ratio of energy in lobes to shocked region is approximately unity, albeit with a larger scatter than the earlier

1.3. MODELS OF ASTROPHYSICAL JETS

paper.

Numerical simulations of both radio jet and the subsequent bubbles that are formed was carried out by Alouani Bibi et al. (2007). They looked at both a one-cycle and two-cycle jet, and found that the two-cycle jet is more effective at heating gas within 10 kpc of the cluster centre, due to the increased environmental coupling efficiency. The energy in the bubbles was found to be about 6 times less than the energy input of the jet.

Vernaleo & Reynolds (2007) also looked at the energetics of jet inflated cocoons and found that cocoon-bounded sources (that is, radio sources that inflated bubbles that rose buoyantly once jet activity ceased) had a greater impact on the entropy of the environment due to shocks, however the energy efficiency showed no clear distinction between cocoon or non-cocoon bounded sources (Vernaleo & Reynolds, 2007, Figure 13). Perucho et al. (2014) performed long-term axisymmetric numerical solutions of relativistic jets, and found that heating of the environment is mainly through shocks. Additionally their results support dual-mode AGN kinetic feedback (Shabala et al., 2011) where low-power jets (identified with FR I) perform feedback mainly on the inner region of the host galaxy, within ~ 100 kpc, while high power jets (identified with FR II) additionally heat larger regions on the order of hundreds of kiloparsecs.

The coupling of jet energy to the environment was explored for different jet densities in Donohoe & Smith (2016), where it was found that the fraction of energy transferred to the environment from the jet increased as the jet/environment density decreased, to a maximum of $\approx 80\%$ for jets with a density ratio of $\eta = 0.0001$. This energy is largely in the form of thermal energy, with the remainder being almost completely kinetic energy. These simulations were carried out in a homogeneous environment which means that the effect of gravitational potential energy was not considered. For simulations in a more realistic environment with a β -model density profile, Vernaleo & Reynolds (2007) found that a large fraction (50% – 80%) of the injected jet energy had the form of gravitational potential energy due to the expanding jet cocoon lifting up material from the core. The majority of the simu-

1.4. SIMULATIONS OF ASTROPHYSICAL FLUID FLOWS

lations with 50% of the injected jet energy in the form of gravitational potential energy were cocoon-bounded sources, however there is no clear distinction in energy distribution between cocoon- and non-cocoon-bounded sources, see Vernaleo & Reynolds (2007, Figures 12,13,14). The cocoon-bounded sources are likely to be more realistic, as these are more consistent with radio and X-ray observations of galaxy clusters.

1.4 Simulations of Astrophysical Fluid Flows

Astrophysical jets can be modelled as supersonic plasma outflows using the hydrodynamic (HD) equations on a computational grid. The full derivation of the hydrodynamics equations is shown in e.g. Teyssier (2015, Section 2). The hydrodynamics equations in the Eulerian form are:

$$\frac{\partial \rho}{\partial t} + \nabla \cdot (\rho \mathbf{u}) = 0 \quad (1.9)$$

$$\frac{\partial \rho \mathbf{u}}{\partial t} + \nabla \cdot (\rho \mathbf{u} \mathbf{u}) = -\rho \nabla \Phi - \nabla P \quad (1.10)$$

$$\frac{\partial e_i}{\partial t} + \nabla \cdot (e_i \mathbf{u}) = -P \nabla \cdot \mathbf{u} \quad (1.11)$$

where ρ is the fluid density, \mathbf{u} is the fluid velocity vector, Φ is the gravitational potential, P is the pressure and e_i is the internal energy density.

Equation (1.9) is the conservation of mass, Equation (1.10) is the conservation of momentum and Equation (1.11) is the conservation of energy. The Euler equations are conservative in this form which makes them an excellent fit for grid-based numerical schemes due to the ease with which the computational domain can be split into sub-domains. Ghost zones are used to extend the computational domain beyond the boundaries of the simulation in order to correctly handle boundary conditions such as mass inflow. These equations do not handle magnetic fields

1.5. A BRIEF HISTORY OF ASTROPHYSICAL HYDRODYNAMICS

or relativistic flows, however they can be extended to do so as shown in Teyssier (2015). These extensions are beyond the scope of this thesis, and I therefore do not discuss them further.

1.5 A Brief History of Astrophysical Hydrodynamics

The first publicly available software designed to simulate astrophysical flows was ZEUS-2D, which was developed by Stone & Norman (1992a). ZEUS-2D contains modules for solving the equations of hydrodynamics (Stone & Norman, 1992a), magnetohydrodynamics (Stone & Norman, 1992b) and radiation hydrodynamics (Stone et al., 1992). ZEUS-2D solves these equations on a 2-dimensional grid in an orthogonal coordinate system.

The NIRVANA simulation code is more recent and builds on the ZEUS-2D code. NIRVANA solves the magnetohydrodynamics equations on a 2-dimensional Cartesian grid as described in Ziegler (1998). A large advance in NIRVANA compared to previous simulation codes is the inclusion of adaptive mesh refinement, or AMR. Adaptive mesh refinement recursively increases the resolution of grid patches selected by a certain criteria, with the goal of accurately capturing physics in certain areas of the computational domain, such as near the injection boundary, while avoiding unnecessarily high resolution in the other areas (Ziegler, 1998).

One of the first numerical codes for computational astrophysics to solve the full 3-dimensional hydrodynamics equations was FLASH, which is described in Fryxell et al. (2000). Similar to NIRVANA, FLASH also makes use of adaptive mesh refinement for the computational grid. FLASH was the one of the first simulation codes to support both AMR and parallelism. By using the Message-Passing Interface (MPI) library, FLASH can be easily scaled to run on massively parallel machines.

Two modern numerical codes for computational astrophysics are ENZO (Bryan et al., 2014) and PLUTO (Mignone et al., 2007). Both codes solve both hydro-

1.6. RELIABILITY OF NUMERICAL SIMULATIONS OF AGN JETS

dynamics and magnetohydrodynamics equations on 1-dimensional, 2-dimensional and 3-dimensional grids, with the ability to use adaptive mesh refinement, while supporting parallel execution. ENZO only supports the Cartesian coordinate system, while PLUTO simulations can be carried out in Cartesian, Cylindrical, Polar and Spherical coordinate systems. Support for curvilinear coordinate systems in PLUTO required the extension of existing high-order reconstruction schemes to curvilinear coordinates as described in Mignone (2014). The support of different coordinate systems makes PLUTO a good choice for simulating astrophysical jets due to the inherently curvilinear nature of the jets. As I discuss in more detail in Chapter 2, approximating the opening angle of an astrophysical jet in a Cartesian coordinate system requires higher resolution grid patches around the jet inlet.

1.6 Reliability of Numerical Simulations of AGN Jets

The reliability of astrophysical simulations with respect to the simulation resolution was investigated by Krause & Camenzind (2001). The MHD simulation code NIRVANA was used by these authors to simulate an axisymmetric two-dimensional jet. These simulations were unique at the time due to the high resolution used for the simulation compared to previous studies. The authors found that the global parameters of the jet (specifically the internal energy, axial momentum, mass, and average velocity) all converged at ~ 100 points per beam radius (ppb), shown in Figure 1.7.

Despite the difficulties in obtaining conditions closely resembling astrophysical ones in the laboratory, numerical simulations have also been compared to experimental results. In Tordella et al. (2011), jets were produced in the laboratory with similar Mach number and jet density ratios to astrophysical jets. The jet flows were produced with a de Laval nozzle, and propagated in a cylindrical vacuum vessel, using a setup developed in Belan et al. (2004, 2008, 2010). A nozzle corresponding to a Mach number of 15 was studied in Tordella et al. (2011). The experimental

1.6. RELIABILITY OF NUMERICAL SIMULATIONS OF AGN JETS

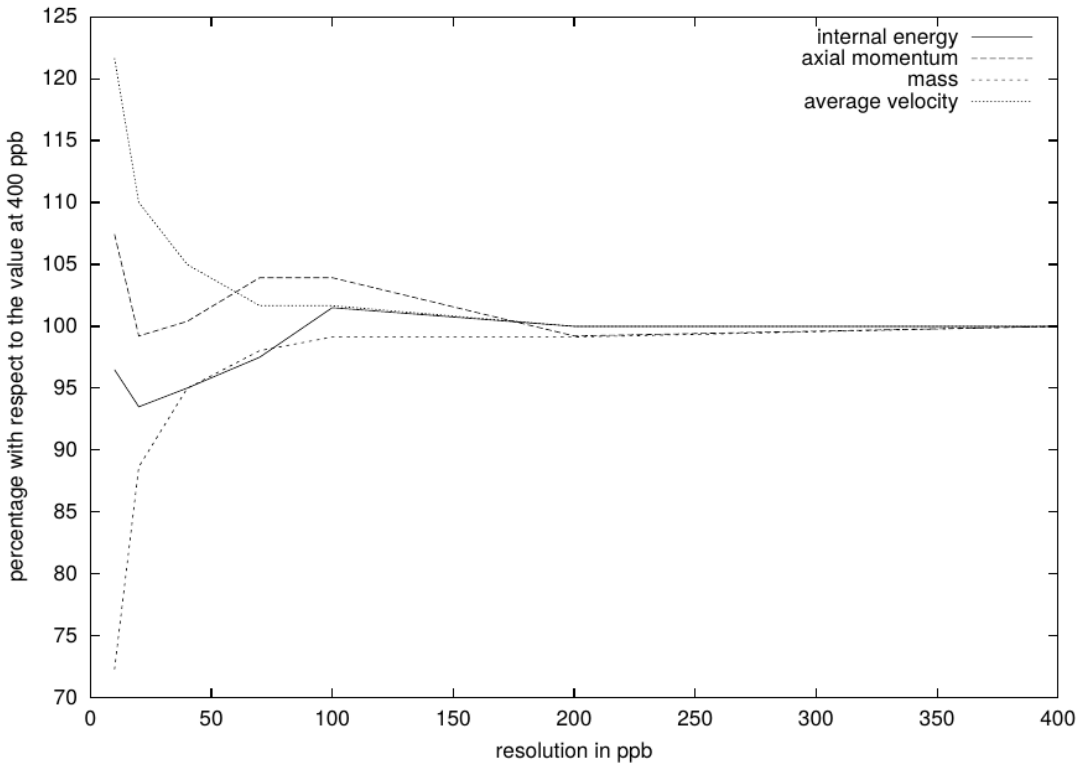


Figure 1.7: Convergence of four global jet parameters.(Krause & Camenzind, 2001, Figure 13)

results were compared with numerical simulations computed with PLUTO using a 3D hydrodynamical solver on a Cartesian grid with resolution 860 x 172 x 172. Internal boundaries were placed on the grid at $r = \sqrt{y^2 + z^2}$ to reproduce the cylindrical experiment vessel. The authors conclude that the numerical simulations agree with the experimental results, within experimental errors. A comparison between experimental results and numerical simulations is shown in Figure 1.8.

This study was extended in Belan et al. (2013) to look at a wider range of Mach numbers (10, 15, 20), while building on the experimental setup of Tordella et al. (2011). The experimental results were compared with numerical simulations computed using PLUTO as in Tordella et al. (2011), however 2D cylindrical coordinates were used. The author's findings support those from Tordella et al. (2011) with respect to the agreement between experimental results and numerical simulations.

1.7. SUMMARY

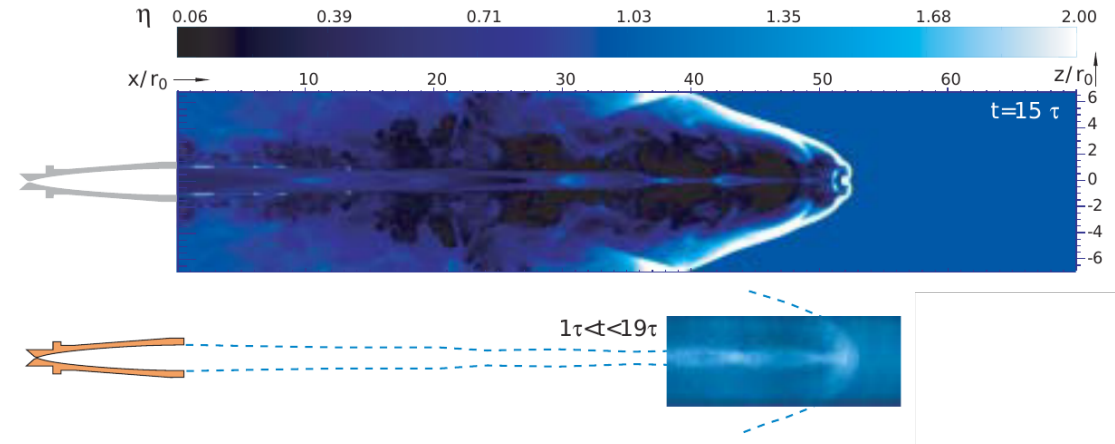


Figure 1.8: Comparison between experimental results and numerical simulations. *Top:* simulation of a light jet. *Bottom:* laboratory visualization of the corresponding helium jet in xenon. Credit: Tordella et al. (2011, Figure 4)

The authors note that both the experimental and numerical results agree in most cases and reproduce the basic dynamics of astrophysical jets, despite not accounting for processes such as radiative cooling and magnetic fields. This implies that fluid dynamics is likely the major determinant of jet characteristics, and supports investigating jet dynamics with PLUTO.

1.7 Summary

In this chapter I introduced the basic concepts behind galaxy formation and black hole accretion, then as described the importance of AGN feedback on maintaining the heating/cooling balance. Intermittent jet activity is likely to occur due to the effect of AGN feedback on the host galaxy, and there is observational evidence for this in the form of double-double radio galaxies. In the remainder of this thesis I will present numerical simulations of intermittent jets in realistic environments, with a focus on the energetics and morphology of the jets. I will provide insight into how the injected jet energy affects the overall energetics of the environment, and whether this changes with the number of jet outbursts.

CHAPTER 2

Numerical Simulations with PLUTO

I carried out 2-dimensional hydrodynamic simulations of Fanaroff-Riley type II (FR II) radio jets in different environments using the PLUTO numerical code for computational astrophysics, version 4.2 (Mignone et al., 2007). The *hllc* solver was used with linear reconstruction using a *minmod* limiter. The simulations were carried out on the Tasmanian Partnership for Advanced Computing (TPAC) computing facility provided by the University of Tasmania, with the longest simulations taking roughly 48 hours to complete, using 64 cores. In this chapter I begin with detailing how the simulations are non-dimensionalised through the use of characteristic length scales in Section 2.1 and how the computational domain is divided up into a simulation grid in Section 2.2. Next I explain the jet injection method in Section 2.3, how the addition of magnetic fields may affect the results in Section 2.4, and how the restarting nature of the jet is implemented in Section 2.5. The realistic gas density profiles into which the jets expand is an important feature of these simulations. I describe these gas density profiles in Section 2.6, and list the jet parameters and simulation timescales in Section 2.7 and Section 2.8. The simulation suite is described in Section 2.9, and Table 2.3 shows the different run parameters.

2.1. LENGTH SCALES

2.1 Length Scales

The simulations are carried out using dimensionless units, which requires choosing a unit length, unit time and unit density in order to scale the physical units. The radio source dynamical model of Kaiser & Alexander (1997) for self-similar radio sources is extended in Alexander (2006) to non-self-similar evolution. In doing so a characteristic length scale L_1 is identified, which is given by

$$L_1 = 2\sqrt{2} \left(\frac{Q}{\rho_x v_{\text{jet}}^3} \right)^{1/2} \quad (2.1)$$

where ρ_x is the ambient density, Q is the kinetic jet power and v_{jet} is the jet velocity. This length scale corresponds to the region where the jet is overdense with respect to the environment. Because L_1 is small, on the order of a few kpc, it is a good approximation to assume a constant density environment where $\rho_x = \rho_0$.

Similarly an outer length scale L_2 for a constant density environment is given by Komissarov & Falle (1998) as

$$L_2 = \left(\frac{Q}{\rho_x c_x^3} \right)^{1/2} \quad (2.2)$$

where c_x is the external sound speed, i.e. the sound speed in the ambient gas (typically $500 - 1000 \text{ km s}^{-1}$ in the hot intracluster medium of galaxy clusters). This length scale is associated with the jet expansion velocity becoming comparable to the sound speed.

There are three more length scales that are related to L_1 . These correspond to morphological changes in the jet, as detailed in Krause et al. (2013). L_{1a} corresponds to the recollimation of the jet and occurs when the sideways ram pressure of the jet is equal to the ambient pressure of the gas. This length scale is given by

2.2. SIMULATION GRID

$$\left(\frac{L_{1a}}{L_1}\right)^2 = \frac{\gamma}{4\Omega} M_x^2 \sin^2 \theta \quad (2.3)$$

where γ is the ratio of specific heats, $\Omega = 2\pi(1 - \cos \theta)$ is the solid angle of the conical jet with half-opening angle θ , and M_x is the external Mach number.

L_{1b} corresponds to the beginning of cocoon formation for the jet which occurs when the jet density ρ_j is less than or equal to the environment density ρ_x . This length scale is given by

$$\left(\frac{L_{1b}}{L_1}\right)^2 = \frac{1}{\Omega} \quad (2.4)$$

L_{1c} corresponds to the termination shock point for an uncollimated jet which occurs when the total ram pressure of the jet falls below the environment pressure. This length scale is given by

$$\left(\frac{L_{1c}}{L_1}\right)^2 = \frac{\gamma}{4\Omega} M_x^2 \quad (2.5)$$

L_1 is used as the unit length for the simulations, c_x is used as the unit velocity, and the environment density at $r = L_{1b}$ (where the jet density and environment density are roughly equal) is used as the unit density. From these, other unit quantities, including time and power, can be calculated .

2.2 Simulation Grid

The simulations are carried out on a 2-dimensional spherical polar grid. 2-dimensional simulations are computationally cheaper than 3-dimensional simulations since computation time linearly increases with the number of grid cells in the simulation, e.g. for a square vs. cubic grid with side length 100, the computational time required would be $t \propto 100^2$ and 100^3 for the 2-dimensional and 3-dimensional case respectively. 3-dimensional simulations would not be likely to affect the jet properties being investigated in this thesis. In related work, Hardcastle & Krause (2013)

2.2. SIMULATION GRID

compared 3-dimensional simulations with corresponding 2-dimensional simulations and found that the resultant lobe dynamics are very similar in these two cases.

The simulations carried out in this thesis use a 2-dimensional grid in spherical coordinates, (r, θ) , with the jet launched in the r direction along the plane $\theta = 0$. A resolution study was carried out (see Section 3.1.5) and a radial resolution of 5 grid cells per 1 kpc was chosen, giving 2000 cells for a simulation grid extending out to $r = 400$ kpc. The number of cells in the θ coordinate is 448. The grid is inhomogeneous and consists of six grid patches each containing a number of equally spaced grid cells in r, θ . Splitting the grid up into several grid patches allows the simulation to properly capture the physics of the jet while reducing the computational power required by having coarser resolution in areas of the simulation domain where changes to the hydrodynamical quantities (ρ, P, \mathbf{v} etc.) are slow. The grid patches and how they make up the total simulation grid are shown in Figure 2.1.

There are 2 grid patches in the radial coordinate. The first is from $r = 1.0$ to $r = 2.0$ (simulation units) which consists of 64 grid cells, while the second grid patch is from $r = 2.0$ to the end of the simulation domain, with 2000 grid cells. The purpose of the first patch is to provide high resolution at the jet inlet which ensures the jet can propagate onto the grid, as well as ensure that the ghost cells PLUTO uses as the boundary conditions do not contain $r = 0$. The use of ghost cells around the simulation grid is described in Section 2.2.1. Earlier runs without the additional high resolution patch ran into numerical errors due to the ghost cells containing the origin of the simulation domain.

There are 3 grid patches in the θ coordinate. The first is from $\theta = 0$ to $\theta = 5$ degrees which consists of 64 grid cells, the second is from $\theta > 5$ to $\theta = 17$ degrees which consists of 128 grid cells, and the third is from $\theta > 17$ to $\theta = 90$ degrees with 256 grid cells. Because the simulation is using a spherical polar grid, azimuthal fidelity is lost as the radial coordinate increases. The extra grid patches with increased resolution in the θ coordinate are implemented with the aim of increasing azimuthal fidelity as the radial coordinate increases, while minimising

2.2. SIMULATION GRID

the increase in computational power required.

The half-opening angle used for all simulations in this thesis is $\theta_{\text{half opening}} = 15^\circ$. The first and second grid patches in θ were chosen to cover $0 \leq \theta \leq 17^\circ$ with higher resolution than $\theta > 17^\circ$, which contains the entirety of the opening angle used. Additionally the aspect ratios of the resulting structures are narrow since the radio jets are longer than they are wide, meaning that most of the dynamics occurs within the first and second grid patches. The structure at the head of the jet needs to be well resolved for the jet to propagate realistically, requiring ≥ 5 cells across the jet head at the hotspots. The first grid patch in θ of $0 \leq \theta \leq 5^\circ$ provides approximately 15 cells across a 2 kpc jet head at a distance of 100 kpc from the core. Because the jet is propagating almost directly along the $\theta = 0$ plane, there is little point in having high resolution for the third grid patch at large θ , where the simulation quantities are changing slowly.

2.2.1 Boundary Conditions

I use reflective boundary conditions on the upper and lower radial boundaries, an axisymmetric boundary on the $\theta = 0$ axis and an equatorially symmetric boundary on the $\theta = \pi/2$ axis. Initial simulations used an outflow boundary condition on the upper radial boundary, however it was found that this caused a mass influx onto the simulation grid so a reflective boundary is used instead to ensure that mass is conserved. The boundary condition equations are given below, where q represents a scalar quantity, \mathbf{v} represents a vector field and \mathbf{B} is the magnetic field. The magnetic field is included in the boundary condition equations for illustrative purposes, however no simulations contained magnetic fields.

In the reflective boundary condition, Equation (2.6), variables are symmetrized across the boundary, while the sign of the normal component to the interface of vector fields is reversed. The axisymmetric boundary condition, Equation (2.7), is identical to the reflective boundary condition except for the fact that the tangential component of the vector field also changes sign. Here the axis subscript is

2.3. JET INJECTION METHOD

$(r, \theta = 0)$ in spherical coordinates. The equatorially symmetric boundary condition, Equation (2.8), is identical to the reflective boundary condition except for the fact that the sign of the magnetic field is reversed.

$$\text{Reflective: } q \rightarrow q, \begin{cases} v_n \rightarrow -v_n \\ B_n \rightarrow -B_n \end{cases}, \begin{cases} v_t \rightarrow v_t \\ B_t \rightarrow B_t \end{cases} \quad (2.6)$$

$$\text{Axisymmetric: } q \rightarrow q, \begin{cases} v_n \rightarrow -v_n \\ B_n \rightarrow -B_n \end{cases}, \begin{cases} v_\phi \rightarrow -v_\phi \\ B_\phi \rightarrow -B_\phi \end{cases}, \begin{cases} v_{\text{axis}} \rightarrow v_{\text{axis}} \\ B_{\text{axis}} \rightarrow B_{\text{axis}} \end{cases} \quad (2.7)$$

$$\text{Equatorial: } q \rightarrow q, \begin{cases} v_n \rightarrow -v_n \\ B_n \rightarrow B_n \end{cases}, \begin{cases} v_t \rightarrow v_t \\ B_t \rightarrow -B_t \end{cases} \quad (2.8)$$

Setting an equatorially symmetric boundary condition on the $\theta = \pi/2$ boundary has the advantage of approximating the presence of an opposing counter-jet. The introduction of azimuthal boundary conditions into the simulation domain is a limitation of simulating only a quarter-plane; an advantage of simulating the entire plane (including a counter-jet) would be the removal of azimuthal boundary conditions. This is the approach taken by Hardcastle & Krause (2013), who additionally break the jet-counterjet symmetry at the $\theta = \pi/2$ boundary by introducing small-scale asynchronous periodic perturbations in the jet and counterjet Mach numbers. This nice approach is beyond the scope of this thesis.

PLUTO makes use of ghost zones that extend the user-defined grid boundaries. These ghost zones are needed to complete the reconstruction stencil at the boundaries. In addition, boundary conditions are actually defined in these ghost zones, and are then propagated onto the grid. An example of these ghost zones is shown in

2.3 Jet Injection Method

The jet is injected on the lower r boundary as a conical mass inflow boundary condition where $0 \leq \theta \leq \theta_{\text{jet}}$. The half-opening angle θ_{jet} is chosen to be 15° .

2.4. ABSENCE OF MAGNETIC FIELDS

This will ensure that the simulation produces FR II morphologies on large scales as detailed in Krause et al. (2013). Cells on the injection boundary at $r = 1$ in simulation units have a density $\rho = \rho_{\text{jet}}$ and a radial velocity $v_r = M_x c_x$ for $\theta \leq \theta_{\text{jet}}$ while cells with $\theta \geq \theta_{\text{jet}}$ have a reflective boundary condition imposed. Tracer particles are used to trace jet material throughout the simulation. The jet material is injected with a tracer value of 1.0 while the environment has a tracer value of 0.0. The jet is injected in pressure equilibrium with the environment, $p = p_x$.

Because the jet is injected at a radius of $r = 1$ in simulation units, the physical injection distance (in kpc) from the core is simply L_1 for the simulation. The realistic environments simulated in this thesis have L_1 ranging from 0.36 kpc to 1.6 kpc, and are discussed in Section 2.6. Injecting the jet at these distances from the core is sufficient for exploring the interaction of the jet with the homogeneous intracluster medium. This is in contrast to investigating jet interaction with the multi-phase interstellar medium, which requires injecting the jet at least an order of magnitude closer to the core in addition to parsec-scale grid resolution, as studied by e.g. Sutherland & Bicknell (2007) and Wagner & Bicknell (2011). The minimal effect of injection radius is supported by two simulations which injected the jet closer to the core as detailed in Section 3.1.5. No significant difference in the resultant morphology was found between the two different injection radii.

2.4 Absence of Magnetic Fields

It should be noted that the simulations presented here are purely hydrodynamical, i.e. no magnetic fields are included. This allows the computational complexity of the problem to be greatly reduced, while still capturing the major dynamical processes that occur in radio jets. Hardcastle & Krause (2013) note that the addition of magnetic fields would in principle suppress Kelvin-Helmholtz instabilities. The effect of magnetic fields on numerical simulations was investigated in detail by Hardcastle & Krause (2014) with reference to the authors' earlier paper without magnetic fields, Hardcastle & Krause (2013). These authors find that including the

2.5. RESTARTING THE JET

magnetic field in numerical simulations does not change the major dynamics of the resulting jet, reproducing the broad dynamical conclusions found in Hardcastle & Krause (2013). Because this thesis is concerned with the dynamics of jet-inflated structures (i.e. radio lobes), a purely hydrodynamical approach is sufficient.

2.5 Restarting the jet

A major focus of the simulations presented in this thesis is the effects of intermittent jet activity on energetics in the simulation and the resulting jet morphology. Each simulation is evolved for the same total time of 200 Myr, see Section 2.8. The total active time of the jet also remains constant at 40 Myr which corresponds to a 20% duty cycle over the total simulation time. The actual times for the jet switching “on” and “off” are determined by the total number of outbursts, ranging from 1 to 4. Each outburst is equally spaced in time, and has a tracer particle associated with it. When the jet is switched off, the entire lower radial plane becomes a reflective boundary.

Initial experiments into restarting the jet simply switched the jet on or off abruptly at appropriate times; however I found that PLUTO could not handle the sudden transition from smooth gradients in density and pressure to large discontinuities and the simulation would crash. To solve this problem I implemented a “ramp” phase for turning the jet both on and off. This is implemented using a sinusoidal ramp in the jet inlet velocity as a function of the difference between the current time and the relevant on or off times as shown in Figure 2.3:

$$v_{\text{jet}}(t) = v'_{\text{jet}} \times \left[1 - \cos \left(\frac{\pi}{2} \times \frac{t - (t_{\text{on time}} - \Delta t)}{\Delta t} \right) \right] \quad \text{Ramp up (jet on)} \quad (2.9)$$

$$v_{\text{jet}}(t) = v'_{\text{jet}} \times \cos \left(\frac{\pi}{2} \times \frac{t - t_{\text{off time}}}{\Delta t} \right) \quad \text{Ramp down (jet off)} \quad (2.10)$$

where Δt is the timescale of the “ramp” phase, v_{jet} and v'_{jet} are the ramped and target jet velocities respectively, t is the current simulation time, and $t_{\text{on time}}$ and

2.6. REALISTIC GAS DENSITY PROFILES

$t_{\text{off time}}$ are the switch on and off times for the jet.

The timescale of this “ramp” phase is chosen to be $\Delta t = 0.01$ simulation units, which corresponds to a physical time of $\Delta t = 4.01 \times 10^{-3}$ Myr for a cluster environment with $M_{\text{halo}} = 10^{14.5} M_{\odot}$, and $\Delta t = 8.35 \times 10^{-2}$ Myr for a poor-group environment with $M_{\text{halo}} = 10^{12.5} M_{\odot}$, much shorter than the characteristic timescale of 1 simulation unit. I investigate the effect this “ramp” phase has in Section 3.1.5 to determine whether the timescale affected the resulting simulation. I find that the choice for timescale has no significant effects on the simulation, even for the lower mass halo environments where the actual physical timescale is longer.

2.6 Realistic Gas Density Profiles

Now that I have described the implementation of the jet, I will detail the environment into which it propagates. An important aspect of these simulations is that the jet is propagating into an environment given by a declining gas density profile set by a semi-analytic galaxy formation model, rather than one of constant density or an arbitrarily chosen profile. The simulations are carried out at redshift $z = 0$, and the Planck15 cosmology (Aghanim et al., 2016) is used ($H_0 = 67.7 \text{ km s}^{-1} \text{ Mpc}^{-1}$, $\Omega_M = 0.307$). The gas density profile used in the majority of these simulations is derived by assuming the gas is in hydrostatic equilibrium with the gravitational potential of a corresponding dark matter halo. Two different dark matter halo masses are simulated: $M_{\text{halo}} = 10^{14.5} M_{\odot}$, representative of a cluster environment; and $M_{\text{halo}} = 10^{12.5} M_{\odot}$, representative of a poor group environment. The complete derivation of the gas density profile is shown in Appendix A; however an overview is given here.

Navarro et al. (1997) determined a universal density profile for dark matter using N-body simulations, shown in Equation (2.11), where δ_c is given by Equation (2.12),

$$\frac{\rho(r)}{\rho_{\text{crit}}} = \frac{\delta_c}{(r/r_s)(1+r/r_s)^2} \quad (2.11)$$

$$\delta_c = \frac{200}{3} \frac{c^3}{(\ln(1+c) - c/(1+c))} \quad (2.12)$$

2.6.1 Concentration Parameter

In Equation (1.2) c is the dark matter concentration parameter, and is crucial for predicting the dark matter density distribution. Many models for the concentration parameter have been found through N-body simulations. An influential paper by Bullock et al. (2001) provided the first simple model for the concentration parameter as a function of halo mass and redshift. As computational power increased more detailed simulations could be run and better models could be produced. As the Planck15 cosmology is used in this thesis, only models from N-body simulations using the Planck15 cosmology are used in this work. The two recent models for concentration parameter considered were Dutton & Maccio (2014) and Klypin et al. (2016). These two models are shown in Figure 2.4. The Klypin et al. (2016) concentration model for a relaxed (i.e. in equilibrium, not having undergone a recent merger) dark matter halo shown in Equation (2.13) was used to calculate the concentration parameters for the NFW dark matter density profile, where $c_0 = 7.75$, $\gamma = 0.100$, and $M_0/10^{12}h^{-1}\text{M}_\odot = 4.5 \times 10^5$. The simulations are carried out at a redshift of $z = 0$, so there is very little difference between the two profiles, and the choice would not significantly affect the result.

$$c(M) = c_0 \left(\frac{M}{10^{12}h^{-1}\text{M}_\odot} \right)^{-\gamma} \left[1 + \left(\frac{M}{M_0} \right)^{0.4} \right] \quad (2.13)$$

2.6.2 Gas Density Distribution

If the environment is spherical and isothermal, then the density distribution ρ_g satisfies the hydrostatic equilibrium equation,

2.6. REALISTIC GAS DENSITY PROFILES

$$\frac{kT_x}{\mu m_p} \frac{d \ln \rho_g}{dr} = -\frac{GM(r)}{r^2} \quad (2.14)$$

where T_x is the gas temperature, ν and m_p are the mean molecular weight and proton mass, and $M(r)$ is the mass distribution of the system. Neglecting the effect of self-gravity on the gas and assuming the gravitational potential is solely due to the dark matter halo produces the Makino gas density profile $\rho_g(r)$ as shown by Makino et al. (1998),

$$\begin{aligned} \rho_g(r) &= \rho_{g0} \exp \left\{ -\frac{27}{2} b \left[1 - \frac{\ln(1 + r/r_s)}{r/r_s} \right] \right\} \\ &= \rho_{g0} e^{-27b/2} \left(1 + \frac{r}{r_s} \right)^{27b/(2r/r_s)} \end{aligned} \quad (2.15)$$

where b is a scaling parameter given by Equation (1.6). I remind the reader that a justification for why neglecting self-gravity is an acceptable assumption is presented in Section 1.1.3 and

$$b(M) \equiv \frac{8\pi G \mu m_p \delta_c(M) \rho_{c0} r_s^2}{27kT_X} \quad (1.6 \text{ revisited})$$

The simulation does not include cooling, and the gas density profile used assumes that the environment is isothermal. An isothermal environment is a good approximation due to the short timescale of thermal conduction in clusters and groups; however the temperature changes from T_{vir} with radius by factor of approximately 2 – 3 (Vikhlinin et al., 2006), so this is not without some issues. The main issue with the isothermal assumption is that it requires a higher core density in both clusters and poor groups which in turn affects the jet dynamics. In addition, the Makino profile is unrealistically steep at large radii from the centre.

An alternative gas density profile is also considered, the isothermal β -model or King profile, as shown in Equation (2.16). The King profile is purely empirical and was initially derived from observations in King (1962). This profile has lower central densities than the Makino profile, and is less steep at large radii, see Figure 2.5.

2.7. JET PARAMETERS

The effect of the different environment profiles on the resulting jet morphologies is investigated in Section 3.6.

$$n = n_0 \left[1 + \left(\frac{r}{r_c} \right)^2 \right]^{-3\beta/2} \quad (2.16)$$

2.7 Jet Parameters

The computational complexity of the simulations decreases with increasing jet power as $Q^{-1/2}$ due to the use of L_1 as the unit length. A higher jet power results in a longer unit time, meaning the simulation can simulate the same physical time in shorter simulation time. Initially a jet power of 10^{38} W (characteristic of a moderate power FR II) was chosen, however resolution issues were encountered due to L_1 being too large. Because of this a jet power of 10^{37} W was chosen as the representative jet power. This jet power is typical of a medium-to-high powered jet, as shown by Turner & Shabala (2015), and above the FR I/II divide.

The external Mach number of the jet affects the computation time of the simulations as $\sqrt{M_x^3}$, again due to the use of L_1 as the unit length. A higher external Mach number results in a lower unit time, meaning the simulation needs to run for longer in order to simulate the same physical time as a lower M_x simulation. Initially an external Mach number of 35 was chosen, however this required too much computational time to simulate the desired jet parameters and timescales, so an external Mach number of $M_x = 25$ was chosen to be the representative Mach number for the simulations. While this Mach number is lower than physical Mach numbers observed in astrophysical jets (Krause et al., 2013), this choice is supported by the work done by Hardcastle & Krause (2013), who investigated the dependence of jet dynamics on the Mach number in simulations similar to those presented here.

2.8 Simulation Times

The majority of the simulations run for 200 Myr, with a total active jet time of 40 Myr and a total quiescent time of 160 Myr. The simulation outputs the simulation state every 0.2 Myr as the density, pressure, velocity and tracer values for each grid cell. These active and quiescent times are consistent with the observed lifetimes of radio active galactic nuclei. Shabala et al. (2008) used observations of radio galaxies to determine the typical active and quiescent timescales to be on the order of 1 Myr and 10 – 100 Myr respectively, with active time increasing and quiescent time declining with increasing stellar mass. These timescales are similar to those determined in Kaiser et al. (2000) by applying the Kaiser & Alexander (1997) and Kaiser et al. (1997) models (KA, KDA from here onwards) to a sample of 5 double-double radio galaxies. In that paper the authors assumed that $t_{\text{off}} = 1$ Myr for each source which gives plausible results for the jet power, assuming that the new jet has the same jet power as the old jet.

Finally, Turner & Shabala (2015) applied a new dynamical semi-analytic model to the same AGN sample as Shabala et al. (2008) to estimate both jet powers and timescales. These authors found that the overall trend of active and quiescent timescales agrees with Shabala et al. (2008). The active timescales are in the range 1 – 100 Myr while the quiescent timescales are in the range 10 – 1000 Myr. It is probable that the quiescent timescales in Shabala et al. (2008) and Turner & Shabala (2015) are overestimates as the authors assumed that all galaxies go through an AGN phase. These quiescent timescales are estimated from a combination of active timescales and fraction of radio-loud AGN at the host galaxy mass.

2.9 Simulation Runs

A comprehensive suite of simulations was carried out for different environments and outburst numbers. The environment parameters are shown in Table 2.1, and

2.9. SIMULATION RUNS

the constant jet parameters are shown in Table 2.2. Finally the parameters for the suite of simulations is shown in Table 2.3. The standard set of simulations filled out a 2×4 grid of parameter space of different halo masses and number of outbursts, as well as four additional sets, each of which focussed on a certain aspect of the simulations. Each simulation was given a run code in the form of **mAA.A-MBB-nC-D**, where **AA.A** is the mass of the dark matter halo for the environment, **BB** is the external Mach number of the jet, **C** is the number of outbursts, and **D** is which set of runs the simulation belongs to. For example a jet with 4 outbursts and an external Mach number of 25, in an environment with a dark matter halo mass of $M_{\text{halo}} = 10^{14.5} M_{\odot}$, has a run code of **m14.5-M25-n1**.

The standard simulations were carried out in an environment given by the Makino gas density profile, with two different dark matter halo masses: a poor group environment with a dark matter halo mass $M_{\text{halo}} = 10^{12.5} M_{\odot}$; and a cluster environment with a dark matter halo mass $M_{\text{halo}} = 10^{14.5} M_{\odot}$. Four different numbers of jet outbursts were simulated in both of these environments: 1 outburst of 40 Myr; 2 outbursts of 20 Myr each; 3 outbursts of 13.34 Myr each; and 4 outbursts of 10 Myr each. The number of outbursts is given as n , with values of $n = 1, 2, 3, 4$ respectively. For all these simulations, the jet power (Q_{jet}), injected energy (E_{total}), total active time ($t_{\text{on, total}}$), and total quiescent time ($t_{\text{off, total}}$) were all constant, with the values shown in Table 2.2.

A set of four simulations was carried out using the King gas density profile (Equation (2.16)) rather than the Makino gas density profile, for both the cluster and poor group halo mass. These simulations are used to investigate the effect of a different gas density profile on the dynamics of the jet, particularly within the central region where the profiles are significantly different. Two simulations were carried out with a faster “ramp” phase in the poor group environment to investigate whether introducing that phase significantly affects the jet dynamics. Two simulations were carried out in the cluster environment with double the θ resolution to investigate the affect of resolution on the simulations. Finally, two simulations were carried out in the poor group environment with a smaller lower radial boundary,

2.9. SIMULATION RUNS

to investigate the effect of injecting the jet closer to the core.

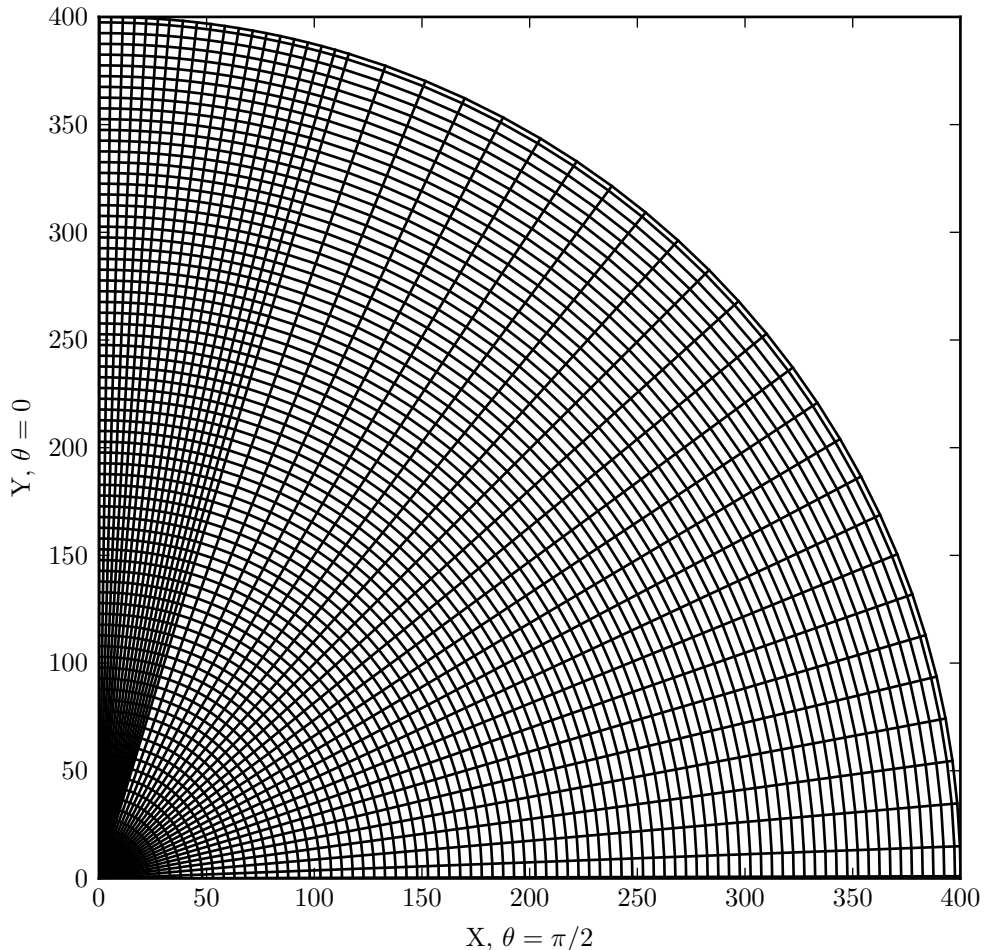


Figure 2.1: The spherical simulation grid projected onto Cartesian coordinates. Only every 25th gridline is shown in r and every 10th in θ for ease of visualization. The three grid patches in θ are clearly visible, with the resolution decreasing as θ increases. Note that the grid starts at $r = 1$, and the jet propagates in the $\theta = 0$ plane. The $\theta = 0$ and $\theta = \pi/2$ planes correspond to the Y and X axes respectively.

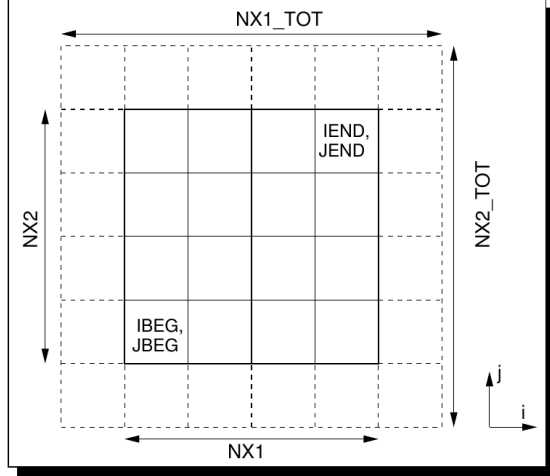


Figure 2.2: PLUTO computational grid with one layer of ghost zones. The area enclosed by the solid lines is the computational grid, while the dashed lines represent the ghost zones. Credit: Mignone et al. (2015, Figure 4.2)

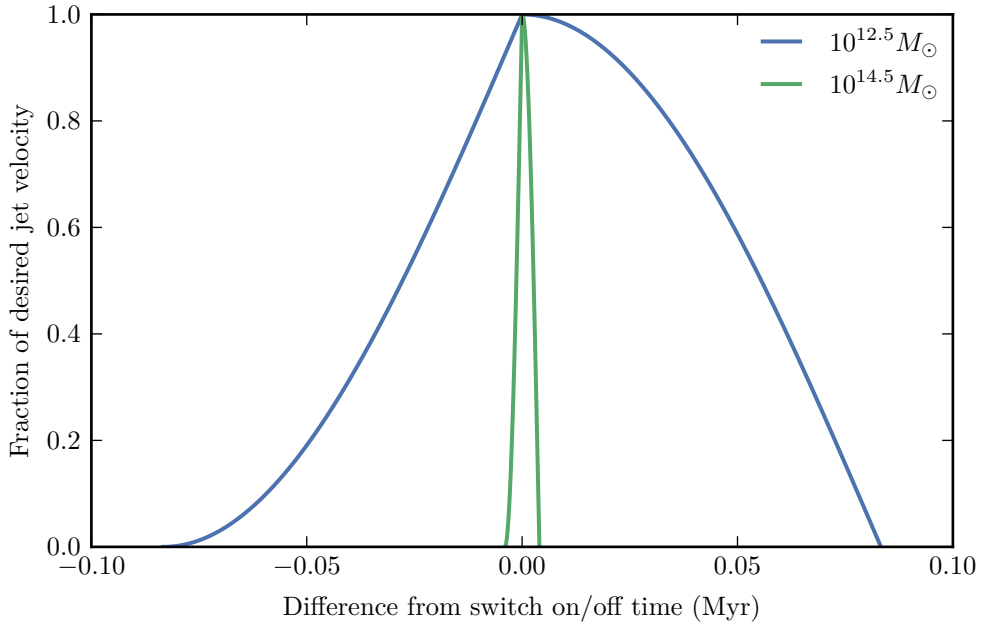


Figure 2.3: “Ramp” phase for both the cluster ($M_{\text{halo}} = 10^{14.5} M_{\odot}$) and poor group ($M_{\text{halo}} = 10^{12.5} M_{\odot}$) environments showing the jet velocity as a function of difference in time from the switch on or off point. Left portion of the plot is ramping up the jet velocity to switch the jet on, right portion of the plot is ramping down the jet velocity to switch the jet off.

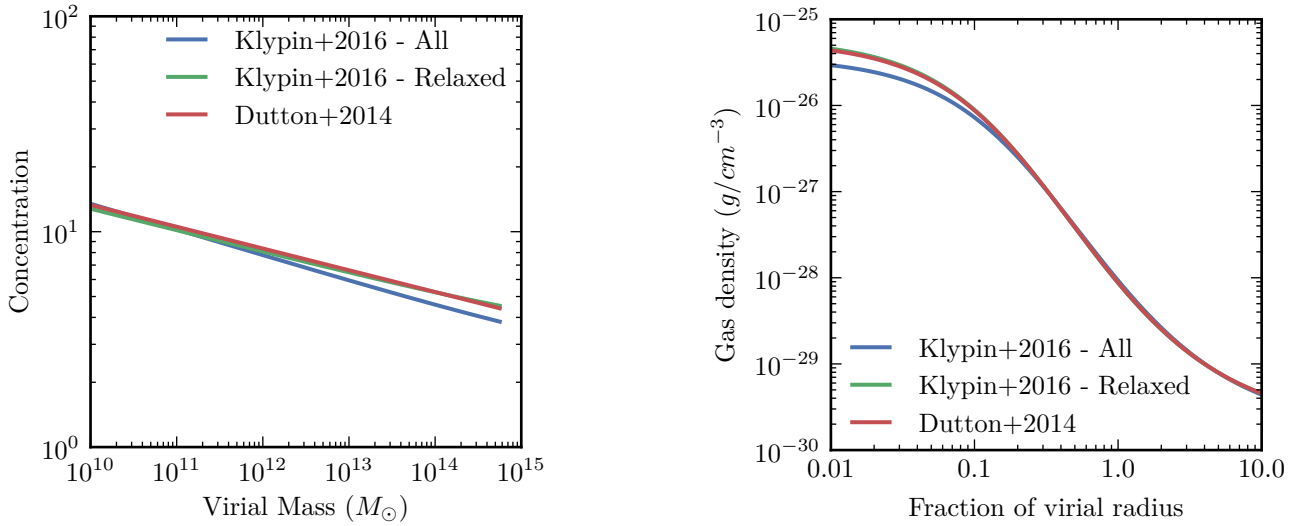


Figure 2.4: Two recent models for concentration parameter. In both plots the Klypin et al. (2016) relaxed curves are almost directly underneath the Dutton & Maccio (2014) curves.

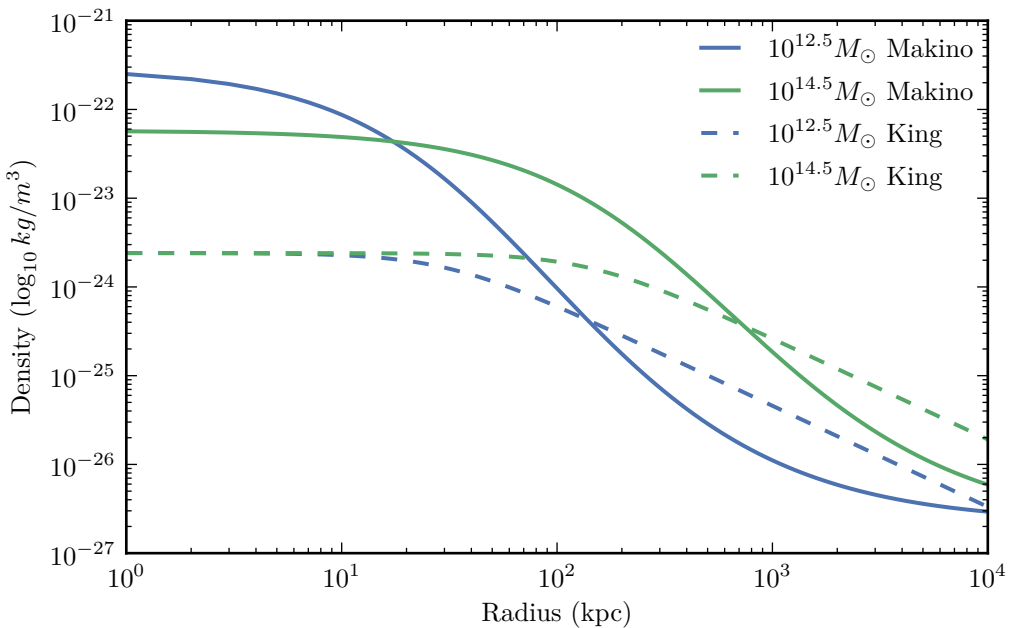


Figure 2.5: The Makino et al. (1998) and King (1962) gas density profiles for two halo masses as a function of radius from the core at $z = 0$.

Table 2.1: Table of environment parameters. M stands for the Makino et al. (1998) profile, while K stands for the King (1962) profile. M_{halo} is the mass of the dark matter halo, T_{vir} is the virial temperature, c_x is the external sound speed, ρ_0 is the central density, c is the concentration parameter, L_1 is the simulation unit length, τ is the simulation unit time, r is the scale radius for the Makino profile and the core radius for the King profile, and β is the parameter for the King profile.

Profile	M_{halo} (M_\odot)	T_{vir} (K)	c_x (km s^{-1})	ρ_0 (g/cm^3)	c	L_1 (kpc)	τ (Myr)	r_s (kpc)	β
M	12.5	1.6×10^6	1.9×10^2	2.9×10^{-25}	7.2	1.63	8.35	26.2	-
	14.5	3.4×10^7	8.9×10^2	5.8×10^{-26}	4.7	0.364	0.401	831	-
K	12.5	1.6×10^6	1.9×10^2	2.4×10^{-27}	-	17.8	91.2	1.73	0.38
	14.5	3.4×10^7	8.89×10^2	2.4×10^{-27}	-	1.78	1.96	80.5	0.38

Table 2.2: Table of constant parameters. Here Q_{jet} is the kinetic jet power, $t_{\text{on,total}}$ is total jet active time, $t_{\text{off,total}}$ is the total jet quiescent time, $\theta_{\text{half-opening}}$ is the half-opening angle of the jet, and z is the redshift.

Q_{jet} (W)	$t_{\text{on,total}}$ (Myr)	$t_{\text{off,total}}$ (Myr)	$\theta_{\text{half-opening}}$ ($^\circ$)	z
10^{37}	40	160	15	0

Table 2.3: Table of run parameters. Here M_{halo} is the dark matter halo mass, M_x is the external Mach number, and n is the number of outbursts.

Type	M_{halo} (M_\odot)	M_x	n	Run code
Standard	$10^{14.5}$	25	1	m14.5-M25-n1
			2	m14.5-M25-n2
			3	m14.5-M25-n3
			4	m14.5-M25-n4
	$10^{12.5}$	25	1	m12.5-M25-n1
			2	m12.5-M25-n2
			3	m12.5-M25-n3
			4	m12.5-M25-n4
King profile	$10^{14.5}$	25	1	m14.5-M25-n1-king
			4	m14.5-M25-n4-king
	$10^{12.5}$	25	1	m12.5-M25-n1-king
			4	m12.5-M25-n4-king
Fast “ramp”	$10^{12.5}$	25	1	m12.5-M25-n1-fast-ramp
			4	m12.5-M25-n4-fast-ramp
Close injection	$10^{12.5}$	25	1	m12.5-M25-n1-close-injection
			4	m12.5-M25-n4-close-injection
High resolution	$10^{14.5}$	25	2	m14.5-M25-n2-high-res
			3	m14.5-M25-n3-high-res

CHAPTER 3

Radio Jets in Different Environments

The dark matter halo centred around a central black hole varies dramatically in mass with the size of the surrounding structure, from $M_{\text{halo}} = 10^{12.5} M_{\odot}$ for poor groups to $M_{\text{halo}} = 10^{15} M_{\odot}$ for the largest superclusters. In this chapter I investigate the role of the environment on jet propagation and overall energetics by looking at simulations in environments described by two different dark matter halo masses. Specifically, I compare a simulation of a single outburst radio jet with an active time of 40 Myr ($n = 1$) in a **cluster** environment ($M_{\text{halo}} = 10^{14.5} M_{\odot}$, run **m14.5-M25-n1**) to that in a **poor group** environment ($M_{\text{halo}} = 10^{12.5} M_{\odot}$ run **m12.5-M25-n1**). The gas density profile used for both the environments is the Makino hydrostatic equilibrium density profile shown in Equation (2.15).

I begin by examining the jet morphology in Section 3.1, where I establish the reliability of the simulations and investigate the morphological changes between radio jets in different environments. The different morphologies affect the overall energetics of simulation; I detail these energetic differences in Section 3.2. The amount of energy injected by the jet that couples to the ambient medium is known as the feedback efficiency, which plays an important role in producing realistic galaxies with both semi-analytic galaxy formation models and hydrodynamical simulations of galaxy formation; see, e.g. Croton et al. (2006) and Vogelsberger et al. (2014) respectively. I examine the effect of environment on the feedback efficiency in Section 3.3. In Section 3.4 I explore how the simulated radio sources

3.1. MORPHOLOGY

would appear when observed, by estimating the radio luminosity of jet inflated lobes, and then making mock images of simulated sources as would be seen by a radio interferometer. I present predicted size-luminosity tracks, a standard tool for studying radio galaxies, in Section 3.5, and finally conclude in Section 3.6 with how the simulations are affected by the choice of density profile.

3.1 Morphology

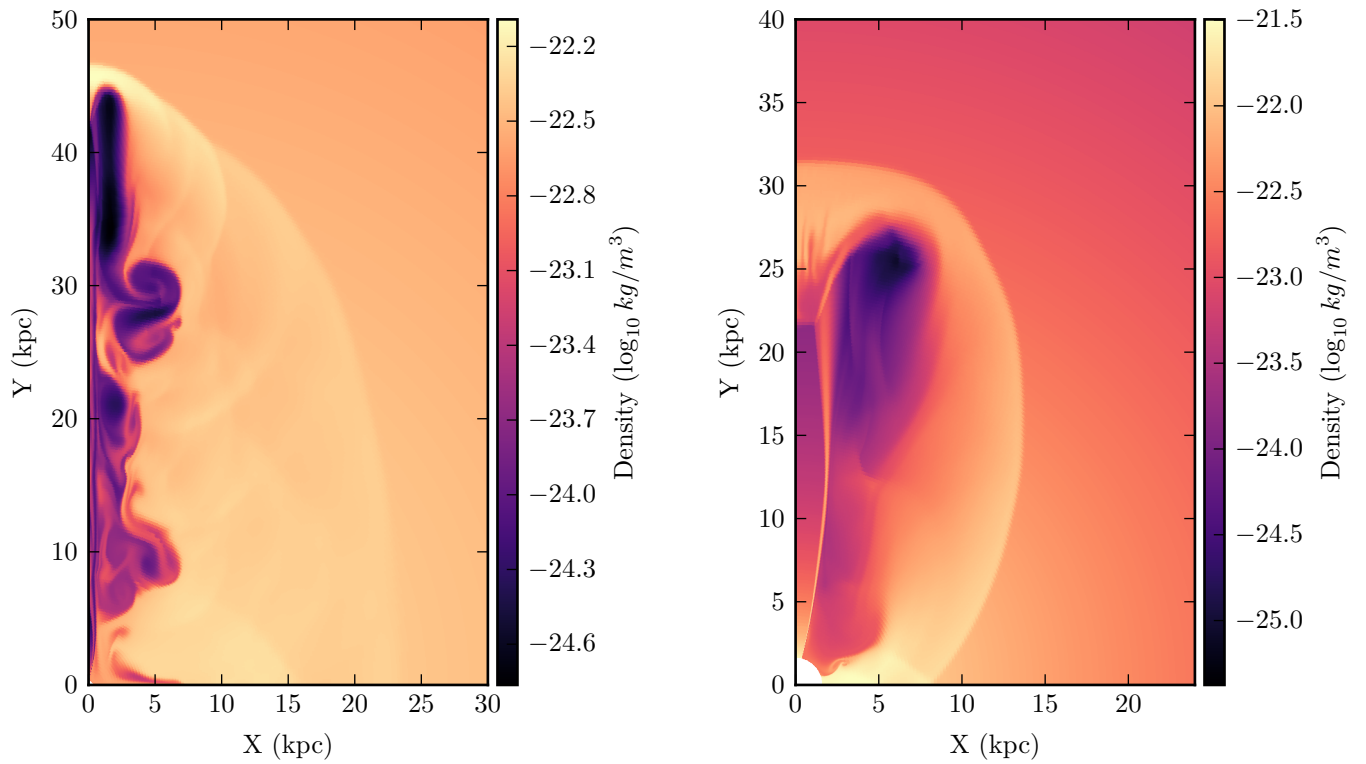


Figure 3.1: Density maps of the jet in the cluster and poor group environments at $t = 20$ Myr, half the jet active time. In both environments the jet has an FR II morphology, there are however clear differences between the two simulations.

The reproduction of FR II morphology is a basic sanity check for the simulations carried out in this thesis and confirms that the large-scale dynamics are accurately

3.1. MORPHOLOGY

captured by the simulation. The output files from PLUTO simulations contain values of the following basic simulation quantities for each grid cell: density ρ ; pressure p ; radial and azimuthal velocities v_{x1} , v_{x2} ; and tracer particles. Density most clearly shows the morphology of the resulting jet, and many of the key morphological features of an FR II radio jet discussed in Section 1.3 can be identified in the density map, shown for the cluster and poor group environments in Figure 3.1 at $t = 20$ Myr, half of the jet active time. In the following subsections I will detail the basic morphology of the jets produced by the simulations, confirm that the key morphological features of an FR II radio source are reproduced, and examine the morphological differences between jets in the two environments.

3.1.1 Shocks

There are three basic shocks described in the radio source model developed by Kaiser & Alexander (1997), hereafter the KA model. The first of these is the reconfinement or recollimation shock, which occurs downstream from the jet injection point on scales of L_{1a} as described in Section 2.1. For a conically expanding jet, the jet density drops as $\rho_j \propto 1/r^2$, and the jet collimates when the external pressure p_x is comparable to the sideways ram-pressure of the conical jet, $\rho_j v_j^2 \sin^2 \theta$, where v_j is the jet velocity and θ is the half-opening angle. The recollimation shock front itself is not visible in the density maps for either environment; however the jet has collimated in both cases. The effect of recollimation is most visible in the poor group environment (Figure 3.1b) due to the larger recollimation scale (compared to the cluster, see Figure 3.1a), and the recollimation itself occurs around $Y = 14$ kpc; this large recollimation distance results in a wide jet. The recollimation distance is in agreement with the recollimation length scale for the poor group environment of $L_{1a} = 14.76$ kpc. The jet in the cluster collimates on length scales of $L_{1a} = 3.30$ kpc as shown in Figure 3.1a. The larger L_{1a} for the poor group is due to the lower external pressure p_x in the poor group environment compared to the cluster, which is seen in the pressure maps for both environments, as shown in Figure 3.2.

The second shock in the KA model for radio jets is the jet shock or termination

3.1. MORPHOLOGY

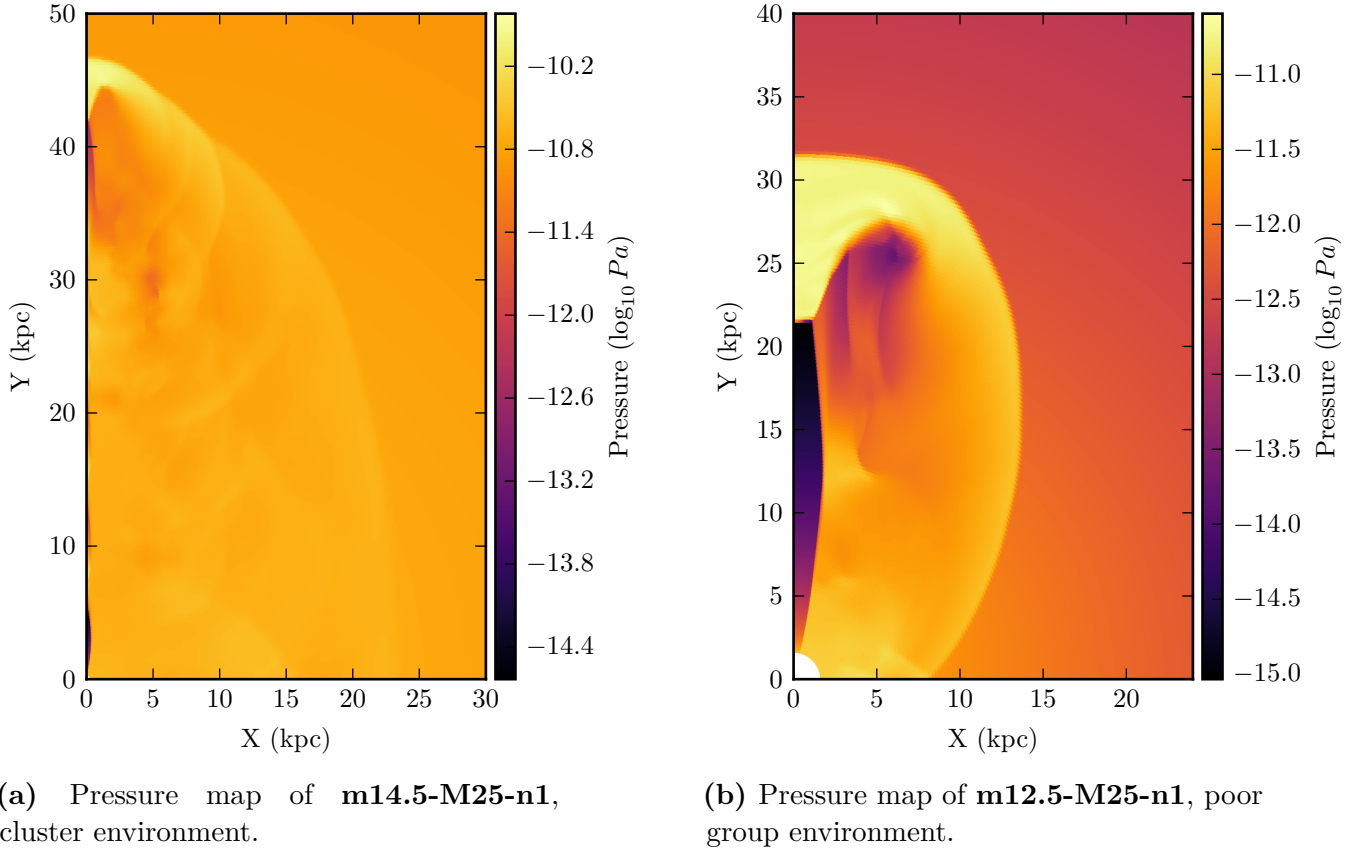


Figure 3.2: Pressure maps of the jet in the cluster and poor group environments, for the same time as Figure 3.1.

shock. This shock occurs at the head of the jet as a roughly transverse discontinuity across the jet which then curves in the direction of jet propagation and continues for a few kpc. It is most visible in the pressure map; however it is also visible in the density (Figure 3.1) and velocity (Figures 3.3 and 3.4) maps. The jet shock occurs at around $Y = 43$ kpc for the jet in the cluster environment (Figure 3.2a) and around $Y = 22$ kpc for the jet in the poor group environment (Figure 3.2b).

The final shock described in the KA model is the bow shock, which separates the shocked gas from the unshocked ambient medium and is the rightmost feature in Figures 3.1 to 3.4. The bow shock of the jet in the poor group environment is tapered towards the lower injection boundary, compared to the jet in the cluster

3.1. MORPHOLOGY

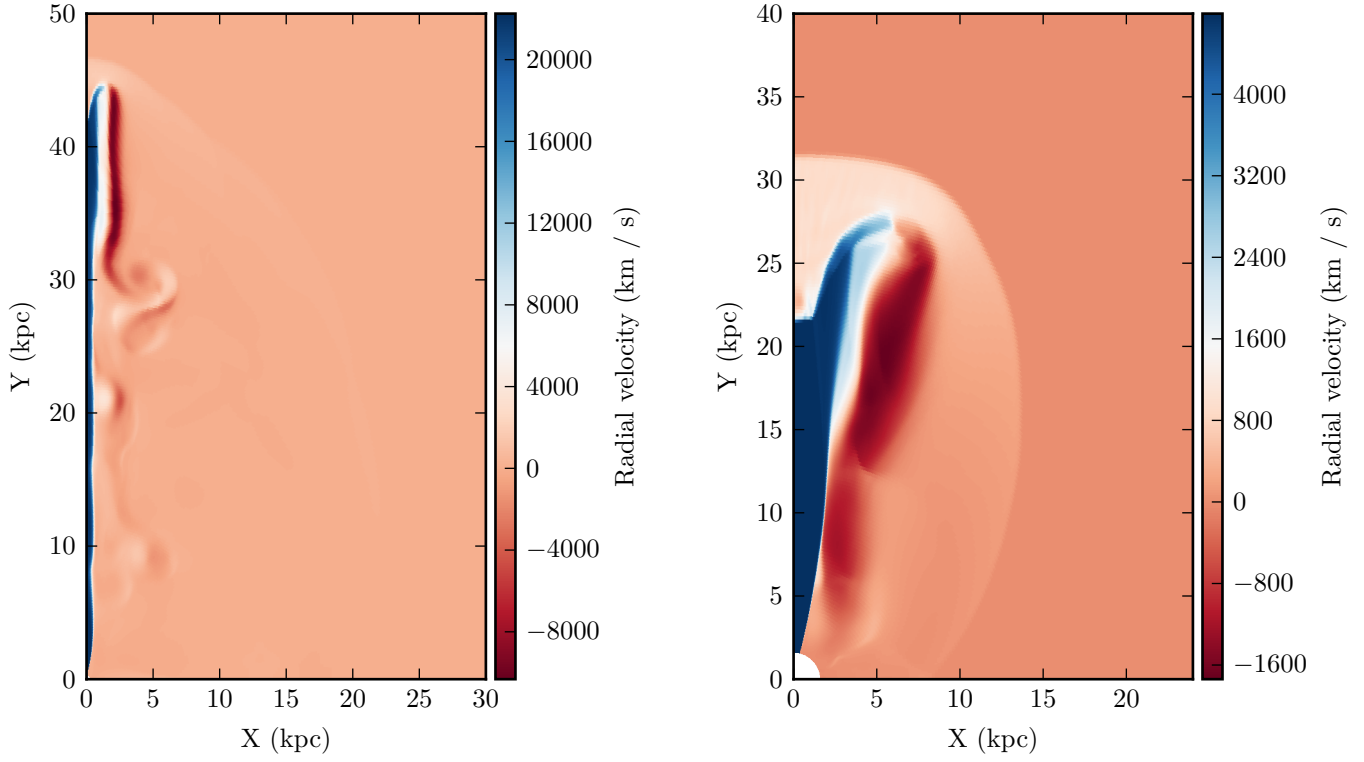
environment which is tapered towards the head of the jet. This difference is probably because the gas density starts falling closer to the core in the poor group, which means that segments of the bow shock will travel faster, the greater their distance from the core. At later times the bow shock of the jet in the poor group environment approaches a spherical shape as shown in the density and pressure time series (Figures 3.8 and 3.10 respectively), which is expected due to the spherically symmetric gas density profile used for the environment. The same spherical shape would likely be seen for the bow shock of the jet in the cluster environment if the simulated time was longer.

3.1.2 Hotspot and Backflow

A key feature of FR II radio jets as described by the KA model is the hotspot at the end of the jet, after the termination shock. This region is characterised by high pressure, and is the working surface over which the jet distributes its forwards ram pressure. For the jet in the cluster environment, the hotspot occurs at around $Y = 45$ kpc as shown by the pressure map in Figure 3.2a, while for the jet in the poor group environment it occurs at around $Y = 25 - 30$ kpc as shown by the pressure map in Figure 3.2b. The KA model predicts the hotspot to have a pressure equal to that of the shocked gas surrounding the hotspot. This is found to be true for jet simulations in both the cluster and the poor group environments.

Due to the high pressure of the hotspot, a backflow of jet material flowing into the lower pressure cocoon is predicted by the KA model. This backflow is present in the simulations, and is visible in the radial and azimuthal velocity maps for both environments as shown by the negative radial velocities to the upper-right of the hotspot for both environments in Figure 3.3, and the positive azimuthal velocities near the same region in Figure 3.4. The backflow for the jet in the poor group environment is significantly wider than that of the cluster environment, which is likely due to the wider jet width and subsequently larger working surface in the poor group.

3.1. MORPHOLOGY



(a) Radial velocity map of **m14.5-M25-n1**, cluster environment.

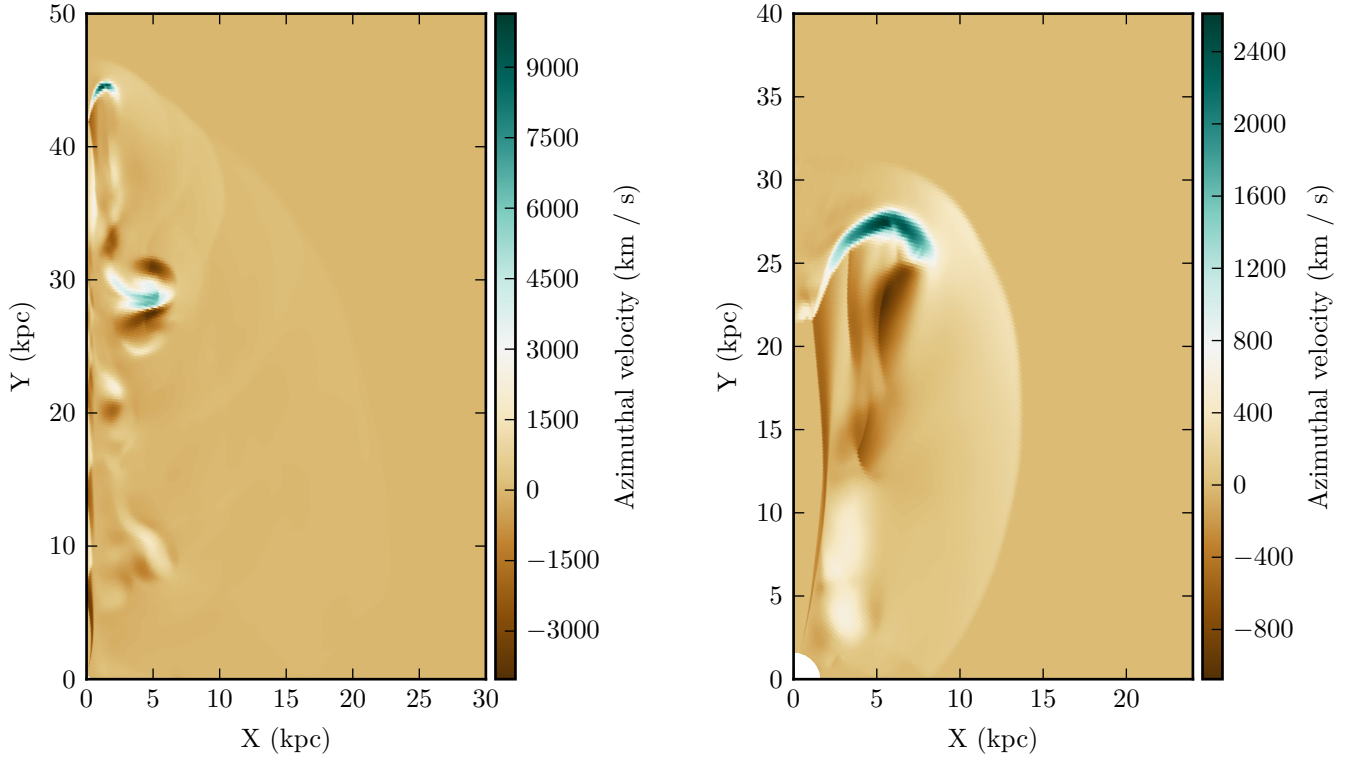
(b) Radial velocity map of **m12.5-M25-n1**, poor group environment.

Figure 3.3: Radial velocity maps of the jet in the cluster and poor group environments, for the same time as Figure 3.1. A positive radial velocity is moving away from the centre region (lower left corner of the plot), while a negative radial velocity is moving towards the centre region. For reference, Figure 2.1 shows the simulation gridlines.

3.1.3 Cocoon and Instabilities

The backflow of material from the hotspot inflates a cocoon of jet material, also known as the lobe of a radio source. This is best seen in the areas of low pressure adjacent to the jet in Figure 3.1 which extend radially from the backflow area down towards the injection point for the jet in both environments. There is a velocity shear surface between the jet beam and the cocoon which leads to Kelvin-Helmholtz instabilities that could potentially disrupt the jet; however the jets in both environments prove to be stable in the simulations. Roll-ups due to these Kelvin-Helmholtz instabilities at the velocity shear surface are most visible for the

3.1. MORPHOLOGY



(a) Azimuthal velocity map of **m14.5-M25-n1**, cluster environment.

(b) Azimuthal velocity of **m12.5-M25-n1**, poor group environment.

Figure 3.4: Azimuthal velocity maps of the jet in the cluster and poor group environments, for the same time as Figure 3.1. A positive azimuthal velocity is moving away from the $\theta = 0$ plane (the Y-axis) towards the $\theta = \pi/2$ plane (the X-axis). For reference, Figure 2.1 shows the simulation grid.

jet in the cluster environment due to the greater velocity difference across the shear surface. Figure 3.7 shows the time evolution of the Kelvin-Helmholtz instabilities for the jet in the cluster.

A contact discontinuity separates the jet material that makes up the cocoon from the shocked gas. This is clearest for the density map of the jet in the cluster (Figure 3.1a) which shows a distinct discontinuity between the low density cocoon material and the high density shocked gas. The cocoon and shocked gas are expected to undergo mixing as a result of the Rayleigh-Taylor instability, since the cocoon material is underdense compared to the shocked gas. This mixing is present for the jet simulations in both environments, however, at time $t = 20$ Myr,

3.1. MORPHOLOGY

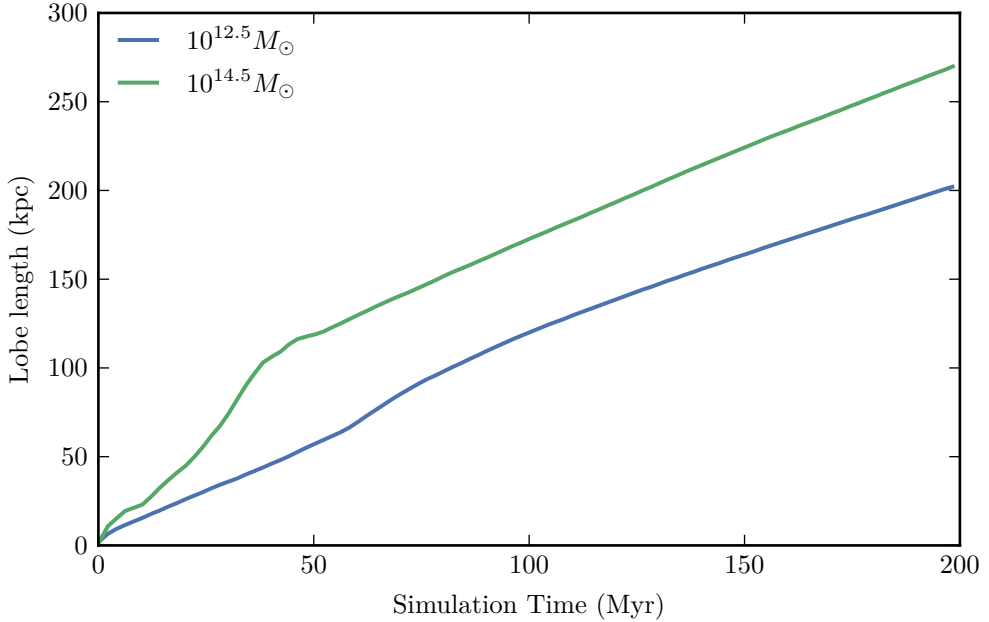


Figure 3.5: Lobe length as a function of simulation time for the $n = 1$ jet in a cluster and poor group, run codes **m14.5-M25-n1** and **m12.5-M25-n1**.

only the cocoon in the cluster environment has begun to mix with the shocked gas, as is shown in Figure 3.1a.

3.1.4 Jet Evolution

The evolution of the jet structure over time in the cluster environment is shown by the density and pressure maps in Figures 3.7 and 3.9 respectively, and can be compared to that in the poor group environment with Figures 3.8 and 3.10. The jet in the cluster environment is expected to propagate faster than the jet in the poor group environment. This is due to the narrower collimated jet in the cluster, which has a smaller working surface at the jet head over which the forwards ram pressure of the jet is distributed, making it easier for the jet to “punch through” the environment. The difference in propagation speeds can be measured by quantifying the lobe (cocoon) length as a function of time for both environments, as shown in Figure 3.5. The lobe length is calculated as the grid cell with the largest radial

3.1. MORPHOLOGY

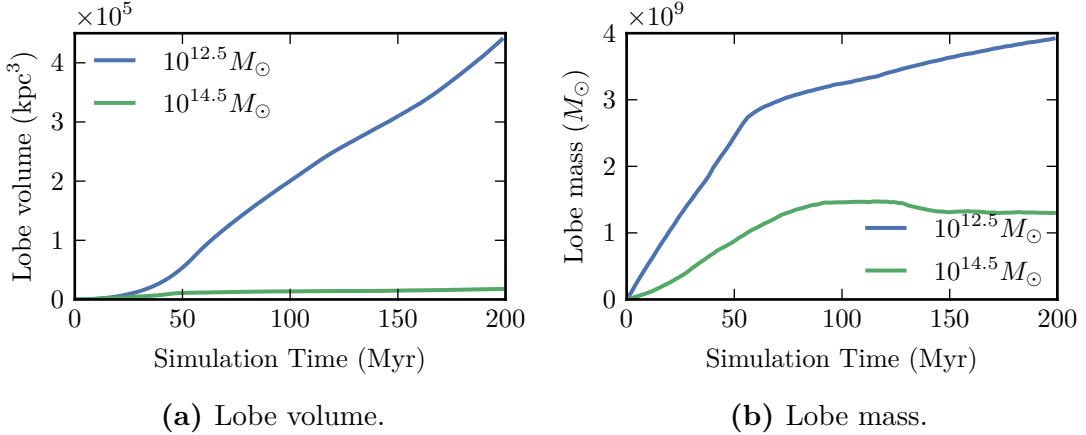


Figure 3.6: Lobe volume and mass for the poor group and cluster environments, runs **m12.5-M25-n1** and **m14.5-M25-n1**.

distance from the core, along the plane $\theta = 0$, that contains a jet tracer value above the chosen threshold value. The tracer cutoff is chosen to be 5×10^{-3} (for comparison, Hardcastle & Krause (2013) used a tracer cutoff of 10^{-3}), however the results presented here are not sensitive to the exact value used, provided it is significantly smaller than unity; this is not the case for the feedback efficiency, as discussed later in Section 3.3. The jet in the cluster propagates faster and inflates a longer lobe compared to the jet in the poor group, as shown in Figure 3.5. The effect of the jet switching off at $t = 40$ Myr on the lobe length is visible for the cluster environment as a kink in the lobe length curve, while no such feature is visible for the poor group environment. This is likely due to the jet in the cluster having a smaller working surface, so that the forwards ram pressure of the jet has a larger effect on the propagation. In the poor group the working surface is much larger so the forwards ram pressure is distributed over a larger area and therefore the jet has less effect on lobe expansion speed.

The different morphologies in Figure 3.1 suggest that the lobe volume of the jet in the poor group should be greater than that of the jet in the cluster due to the significant differences in lobe width. The lobe volume is calculated in a similar way to the lobe length, by classifying every cell with a jet tracer value greater than the cutoff as lobe material and then summing up the total cell volume

3.1. MORPHOLOGY

over the lobe. The evolution of the lobe volume as a function of time for both environments, shown in Figure 3.6a, shows that the volume of the lobe in the poor group environment is significantly greater than that of the cluster environment, as expected. The mass of the lobe is calculated from the lobe volume and cell density, and the evolution over time is shown in Figure 3.6b. While the lobe volumes are significantly different, the lobe masses are similar between the environments. This is expected due to the higher average density in the cluster environment compared to the group environment.

Once the jet is switched off, the cocoon continues to expand in both environments and the jet channel fills in, as shown in Figures 3.7 to 3.10. The bubble of underdense material formed by closing off the jet channel theoretically rises at approximately half the sound speed of the environment. This is true for both environments, and can be checked by tracking the lower edge of the underdense material in Figures 3.7 and 3.8.

In the cluster environment, the bulk of the low-density material closest to the centre is at a radius of 150 kpc at time 120 Myr, and at a radius of 170 kpc at time 150 Myr, corresponding to a rise speed of approximately $0.67 \text{ kpc Myr}^{-1}$. This is approximately half the sound speed of the cluster environment $0.46 \text{ kpc Myr}^{-1}$, where $c_x = 0.91 \text{ kpc Myr}^{-1}$. The same can be done for the poor group environment, where the bulk of the low-density material is at a radius of 10 kpc at time 120 Myr, and at a radius of 15 kpc at time 150 Myr. This gives a rise speed of approximately $0.167 \text{ kpc Myr}^{-1}$, compared to the sound speed in the poor group environment of $c_x = 0.20 \text{ kpc Myr}^{-1}$.

This page was intentionally left blank so that Figures 3.7 and 3.8 may be compared side-by-side.

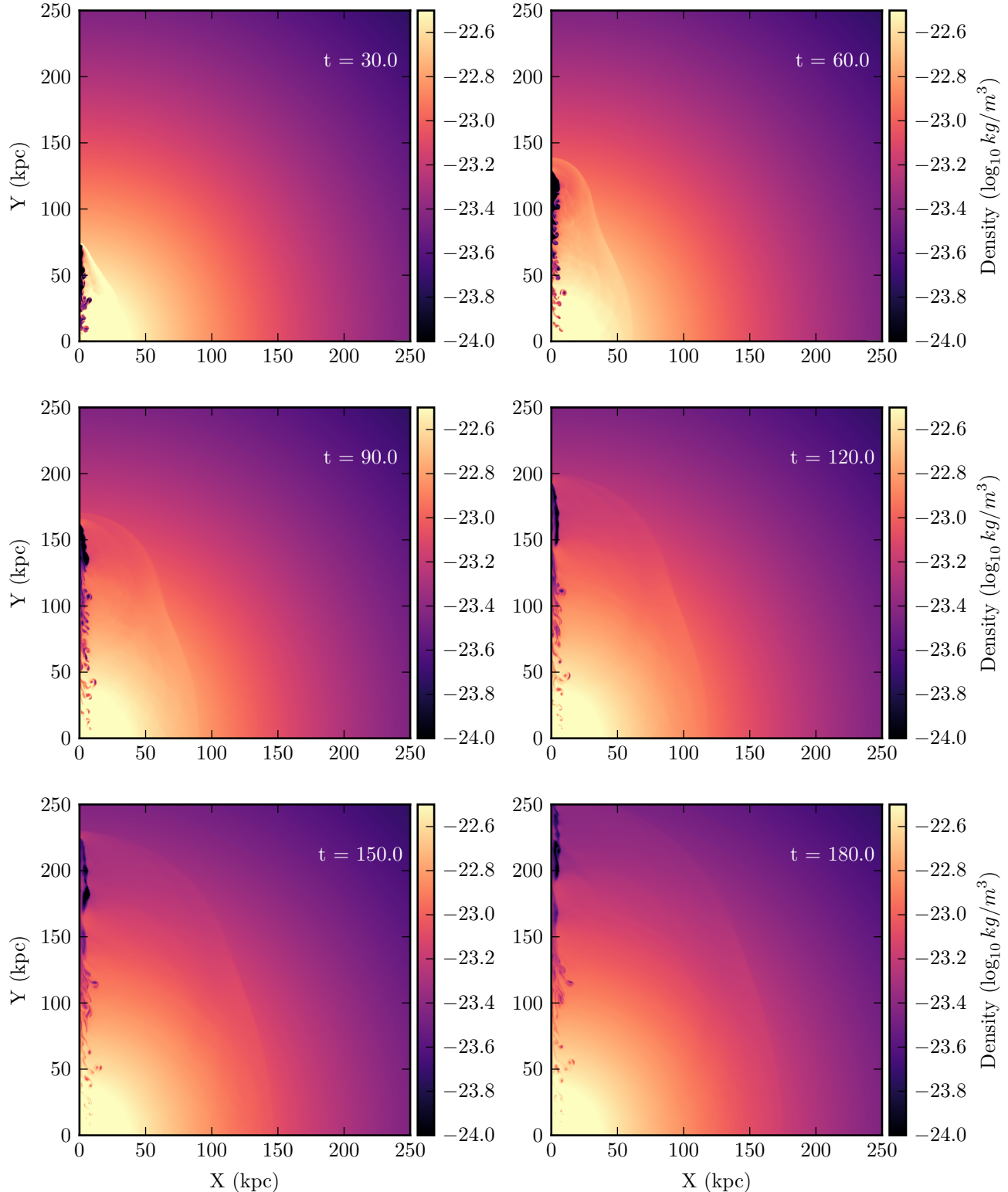


Figure 3.7: Density maps for 6 different simulation times, $t = 30, 60, 90, 120, 150$ and 180 Myr for $n = 1$ in a cluster environment, run code **m14.5-M25-n1**. The jet is switched on from $t = 0$ to $t = 40$ Myr.

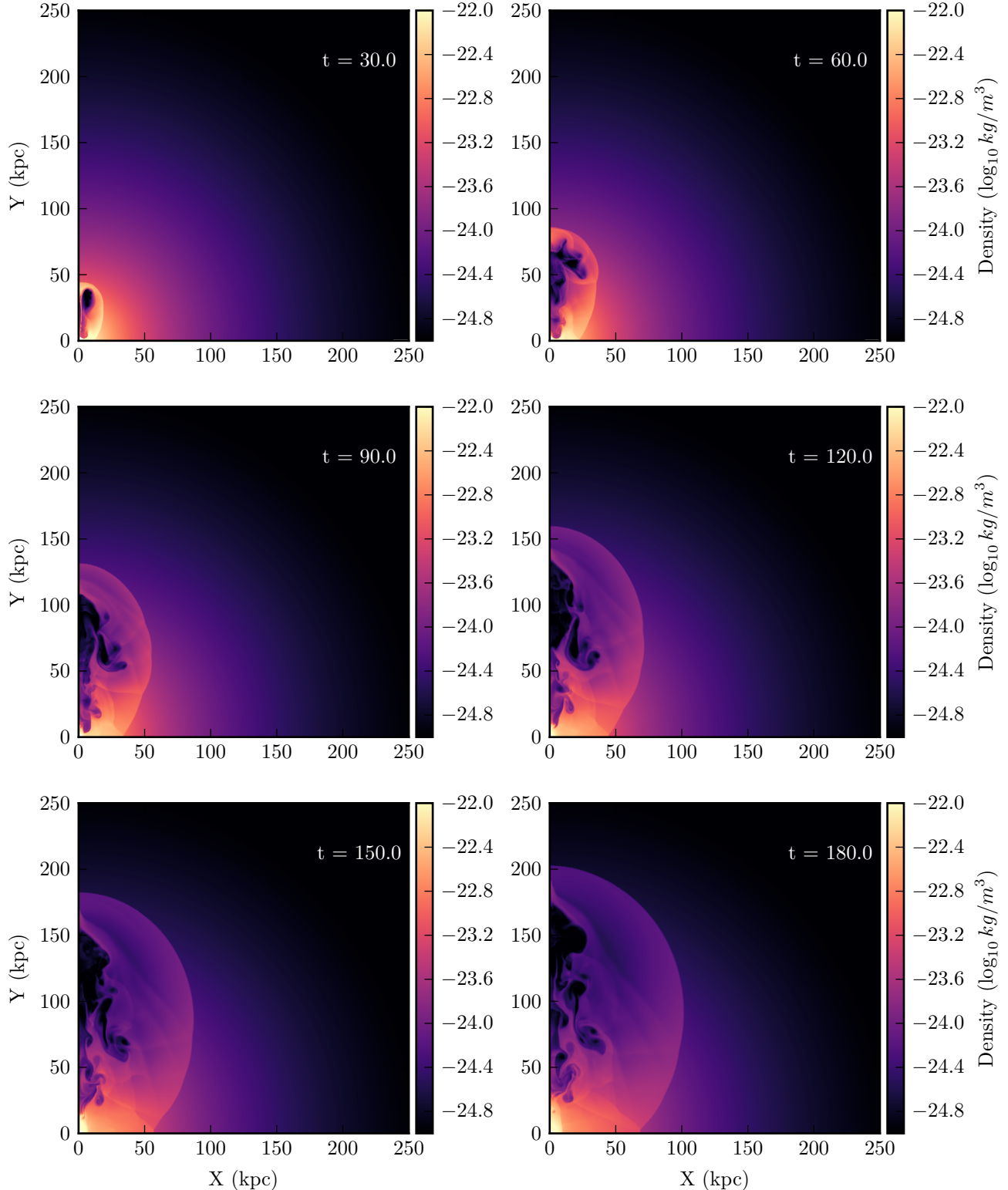


Figure 3.8: Density maps for 6 different simulation times, $t = 30, 60, 90, 120, 150$ and 180 Myr for $n = 1$ in a poor group environment, run code **m12.5-M25-n1**. The jet is switched on from $t = 0$ to $t = 40$ Myr.

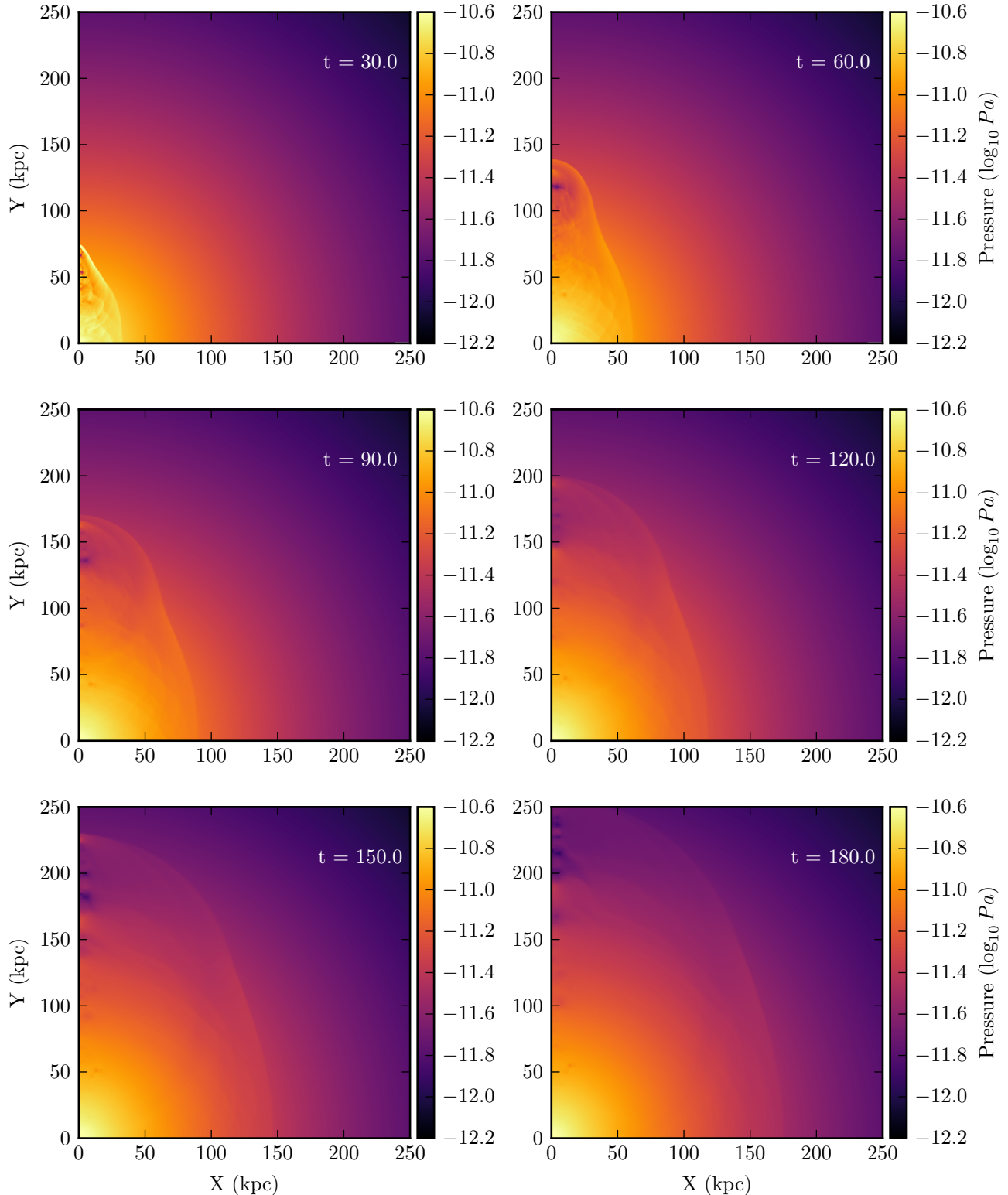


Figure 3.9: Pressure maps for 6 different simulation times, $t = 30, 60, 90, 120, 150$ and 180 Myr for $n = 1$ in a cluster environment, run code **m14.5-M25-n1**. The jet is switched on from $t = 0$ to $t = 40$ Myr.

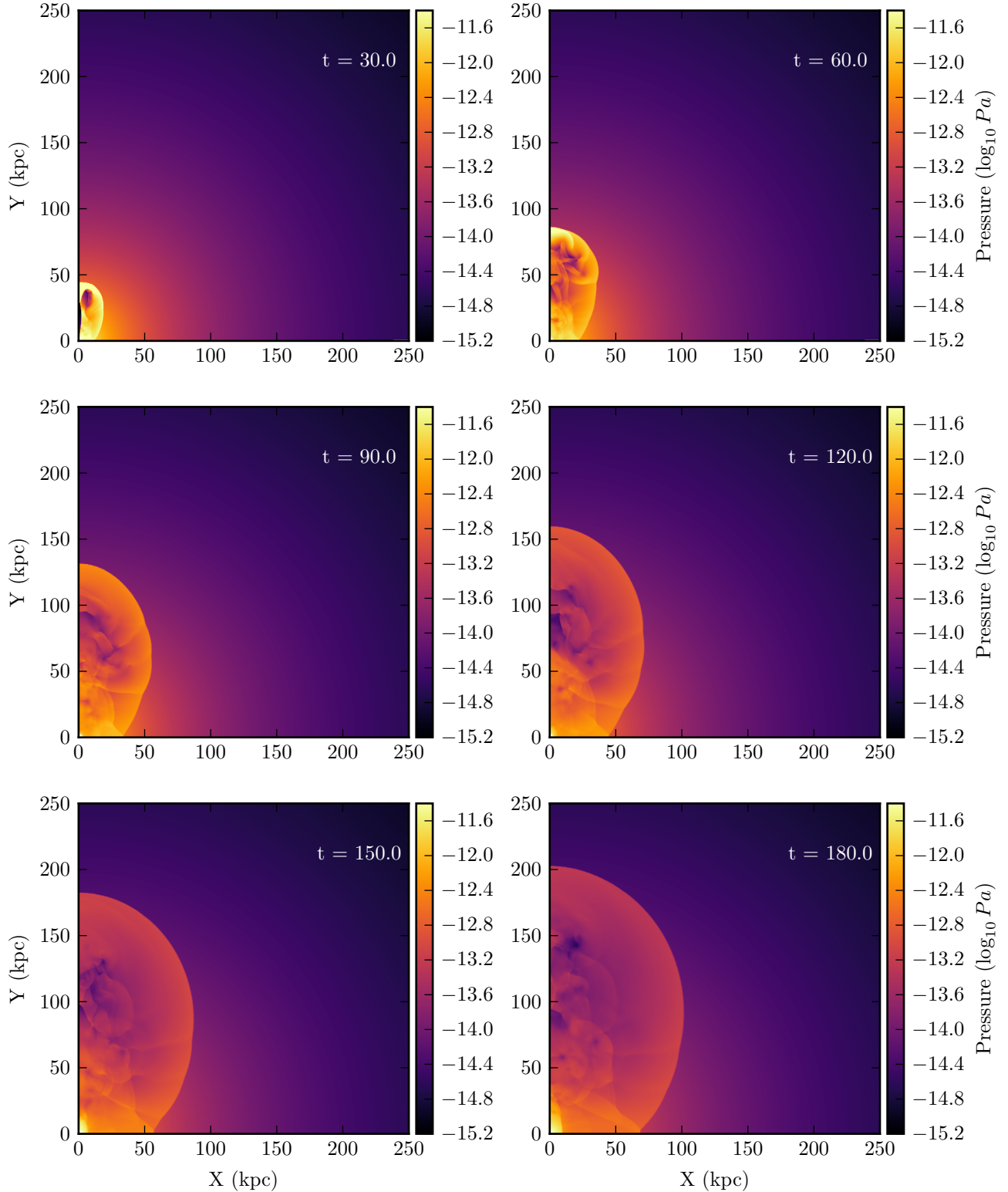


Figure 3.10: Pressure maps for 6 different simulation times, $t = 30, 60, 90, 120, 150$ and 180 Myr for $n = 1$ in a poor group environment, run code **m12.5-M25-n1**. The jet is switched on from $t = 0$ to $t = 40$ Myr.

3.1. MORPHOLOGY

3.1.5 Simulation reliability

An important aspect of the simulations that I have only briefly discussed so far is their reliability. In this subsection I begin by examining the grid resolution used for the standard suite of simulations with reference to a resolution study, and then investigate the effect of the jet injection radius and jet ramping timescale on the jet structure.

Resolution Study

Four simulations were carried out to study the influence of grid resolution on the jet structure and propagation. These simulations are shown in Figure 3.11, with the total resolution increasing with each plot from left to right. I will only discuss the two extremes in resolution as the changes due to resolution are continuous over the centre two plots. The environment used in these simulations is a homogeneous, constant density environment, with the jet injected as a cylindrical boundary condition; the results are however still applicable to the hydrostatic equilibrium density profiles used in the main suite of simulations.

The most prominent change going from low resolution to high resolution is the ability of the simulation to accurately capture fluid instabilities. The lowest resolution simulation (Figure 3.11, far left) has an unrealistically smooth contact discontinuity between the underdense cocoon and the surrounding shocked gas. On the other hand, the highest resolution simulation (Figure 3.11, far right) is able to capture the Rayleigh-Taylor instabilities that occur at the contact discontinuity, and correctly reproduces the mixing effect of the cocoon with the shocked gas. The dynamics of the jet beam also change with resolution: the lowest resolution simulation has a smooth jet beam, while the highest resolution simulation is able to capture the instabilities and turbulence in the jet beam.

The speed of jet propagation and cocoon expansion also changes with resolution; the jet in the lowest resolution simulation propagates significantly faster than the jet in the highest resolution simulation. This is mainly due to two factors: the

3.1. MORPHOLOGY

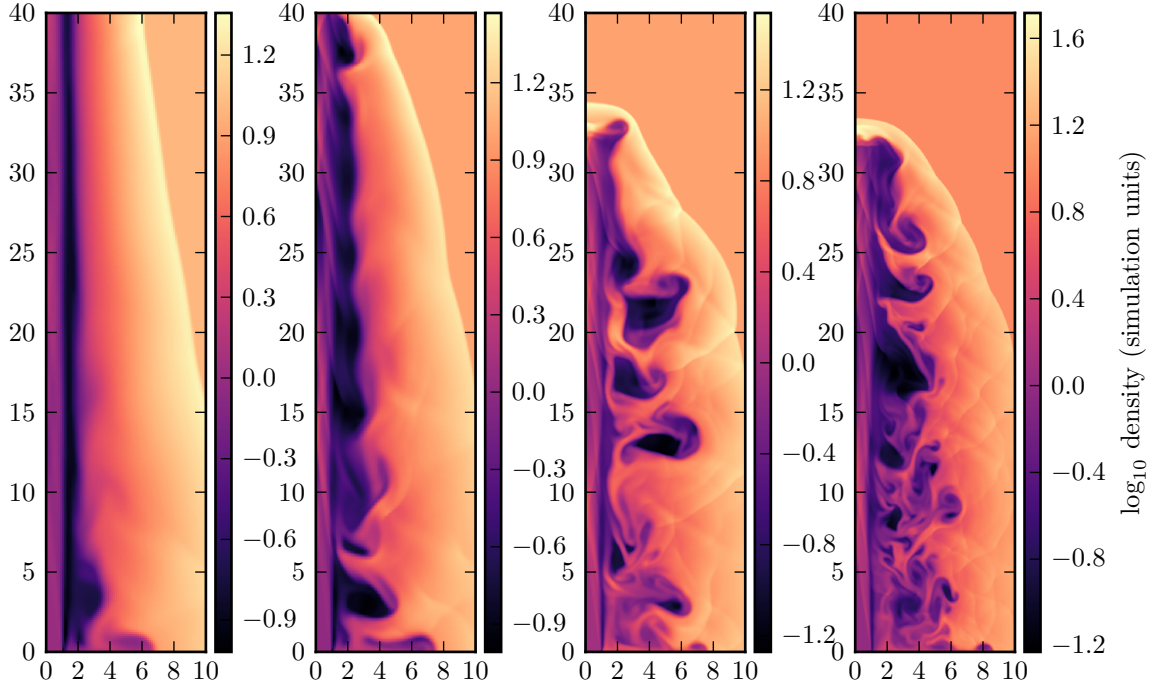


Figure 3.11: Density maps of a jet in a constant density environment. The simulation time is the same for all four plots. The grid resolution increases with each plot from left to right. Higher resolution allows the simulation to capture the fluid instabilities present in the jet.

first is because there is insufficient resolution to accurately resolve the working surface of the jet in the lowest resolution simulation and so the jet's forwards ram pressure is distributed over a smaller area. The second reason is due to the lack of instabilities and turbulence in the lowest resolution simulation, which would disrupt the jet and slow the speed of its propagation.

Comparing the four density plots of differing resolution in Figure 3.11 to the density plots of the standard **m14.5-M25-n1** and **m12.5-M25-n1** runs in Figure 3.1 gives an indication of whether the chosen resolution is sufficient. The fluid instabilities are shown to be correctly captured in Figure 3.1, particularly the Rayleigh-Taylor instability at the contact discontinuity between the cocoon and the shocked gas. In addition, the jet beam in Figure 3.1 does not display the unrealistic smoothness

3.1. MORPHOLOGY

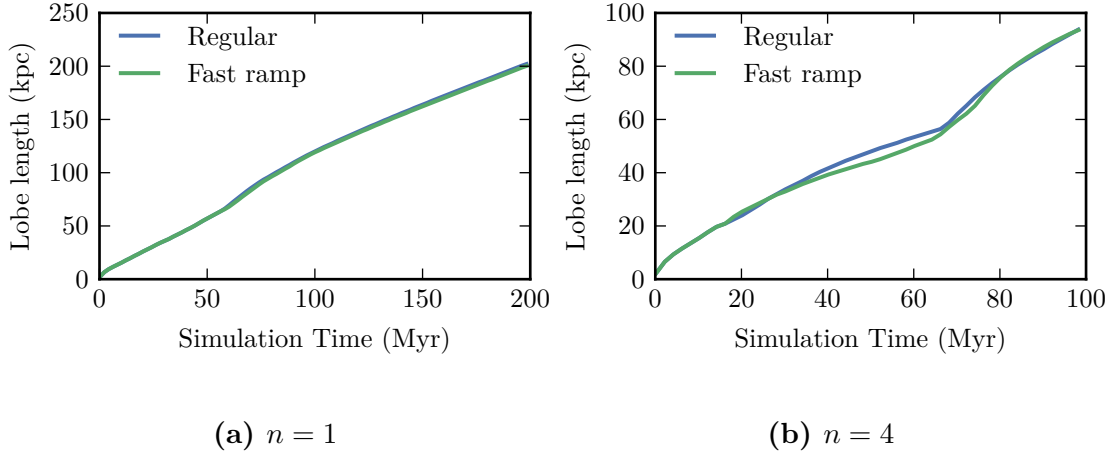


Figure 3.12: Lobe length as a function of simulation time for the $n = 1$ and $n = 4$ jets in the poor group environment. The standard simulation setup (runs **m12.5-M25-n1** and **m12.5-M25-n4**, the blue curve in both plots) is compared to a fast ramp setup (runs **m12.5-M25-n1-fast-ramp** and **m12.5-M25-n4-fast-ramp**, the green curve in both plots).

exhibited in the lowest resolution simulation (Figure 3.11, far left). These two metrics indicate that the resolution used for the standard runs is sufficient to fully capture the jet dynamics.

Ramping Timescale Study

The method used to restart the jet ramps the injected velocity up or down over a short timescale to prevent errors with the simulation, as discussed in Section 2.5. The timescale used is $\Delta t = 0.01$ simulation time units, which is small compared to the jet active times, and should not significantly affect the resulting jet morphology. This ramping timescale in simulation units translates to $\Delta t = 4.01 \times 10^{-3}$ Myr for the cluster environment, and $\Delta t = 8.35 \times 10^{-2}$ Myr for the poor group environment. To examine how this timescale affects the jet structure, I ran two simulations in the poor group environment (**m12.5-M25-n1-fast-ramp** and **m12.5-M25-n4-fast-ramp**) which are identical to their standard counterparts (**m12.5-M25-n1** and **m12.5-M25-n4**) except that the physical ramping timescale is set to that for the cluster, $\Delta t = 4.01 \times 10^{-3}$ Myr.

3.1. MORPHOLOGY

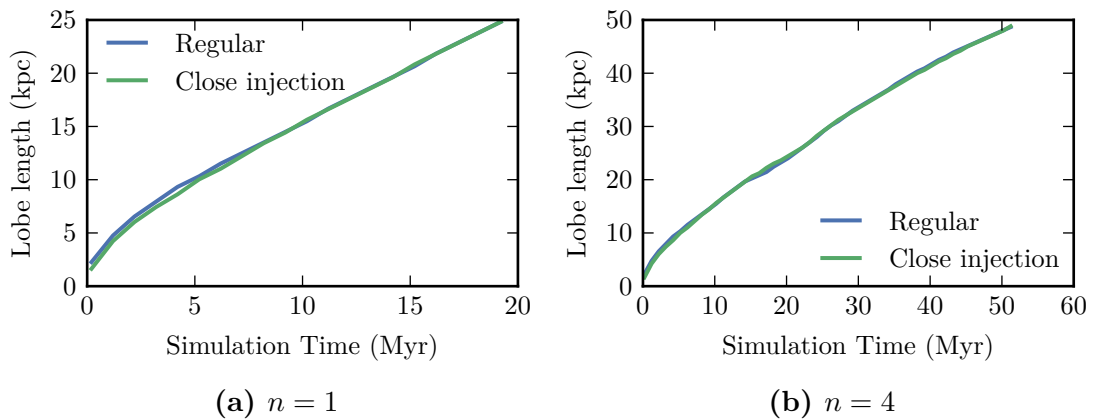


Figure 3.13: Lobe length as a function of simulation time for $n = 1$ and $n = 4$ jets in the poor group environment. The blue curve in each plot is the standard simulation setup (runs **m12.5-M25-n1** and **m12.5-M25-n4**), which is compared to the close injection setup (runs **m12.5-M25-n1-close-injection** and **m12.5-M25-n4-close-injection**), the green curve in each plot.

The evolution of the lobe length as a function of time for both the standard and fast ramp simulations is shown in Figure 3.12. The evolution of the single outburst jet shown in Figure 3.12a is practically unaffected by a shorter ramping timescale; however the effect is more noticeable for the multiple outburst jet, shown in Figure 3.12b, since the jet is restarted a greater number of times. For both numbers of outbursts the shorter ramping timescale does not significantly affect the jet morphology and so using $\Delta t = 0.01$ simulation time units for the standard set of simulations is justified.

Injection Point Study

The jet is injected onto the grid as a mass inflow boundary condition on the lower radial boundary, as is discussed in Section 2.3. The value of this lower radial boundary is chosen to be $r = 1.0$ in simulation units for the standard set of simulations. This value corresponds to a physical injection radius of $r = 0.36$ kpc in the cluster environment, and $r = 1.63$ kpc in the poor group environment, as set by the unit length L_1 . The collimation length scale L_{1a} as described in Section 2.1 is generally at least an order of magnitude greater than L_1 , so choosing L_1 as the

3.2. ENERGY COMPONENTS AND DISTRIBUTION

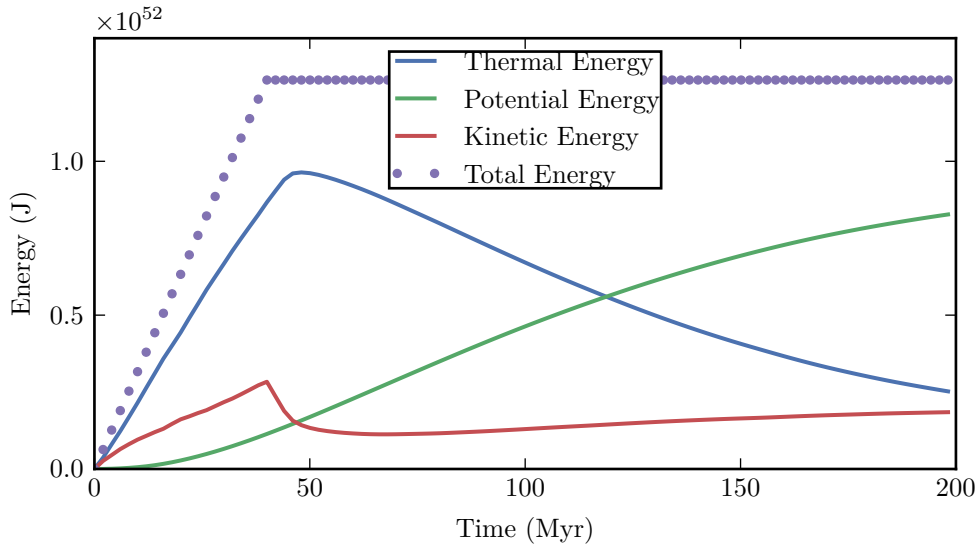


Figure 3.14: Total change of energy in the thermal, gravitational potential and kinetic energy components as well as the overall sum as a function of simulation time for $n = 1$ in a cluster environment, run code **m14.5-M25-n1**.

injection radius is not likely to affect the jet structure.

Two simulations were carried out in the poor group environment with a physical jet injection radius of $r = 0.36$ kpc, the physical injection radius in the cluster environment, to investigate the effect this closer injection radius would have on the resulting jet morphology. These two simulations, runs **m12.5-M25-n1-close-injection** and **m12.5-M25-n4-close-injection**, are otherwise identical to their equivalent standard simulations, runs **m12.5-M25-n1** and **m12.5-M25-n4**. The evolution of lobe length as a function of time for both the close injection runs and their standard counterparts is shown in Figure 3.13. It is clear that the resulting lobe length of the jet does not change significantly with a closer injection point, and so injecting the jet at a radius of L_1 is justified.

3.2 Energy Components and Distribution

The energy injected by the jet is calculated in each grid cell for the kinetic, gravitational potential and thermal components as

3.2. ENERGY COMPONENTS AND DISTRIBUTION

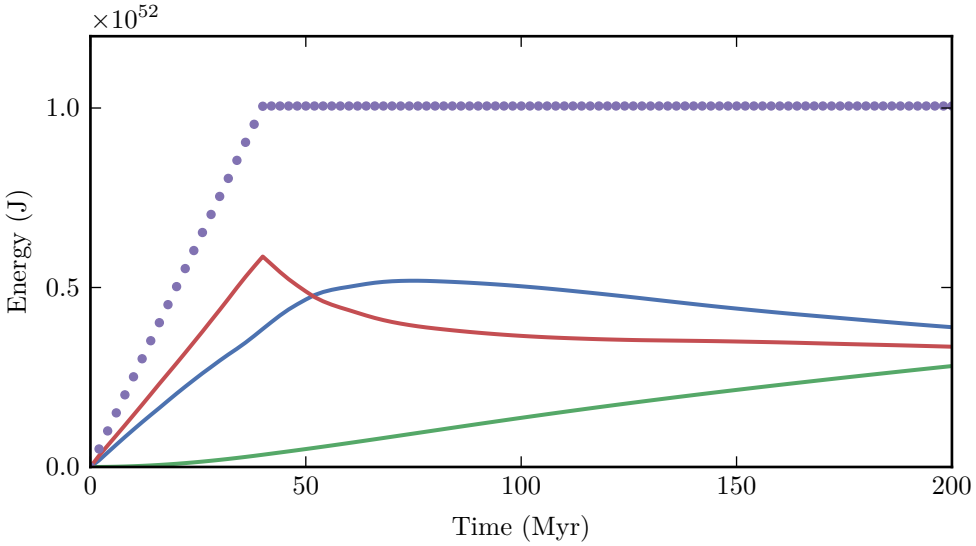


Figure 3.15: Total change of energy in the thermal, gravitational potential and kinetic energy components as well as the overall sum as a function of simulation time for $n = 1$ in a poor group environment, run code **m12.5-M25-n1**. The legend is the same as the one in Figure 3.14.

$$dE_{\text{kin}} = \frac{1}{2}\rho V v^2 \quad (3.1)$$

$$dE_{\text{pot}} = \frac{-\ln(\rho_g(r))\rho V}{\gamma} \quad (3.2)$$

$$dE_{\text{therm}} = \frac{3}{2}PV \quad (3.3)$$

where ρ is the density of the cell, V is the cell volume, v is the cell velocity and P is the cell pressure. The gravitational potential for the gas in hydrostatic equilibrium with the dark matter halo is given by $\frac{\ln(\rho_g(r))}{\gamma}$ as shown in Appendix A. The initial energy in the system (at $t = 0$) is subtracted from the calculated energy in each cell to obtain the change in energy due to the jet. This change in energy is then summed over the entire simulation grid to obtain total energies for each of the different components.

The energy injected into the system as a function of time for the cluster environment is shown in Figure 3.14, while the energy injected into the system as a function of

3.2. ENERGY COMPONENTS AND DISTRIBUTION

time for the poor group environment is shown in Figure 3.15. The top dotted curve in both figures is the total injected energy in the simulation, which is obtained from summing the kinetic, gravitational potential and thermal energies. The total injected energy curve has a linear slope when the jet is switched on. The value of this slope is the jet power. Once the jet is switched off the total energy in the simulation grid remains constant, indicating that energy is conserved in the simulations.

The thermal energy component of the injected energy is significantly greater than the other components in the cluster environment for early times due to the high pressure jet hotspot. The situation is different in the poor group environment, where the thermal and kinetic components of the injected energy are similar for most of the simulation. The larger kinetic energy component in the poor group compared to the cluster for early times is likely due to the significantly larger lobe volume and mass in the poor group (see Figure 3.6) since the kinetic energy depends on the mass of entrained material.

In both environments the injected kinetic energy drops sharply when the jet is switched off ($t = 40$ Myr) since the high velocity jet material is no longer being injected into the simulation. This dramatic drop is not seen in the thermal energy component simply because it is not affected by the jet as much; the majority of the thermal energy comes from the over-pressured cocoon and hotspot.

The gravitational potential energy component is expected to be greater in the cluster environment due to the increased gas mass available; the higher average density in the cluster means there is more gas for the jet to do work against by uplifting it. This is seen in the energy plot for the cluster (Figure 3.14) where both the kinetic and thermal energy components are converted quickly to gravitational potential energy once the jet is switched off as the ambient material is uplifted, leading gravitational potential energy to dominate from approximately $t = 125$ Myr onwards. Kinetic and thermal potential energy are also converted to gravitational potential energy in the poor group environment at later times (Figure 3.15), however this conversion is not as rapid as in the cluster environment,

3.3. FEEDBACK EFFICIENCY

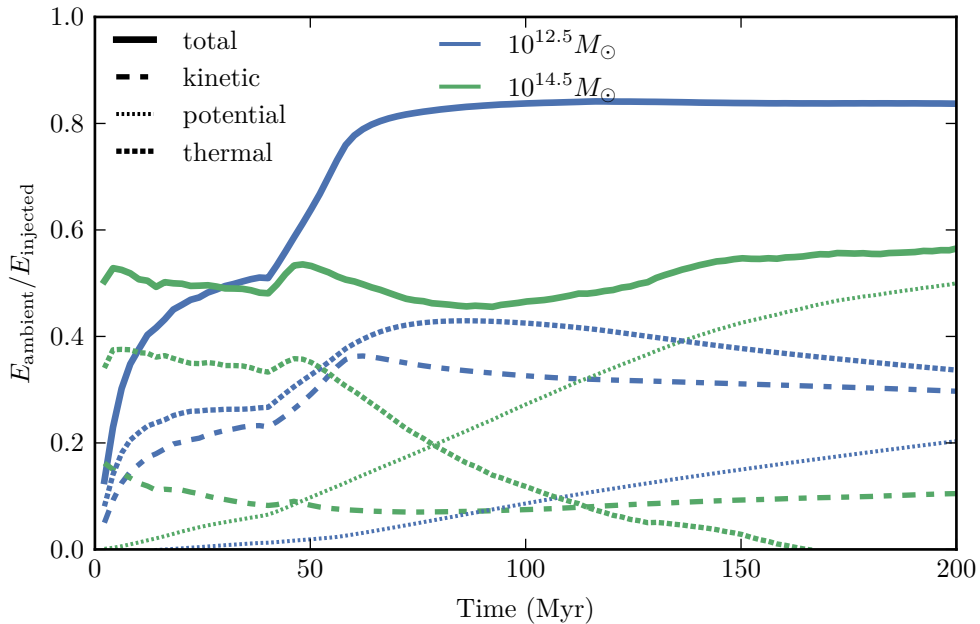


Figure 3.16: Feedback efficiency (fraction of injected energy that couples to ambient gas) as a function of simulation time for both the poor group and cluster environments, for $n = 1$, run codes **m12.5-M25-n1** and **m14.5-M25-n1**.

due to the aforementioned larger gas mass. If the simulation were evolved for longer, I predict that the gravitational potential energy would be larger than the kinetic and thermal components for the poor group environment, as in the cluster environment. This result, that a large percentage of the injected energy ends up as gravitational potential energy at later times, agrees with the simulations carried out by Vernaleo & Reynolds (2007).

3.3 Feedback Efficiency

The effect of AGN feedback on the surrounding environment is governed by the feedback efficiency: the fraction of total injected jet energy that couples to the surrounding ambient medium. An accurate prescription of AGN feedback requires knowing the feedback efficiency for the environment and jet being considered. This is useful for both semi-analytic galaxy formation models (Croton et al., 2006) and

3.3. FEEDBACK EFFICIENCY

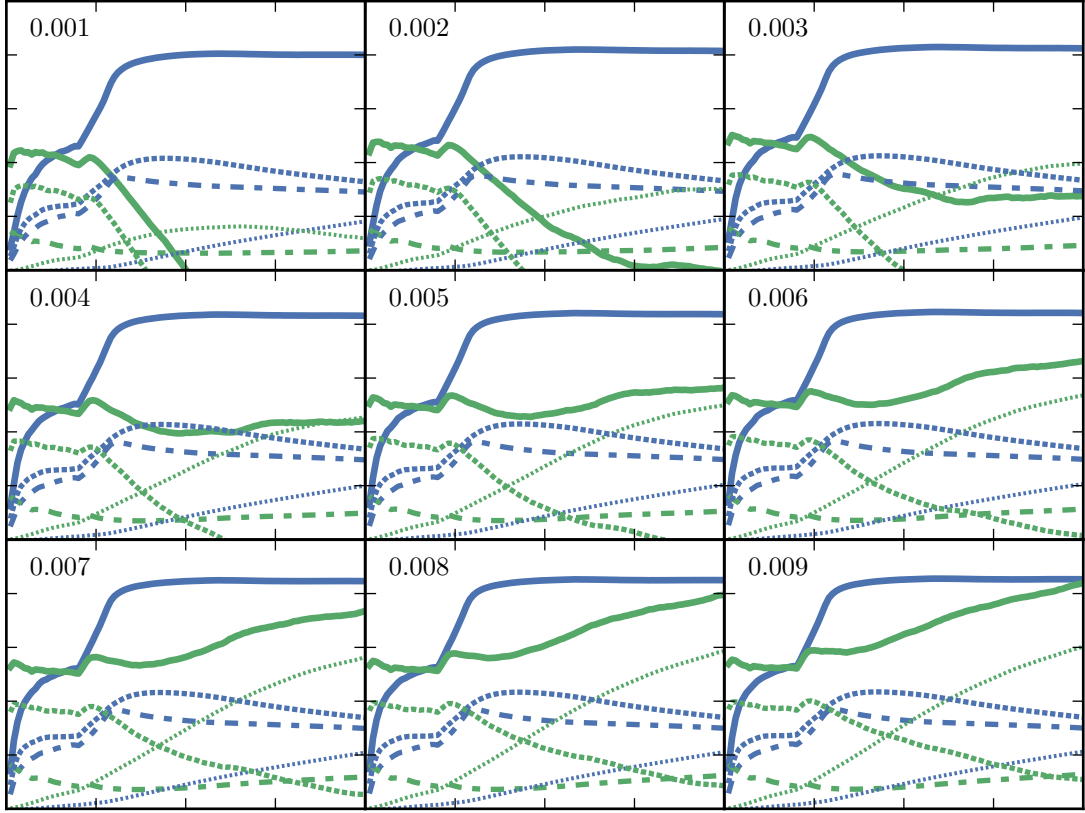


Figure 3.17: Feedback efficiency as a function of time for nine different tracer cutoff values, shown in top left of each plot. The simulation runs and line legends are the same as for Figure 3.16.

numerical hydrodynamical galaxy formation simulations (Vogelsberger et al., 2014). In this section I quantify the energy feedback for simulations in both the cluster and poor group environments.

The simulation grid is divided into ambient and jet material through the use of jet tracer particles and a tracer threshold of 0.005, as was discussed in Section 3.1. Grid cells with a tracer value below the threshold are classed as non-jet or ambient material, while cells with a tracer value greater than the threshold are classed as jet material. Using these classifications, the energy components are divided into energy in the jet material and energy in the ambient material, and the total energy for a simulation time step is calculated by summing up all the components.

3.3. FEEDBACK EFFICIENCY

The evolution of feedback efficiency over time for the $n = 1$ simulations in the cluster and poor group environments is shown in Figure 3.16; solid lines are the main focus of the plot and show the overall feedback efficiency, while other lines show the individual components. The tracer cutoff value chosen significantly affects the resulting feedback efficiency for the cluster environment, but not for the poor group environment, as shown in Figure 3.17. The feedback efficiency of the thermal energy component in the cluster environment is most affected by the chosen tracer cutoff value; the gravitational potential feedback efficiency is the next most affected and the kinetic feedback efficiency is essentially unaffected. Mixing between the cocoon and ambient medium once the jet is switched off accounts for the dependence of feedback efficiency on the tracer cutoff value shown for the cluster environment, however this does not explain why such a dependence is not shown for the poor group environment. This dependence warrants further investigation, and could be the subject of future work. A tracer cutoff value of 0.05 is used for all the simulations presented in this thesis because it is the midpoint of the tracer cutoff range; however the absolute values of the cluster environment feedback efficiencies are likely unreliable.

The jet in the cluster environment initially has a higher feedback efficiency compared with the jet in the poor group environment; however the feedback efficiency of the poor group overtakes at approximately 30 Myr, leading to a significant difference between the feedback efficiency of the two environments. A sharp increase in overall feedback efficiency due to a corresponding increase in thermal (and kinetic for the poor group environment) feedback efficiency is present for both environments when the jet switches off at 40 Myr. There is no increase in kinetic feedback efficiency for the cluster environment because most of the injected energy is in the thermal component, shown in Figure 3.14. This increase in overall feedback efficiency, which is larger in the poor group environment, is due to both the increased rate of Rayleigh-Taylor mixing between the jet cocoon and the ambient gas and the refilling of the jet channel once the jet is switched off. Figure 3.7 and Figure 3.8 shows this mixing and refilling taking place. It is larger in the poor

3.3. FEEDBACK EFFICIENCY

group environment due to a greater amount of mixing taking place; compare the $t = 60.0$ panels in Figure 3.8 and Figure 3.7.

The overall feedback efficiency in the poor group environment stabilises to 80% at later times, while for the cluster it stabilises to 50%. The largest feedback efficiency is in the gravitational potential energy for the cluster environment, which is expected due to the large average density of this environment leading to a greater amount of injected energy ending up in the gravitational potential component as discussed in Section 3.2. In contrast the kinetic and thermal feedback efficiency components for the poor group are similar once the jet is switched off, and the gravitational potential feedback efficiency is lower.

Overall, the average feedback efficiency is significantly different between the two environments. AGN feedback and its role in maintaining the heating/cooling balance depends on this; larger feedback efficiencies in the poor group environment suggest AGN feedback plays a greater role in this case, compared to AGN feedback in a cluster. Clusters of galaxies are formed through mergers, meaning that there are greater numbers of clusters at low redshift. N-body simulations such as the Millennium Simulation (Springel et al., 2005) confirm this, as shown by De Lucia & Blaizot (2007). This means that the impact of AGN feedback on galaxy evolution is larger at higher redshifts where there is a greater percentage of poor groups, and smaller at low redshifts where there are more clusters.

The simulations carried out in this thesis do not include cooling or magnetic fields. The inclusion of cooling would decrease the injected thermal energy over time, however the difference in feedback efficiency between the environments is mostly due to the gravitational potential feedback efficiency, so I do not believe this would greatly affect the results. Including magnetic fields is unlikely to impact the results since the overall jet dynamics are largely unaffected, as shown in Hardcastle & Krause (2014).

3.4 Surface Brightness

All the simulations carried out in this thesis are purely hydrodynamical and do not contain the necessary physics (primarily magnetic fields) to completely calculate the synchrotron emissivity. However, it is possible to calculate the emissivity per unit volume by assuming that the pressure in the jet lobes is related to the electron energy density, thermal energy density and magnetic field energy density. This is the basis for radio source dynamical models (e.g. those developed by Kaiser et al. (2000) and Turner & Shabala (2015)), which further typically assume that there is approximate equipartition between the particle and magnetic field energy densities.

The synchrotron emissivity per unit volume $J(\omega)$ can be written as

$$J(\omega) = A \frac{\sqrt{3\pi} e^3 B}{16\pi^2 \epsilon_0 c m_e (q+1)} \kappa \left(\frac{\omega m_e^3 c^4}{3eB} \right)^{-\frac{q-1}{2}} \quad (3.4)$$

with

$$A = \frac{\Gamma\left(\frac{q}{4} + \frac{19}{12}\right) \Gamma\left(\frac{q}{4} - \frac{1}{12}\right) \Gamma\left(\frac{q}{4} + \frac{5}{4}\right)}{\Gamma\left(\frac{q}{4} + \frac{7}{4}\right)} \quad (3.5)$$

as shown in Longair (2011, Chapter 8). Here we have assumed a power-law distribution of electron energies $N(E) = \kappa E^{-q}$ with exponent q and normalisation κ at an angular frequency ω , which relates to the observing frequency $\nu = \frac{\omega}{2\pi}$. Throughout the rest of the analysis, I take $q = 2.2$ as in Hardcastle & Krause (2013), which gives a spectral index $\alpha = \frac{1-q}{2} = -0.6$ that is typical of radio lobes.

The relationship between cocoon pressure and energy densities is given in Kaiser et al. (1997) as

$$p = (\Gamma_c - 1)(u_e + u_B + u_T) \quad (3.6)$$

where p is the pressure, u_e , u_B and u_T are the electron, magnetic field and thermal energy densities respectively, and Γ_c is the adiabatic index, taken to be $\Gamma_c = 4/3$

3.4. SURFACE BRIGHTNESS

for a relativistic plasma.

The normalisation κ can be written as

$$\kappa = \frac{u_e}{I} = \frac{u_B \eta}{I} \quad (3.7)$$

using $\eta = u_B/u_e = B^2/(u_e 2\mu_0)$, the ratio between the energy densities of the magnetic field and electrons respectively, and I is the integral of $EN(E)$

$$I = \int E \times E^{-q} dE = (m_e c^2)^{2-q} (\gamma_{\max}^{2-q} - \gamma_{\min}^{2-q}) / (2 - q) \quad (3.8)$$

Equation (3.6) can be rewritten to give u_e in terms of the cocoon pressure and departure from equipartition as

$$u_e = \frac{p}{(\Gamma_c - 1)(\eta + 1)} \quad (3.9)$$

with the assumption that there is no thermal energy.

Using Equation (3.9) and $u_B = B^2/(2\mu_0)$ one can write

$$\begin{aligned} B &= (2\mu_0 \eta u_e)^{1/2} \\ &= \left(\frac{2\mu_0}{\Gamma_c - 1} \left[\frac{\eta}{1 + \eta} \right] \right)^{1/2} \end{aligned} \quad (3.10)$$

which leads to an expression for κ in terms of the cocoon pressure

$$k = \frac{1}{\Gamma_c - 1} \left(\frac{1}{1 + \eta} \right) \frac{1}{I} p \quad (3.11)$$

Substituting Equations (3.10) and (3.11) with $\nu = \omega/2\pi$ into Equation (3.4) gives

$$J(\nu) = K(q) \left(\frac{e^3}{\epsilon_0 c m_e} \right) \left(\frac{\nu m_e^3 c^4}{e} \right)^{-\frac{q-1}{2}} (2\mu_0)^{\frac{q+1}{4}} \frac{1}{I} \left(\frac{\eta^{\frac{q+1}{4}}}{(1 + \eta)^{\frac{q+5}{4}}} \right) p^{\frac{q+5}{4}} \quad (3.12)$$

3.4. SURFACE BRIGHTNESS

$$\begin{aligned}
K(q) &= \left(\frac{A}{(\Gamma_c - 1)^{\frac{q+5}{4}}} \right) \left(\frac{2\pi}{3} \right)^{-\frac{q-1}{2}} \left(\frac{\sqrt{3\pi}}{16\pi^2(q+1)} \right) \\
&= \left[\frac{\Gamma\left(\frac{q}{4} + \frac{19}{12}\right) \Gamma\left(\frac{q}{4} - \frac{1}{12}\right) \Gamma\left(\frac{q}{4} + \frac{5}{4}\right)}{\Gamma\left(\frac{q}{4} + \frac{7}{4}\right)} \right] \frac{1}{(\Gamma_c - 1)^{\frac{q+5}{4}}} \\
&\quad \times \left(\frac{2\pi}{3} \right)^{-\frac{q-1}{2}} \left(\frac{\sqrt{3\pi}}{16\pi^2(q+1)} \right)
\end{aligned} \tag{3.13}$$

The luminosity in each simulation cell is then given by $L(\nu) = 4\pi J(\nu)V$, where V is the cell volume. The final luminosity scaled to physical units (W Hz^{-1}) is then

$$L(\nu) = L_0 \left(\frac{\nu}{1 \text{ GHz}} \right)^{-\frac{q-1}{2}} \left(\frac{p_0}{10^{-11} \text{ Pa}} \right)^{\frac{q+5}{4}} \left(\frac{L_1}{\text{kpc}} \right)^3 \tag{3.14}$$

where L_0 is the coefficient for $L(\nu)$ scaled to $(L_1, p_0, \nu) = (1 \text{ kpc}, 10^{-11} \text{ Pa}, 1 \text{ GHz})$.

The observed flux density and surface brightness can be obtained from the luminosity as

$$S = \frac{L(\nu)}{4\pi D_{\text{lumin}}^2} (1+z)^{1+\alpha} \tag{3.15}$$

and

$$S_{\text{obs}} = S \frac{1}{\xi} \tag{3.16}$$

where L is the cell luminosity, D_{lumin} is the luminosity distance, z is the redshift of the source, α is the spectral index and ξ is the number of beams per simulation cell.

Equation (3.16) is used to produce surface brightness plots for simulations as if the radio galaxies were being observed at redshift $z = 0.1$, with a $\theta_{\text{FWHM}} = 5''$ beam at $\nu = 1.4 \text{ GHz}$. The observing beam size and frequency were chosen to match those used in the FIRST survey (Becker et al., 1995). The departure from equipartition is taken to be $\eta = 0.1$, which is consistent with the observations of Croston et al.

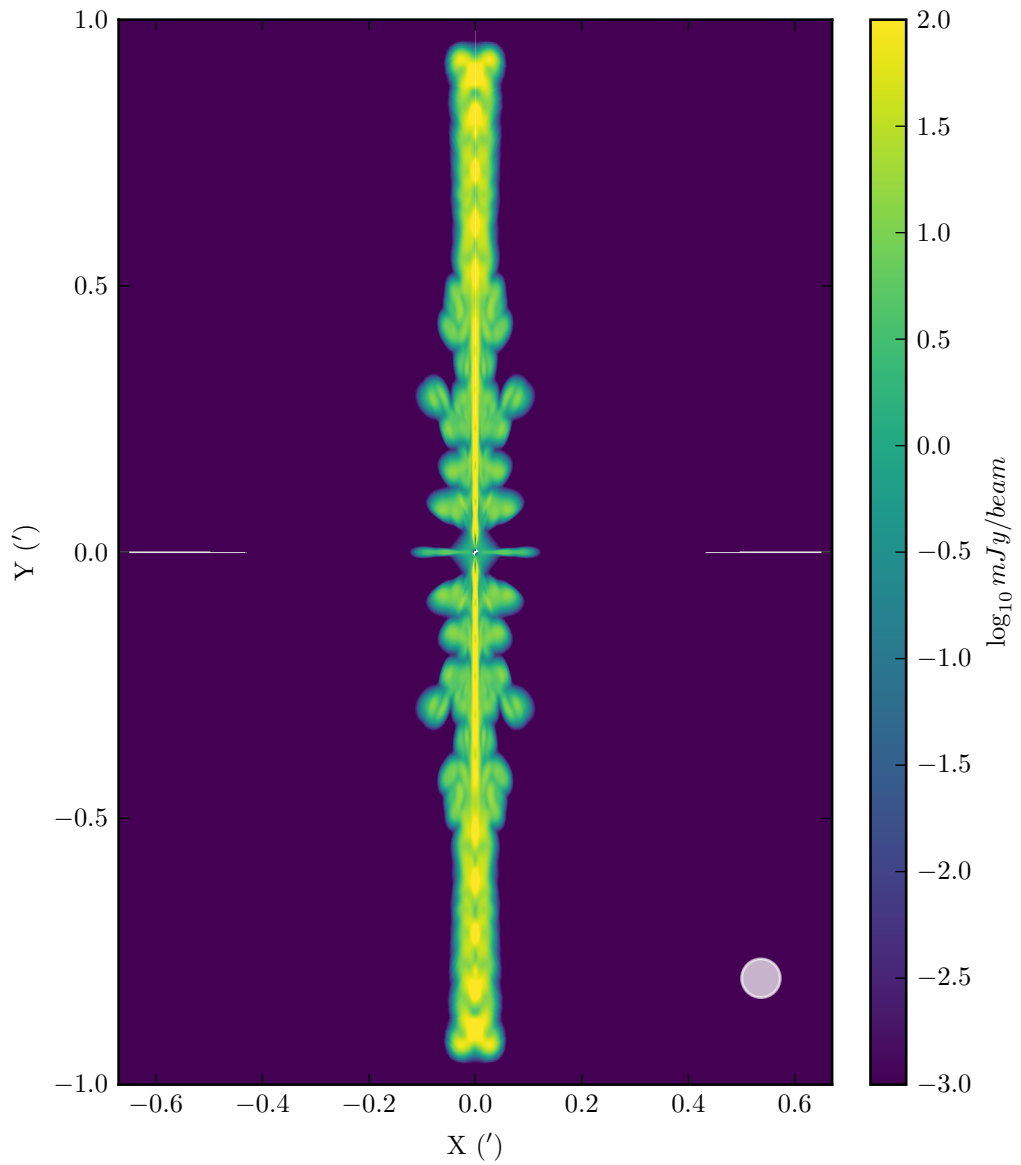


Figure 3.18: Surface brightness plot for $n = 1$ simulation in cluster environment, run **m14.5-M25-n1**, at $t = 40$ Myr. Source is placed at a redshift of $z = 0.1$, viewed with a 5 arcsec beam at 1.4 GHz.

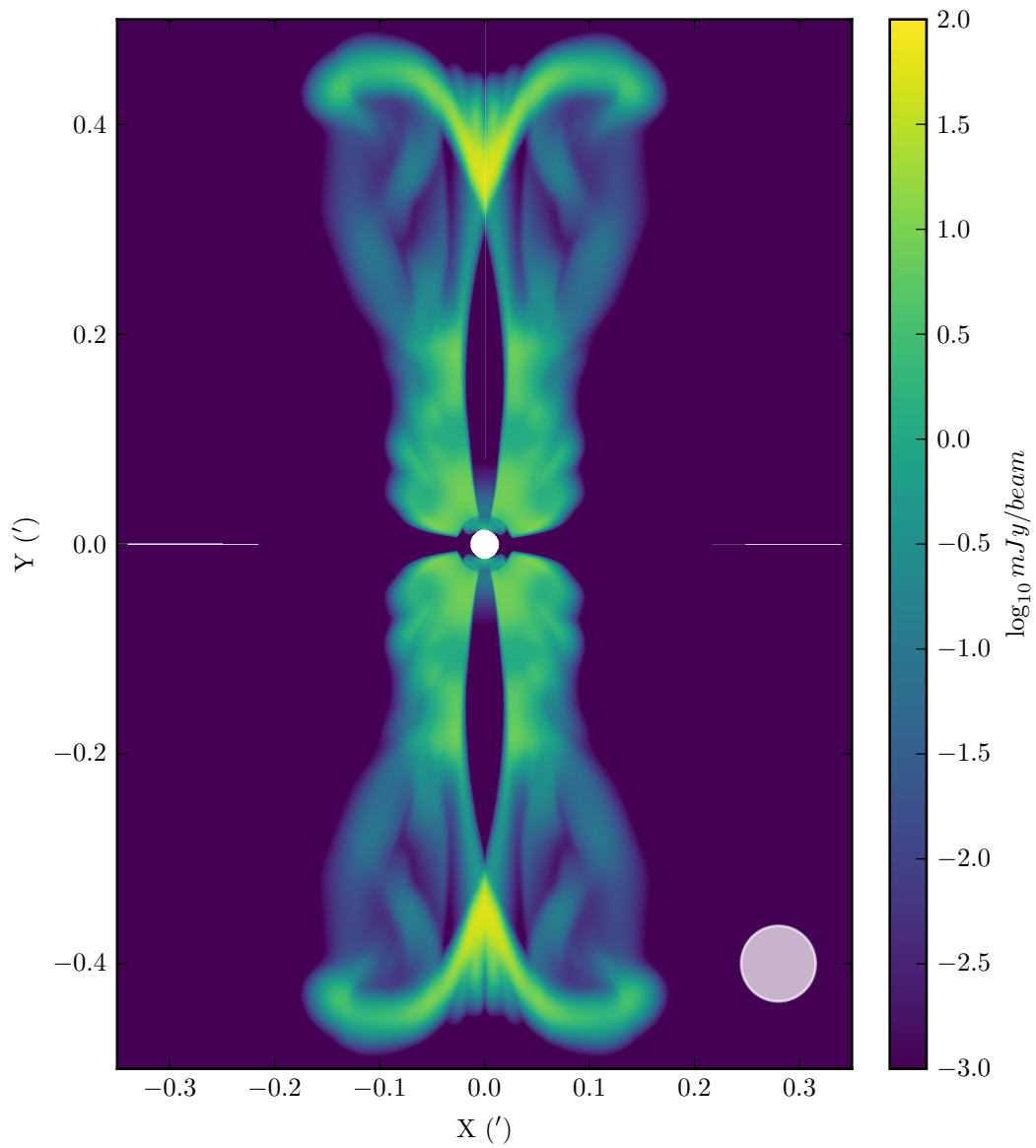


Figure 3.19: Surface brightness plot for $n = 1$ simulation in poor group environment, run **m12.5-M25-n1**, at $t = 40$ Myr. Source is placed at a redshift of $z = 0.1$, viewed with a 5 arcsec beam at 1.4 GHz.

3.4. SURFACE BRIGHTNESS

(2005). The maximum and minimum energies are taken to correspond to Lorentz factors $\gamma_{\min} = 10$ and $\gamma_{\max} = 10^5$ as in Hardcastle & Krause (2013).

The surface brightness of each grid cell is calculated using Equation (3.16), and is then weighted by the average value of the jet tracer convolved with a 2-dimensional boxcar kernel of width 3. This weighting process is necessary because each simulation cell may in principle contain both jet and non-jet material. Weighting by the jet tracer value corresponds to only the jet plasma contributing to synchrotron emission. Finally the tracer weighted flux density is convolved with the $\theta_{\text{FWHM}} = 5''$ observing beam. Figure 3.18 shows the surface brightness plot of the radio jet for $n = 1$ in the cluster environment when the jet switches off at $t = 40$ Myr, while Figure 3.19 shows the corresponding simulation for the poor group environment. Note that in both these figures the quarter-plane jet has been reflected in both the horizontal and vertical planes, with the assumption that the jet is axisymmetric. The convolving beam size is shown in both figures as the circle in the lower right.

There are two simulation artefacts present in the surface brightness distributions. First is the injection radius and inner radial high-resolution grid patch, most visible for the poor group environment but visible in the cluster environment as well. The apparent discontinuity in surface brightness transitioning from the high-resolution to regular grid is an artefact of smoothing the jet tracer with a boxcar kernel. The second simulation artefact, which is only present for the cluster environment, is the extension of thin “fingers” of synchrotron emitting material from the centre, perpendicular to the direction of jet propagation. The reflective boundary condition imposed on the $\theta = \pi/2$ boundary is the cause for these extensions, and they would not occur if the entire plane was simulated along with a counter-jet.

There is a large difference in the observed surface brightness maps, due to the differing lobe morphology in the two environments. The general jet morphology discussed in Section 3.1 is visible in the surface brightness maps for both environments. The recollimation of the jet is visible for both environments, and is more prominent with the jet in the poor group environment because of the larger recollimation length scale L_{1a} . In addition to the recollimation, diamond shocks are

3.5. SIZE-LUMINOSITY DIAGRAM

visible along the latter half of the jet in the cluster; these are due to the reflection and propagation of the initial recollimation down the jet length (Norman et al., 1982). So called because of their diamond shape, these shocks are observed as knots in astrophysical jets, see e.g. Nawaz et al. (2014). Multiple diamond shocks are not present for the jet in the poor group environment due to the large length scale of recollimation; however the narrowing of the jet beam seen near the hotspot would likely form a diamond shock if the jet were active for longer.

The hotspot shows as a region of high surface brightness at the head of the jet for both environments, which is expected due to the high pressure in this area. The jet shock is also visible for the jet in the poor group environment; but it is not clearly defined for the jet in the cluster environment. Backflow of material from the hotspot into the radio lobe is visible in the surface brightness map for the jet in both environments, along with the radio lobe itself. Mixing between the radio lobe and the ambient medium is visible for the cluster environment, but not for the poor group environment. Kelvin-Helmholtz vortices are slightly visible for the simulation in the cluster environment; they are however largely smoothed out due to convolving the surface brightness with the observing beam.

Finally, the jet in the cluster has a higher overall surface brightness compared with the jet in the poor group, due to the higher pressure. 1 mJy/beam is roughly the source detection limit for FIRST (Becker et al., 1995), so a large part of the radio lobe for the poor group would not be detected. Parts of the radio lobe inflated by the jet in the cluster environment would also fall below the detection limit if the source were moved out to higher redshift. At low redshifts it is likely that a radio source in a poor group would be undetected with a FIRST-like survey, and at higher redshifts the same would be true for a radio source in a cluster.

3.5 Size-Luminosity Diagram

The evolution of total source luminosity with source size is known as a P-D track, and was first introduced by Shklovskii (1963) as a tool for studying the temporal

3.5. SIZE-LUMINOSITY DIAGRAM

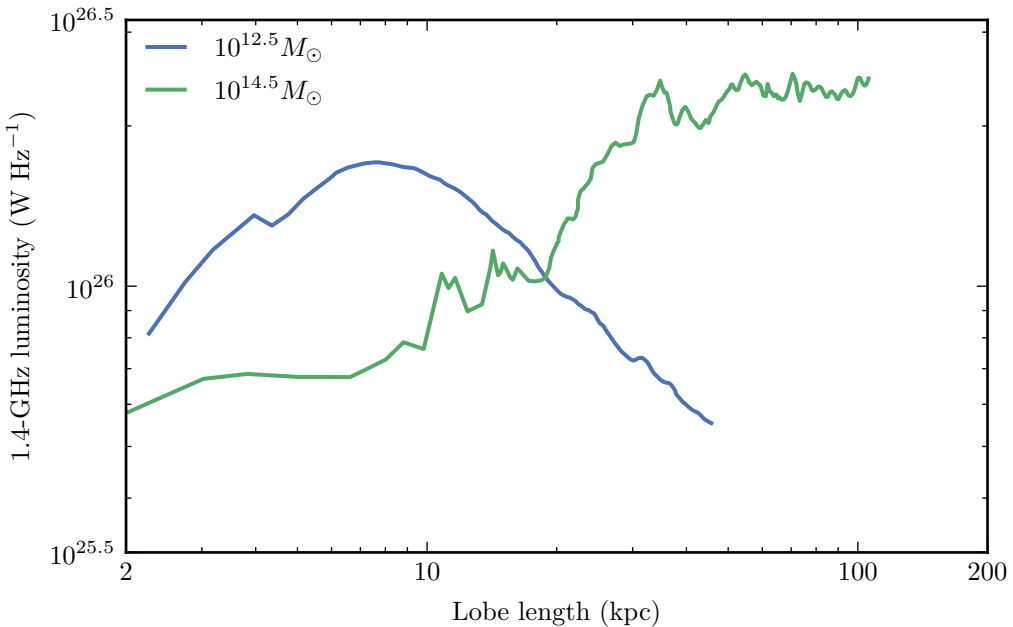


Figure 3.20: Size-luminosity diagram for the $n = 1$ jet in both the poor group and cluster environment, run codes **m12.5-M25-n1** and **m14.5-M25-n1**.

evolution of radio sources. The position of a radio source on the P-D diagram can give information about the power of the jet and its active time. Kaiser et al. (1997) developed a model for the evolution of a radio source through the P-D diagram, and showed that the shape of the track depends on the environment. Larger central densities should correspond to higher P-D tracks. The rate at which the density profile falls off also has an effect: a flat density profile corresponds to a rising P-D track, while a steep density profile corresponds to a falling P-D track. With this in mind, a jet in a poor group with the gas density set by the hydrostatic equilibrium density profile is expected to produce a rising P-D track initially while it is in the flat density regime, before falling off as the density profile begins to decline. On the other hand, a jet in a cluster is expected to continue rising for larger radii, due to the density profile remaining flat for longer.

The total luminosity of the simulation is calculated by adding up the luminosity in each grid cell as given by Equation (3.14). The total luminosity is plotted against the lobe size in Figure 3.20 for the $n = 1$ simulation in the cluster and

3.6. THE KING GAS DENSITY PROFILE

poor group environments. Lobe size acts as a proxy for time (see Figure 3.5), so the x-axis in Figure 3.20 is effectively time. The track of the jet in the poor group environment reproduces the peak of the evolutionary track and subsequent decline in overall luminosity at large jet sizes of the standard model developed by Kaiser et al. (1997). The track of the jet in the cluster environment continues to increase with increasing jet size due to the gas density profile in the cluster, as is expected due to the larger region of approximately constant density. The jet is still expanding into a significantly denser environment at large radii compared to the poor group, which increases the pressure and in turn increases the overall luminosity.

The overall evolution of the luminosity over the jet active time seen in the simulations is very large, close to 1 dex. This means that observations of radio sources and the determination of their properties is dependent on the stage of evolution the source is in. In addition, knowing the environment into which the jet is propagating is important for interpreting jet properties. Simulations allow the P-D diagram to be fully explored for a range of jet powers and environments which can provide a framework to link observations to the underlying jet properties.

3.6 The King Gas Density Profile

The effect of different gas density profiles on jet structure is important for simulations; in this section I compare two different gas density profiles, one obtained through hydrostatic equilibrium with a dark matter halo, and the other empirically through observations. In Section 2.6, I described the isothermal β or King profile, an empirical gas density profile derived from observations, which is used in many radio jet simulations (e.g. English et al. (2016); Hardcastle & Krause (2013, 2014); Vernaleo & Reynolds (2007)). This profile differs from the Makino hydrostatic equilibrium profile in both the central density and overall shape, as shown in Figure 2.5. The Makino profile has large differences in density between the cluster and poor group environments, and so results in significantly different

3.6. THE KING GAS DENSITY PROFILE

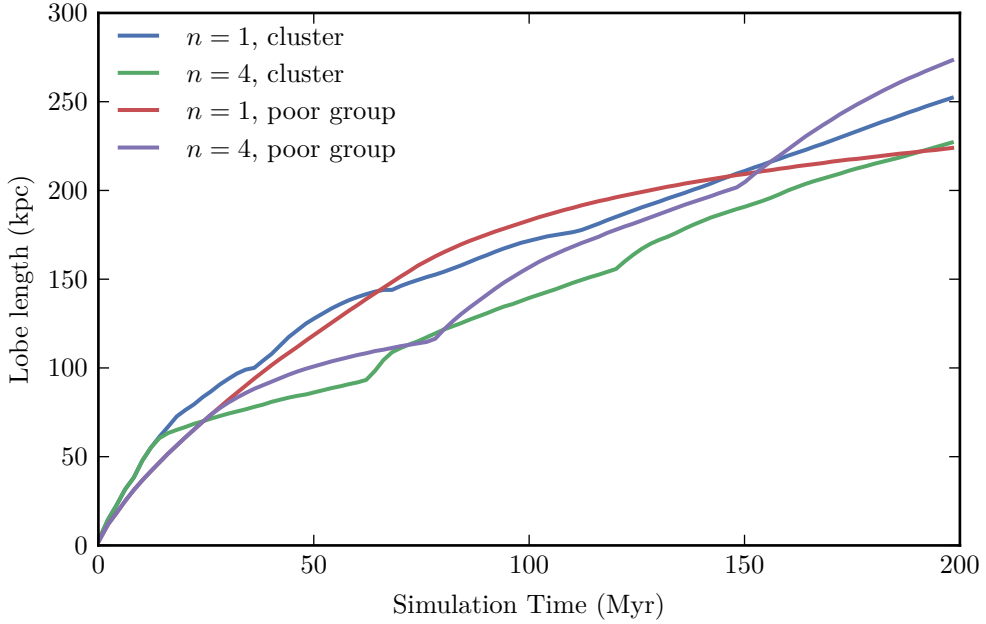


Figure 3.21: Lobe length as a function of simulation time for the $n = 1$ and $n = 4$ outburst jets in the King cluster and poor group environments, run codes **m12.5-M25-n1-king**, **m12.5-M25-n4-king**, **m14.5-M25-n1-king**, **m14.5-M25-n4-king**.

jet morphologies. Compared with the Makino profile, the King profile has a lower central density, shallower falloff at large radii, and the gas density profile for the cluster environment is similar to that of the poor group environment. Using the King profile, the jet in the cluster environment is expected to produce similar morphologies to those of the jet in the poor group environment.

This is supported by the evolution of lobe length over time for the $n = 1$ and $n = 4$ outburst jets in the King cluster and poor group environments, as shown in Figure 3.21. The jets in both environments have similar lobe lengths at all times; this was not the case for the Makino gas density profile. In Figures 3.22 and 3.23 the evolution of the jet structure is shown over time with density maps for the King cluster and poor group environments respectively. These density maps can be compared to the corresponding ones for the jet in the Makino cluster and poor group environments, Figures 3.7 and 3.8 respectively. In both the King environments,

3.6. THE KING GAS DENSITY PROFILE

the jet reproduces the expected FR II morphology described in Section 3.1, such as the bow shock, working surface/hotspot, and contact discontinuity.

By comparing the evolution of the jet over time, it is clear that the two jets in the poor group environment have a similar morphology, regardless of the gas density profile used. The same is true for the two jets in the cluster environment. There are differences, however, between the resulting morphology for the two gas density profiles. The bow shock of both jets in the King environments expands quicker than the corresponding jets in the Makino environments. This is due to the lower central density in the King environment.

The recollimation length scales are significantly larger for the King gas density profile compared with the corresponding Makino ones: $L_{1a} = 16.1$ kpc for the King cluster environment, while $L_{1a} = 161$ kpc for the King poor group environment. Looking at the density map for the $n = 1$ jet in the King cluster environment (Figure 3.22, it appears to collimate around $Y = 10$ kpc, which is in agreement with the recollimation length scale. This agreement does not exist for the $n = 1$ jet in the King poor group environment (Figure 3.23); it appears to be collimating at around $Y = 50$ kpc, roughly a factor of three less than the predicted recollimation length scale. In addition, the cocoon inflated by the jet in the cluster environment undergoes more pronounced mixing with the ambient medium in the King environment compared with the jet in the Makino environment. This is because the cocoon inflated in the King cluster environment is wider than corresponding cocoon in the Makino environment, due to the aforementioned recollimation scales.

Finally, an odd feature of the $n = 1$ jet simulation in the King poor group environment is found for the $t = 60.0$ panel in Figure 3.23. There is an underdense wedge from $Y = 55$ kpc to $Y = 100$ kpc. Further research is needed to determine whether this is a numerical artefact, or a realistic effect caused by e.g. the refilling of the jet channel once the jet is switched off.

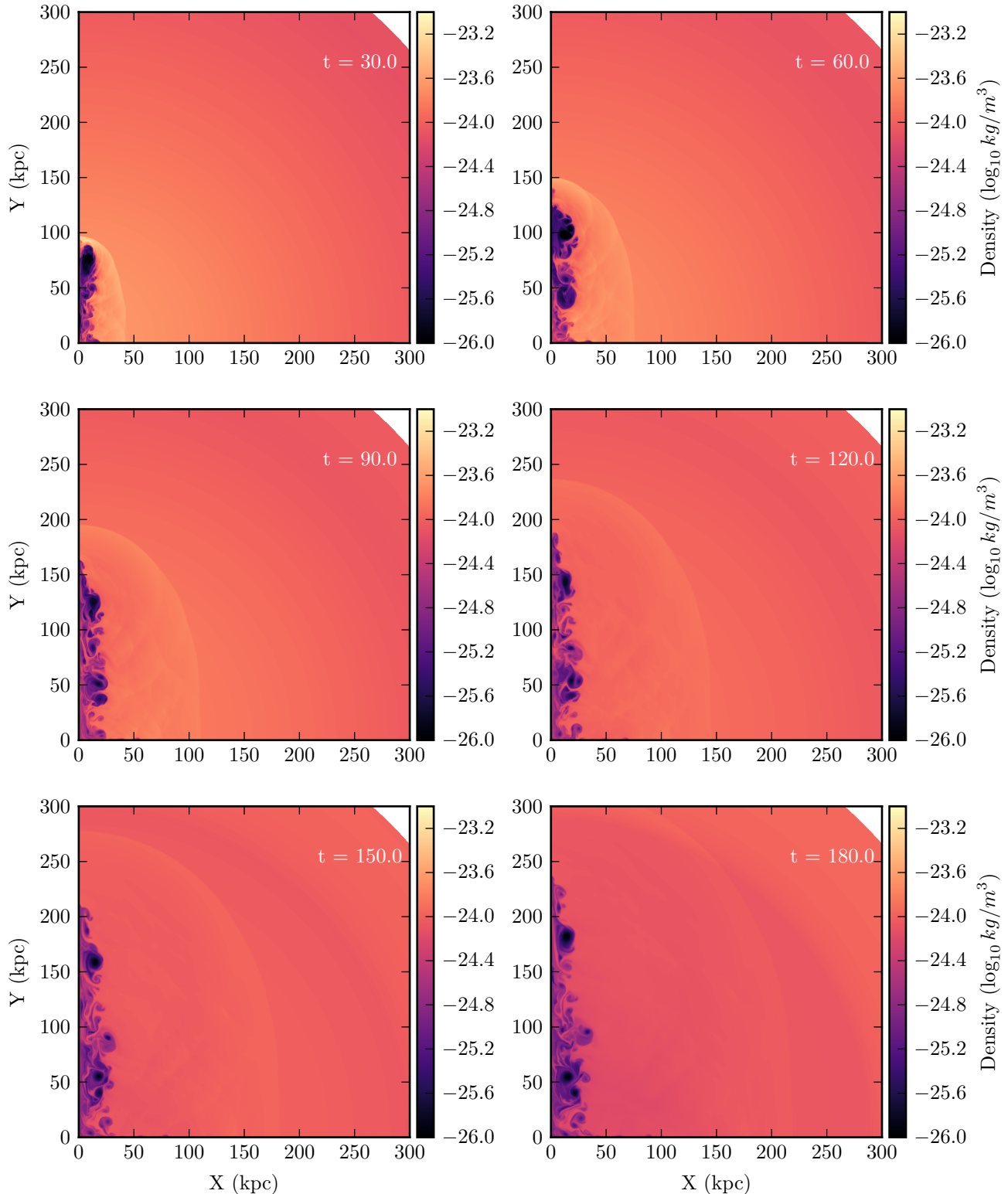


Figure 3.22: Density maps for 6 different simulation times, $t = 30, 60, 90, 120, 150$ and 180 Myr for $n = 1$ in the King cluster environment, run code **m14.5-M25-n1-king**. The jet is switched on from $t = 0$ to $t = 40$ Myr.

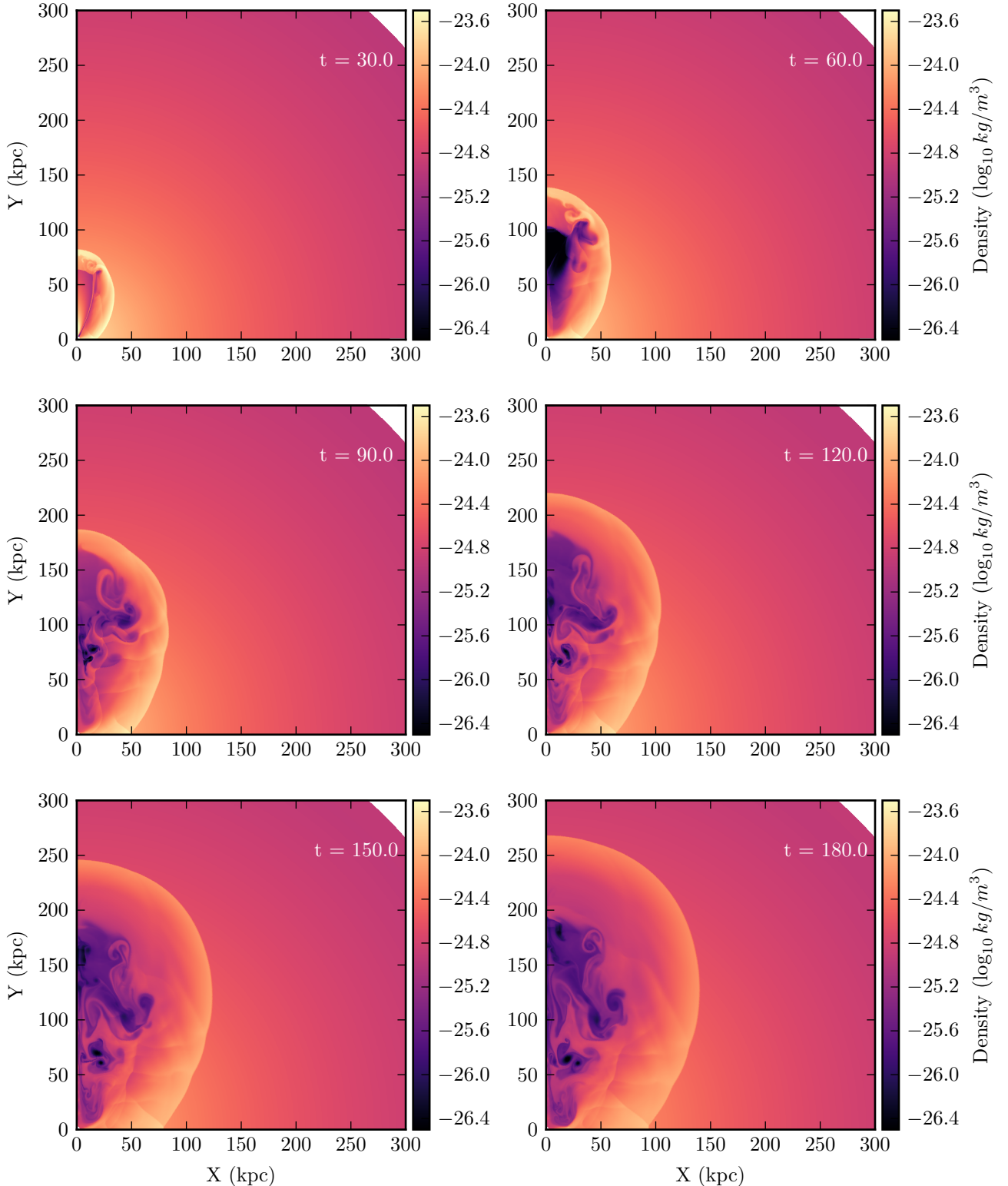


Figure 3.23: Density maps for 6 different simulation times, $t = 30, 60, 90, 120, 150$ and 180 Myr for $n = 1$ in the King profile poor group environment, run code **m12.5-M25-n1-king**. The jet is switched on from $t = 0$ to $t = 40$ Myr.

3.7 Summary

In this chapter I examined how much different environments affect the simulations. Two types of environments were looked at, the cluster environment and the poor group environment. The evolution of the jet was remarkably different in each environment, however the basic FR II morphology was reproduced in both. The difference in resulting morphology for different gas density profiles was also determined by comparing simulations of jets in environments using the King gas density profile to those using the Makino gas density profile. There were slight morphological differences between jets produced in the different gas density profiles, however the overall morphology of those in the King environment matched the corresponding simulations in the Makino environment. The remaining analysis uses simulations with the environment set by the Makino gas density profile.

The basic impact that environment has on observations is due to the jet morphology. Wider jets are produced in a poor group environment, while narrower ones are produced in a cluster. These morphology differences are visible in the observed surface brightness map of the radio source. Furthermore, radio jets in richer environments (like the cluster environment) have higher overall surface brightness; this means that for a given detection limit and a radio source at a specific redshift, jets in a cluster environment are more likely to be above the surface brightness detection limit compared to jets in a poor group environment. P-D tracks are also affected by different environments. A radio jet in a cluster environment traces a significantly different track on the P-D diagram compared with a radio jet in a poor group environment. This is due in part to the different central densities and radii at which the density profile begins to decline. Simulations of P-D tracks can be used to link observations of radio sources to the jet power and environment properties; however care must be taken to account for the current evolutionary stage of the source, since the total luminosity varies dramatically over the lifetime of the jet.

The energetics of the jet are also affected by the environment into which it is

3.7. SUMMARY

propagating. Energy injected by the jet has a greater effect on the ambient gas for a poor group environment, compared to the cluster environment, due to the higher feedback efficiency. More gas is uplifted by the jet in the cluster environment however, which is likely to contribute the most towards increasing the energy of the environment if cooling were taken into account. The feedback efficiencies calculated can be used in galaxy formation models in order to produce more realistic galaxies.

CHAPTER 4

Intermittent Radio Jets

I detailed why intermittent jet activity is required in order to maintain the heating/cooling balance of active galactic nuclei and their host galaxies in Chapter 1 (Section 1.2.4). Intermittent jets are supported through observational evidence of Double-Double radio galaxies, which are radio structures with two sets of radio lobes aligned with an inner core. The duty cycle of an intermittent jet is defined as $t_{\text{on},\text{total}}/t_{\text{total}}$. This can be constrained by observations using methods like those I reviewed in Section 2.8; however the same duty cycle can be produced by a jet with four short outbursts or one long outburst over the same time interval. How does the number of outbursts affect the resulting jet structure and energetics?

In this chapter I compare simulations of intermittent jets with the same duty cycle (20%), but different numbers of outbursts. Specifically I compare simulations in both the cluster and poor group environments, with multiple outbursts of $n = 1$, $n = 2$, $n = 3$ and $n = 4$ outbursts respectively. Except for the number of jet outbursts, the simulations are identical to the single outburst ($n = 1$) case studied in Chapter 3. This means that the total injected energy for each simulation is the same because $t_{\text{on},\text{total}} = 40 \text{ Myr}$. Despite this, the number of jet outbursts is expected to affect many of the simulation aspects examined in Chapter 3.

I begin by highlighting morphological differences caused by the number of outbursts in Section 4.1. The representative cases of outburst number compared are $n = 1$ and $n = 4$, while $n = 2$ and $n = 3$ are generally intermediate cases between the two

4.1. MORPHOLOGY

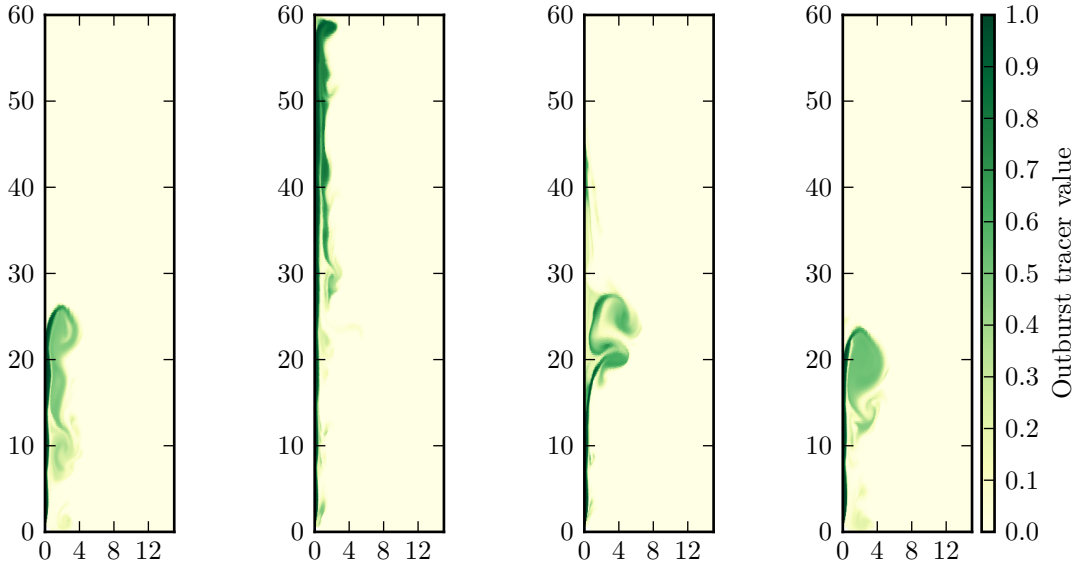


Figure 4.1: Outburst tracer map for the $n = 4$ jet in the cluster environment, run **m14.5-M25-n4**. Each panel shows the simulation as an outburst is finishing. The times from left to right are 10 Myr, 60 Myr, 110 Myr, and 160 Myr. The axes are in kpc.

extremes; the time evolution and energetics for the $n = 2$ and $n = 3$ simulations are shown in Appendix B. In Section 4.2, I examine the effects of outburst number on the energetics of the simulation, and in Section 4.3, present how the feedback efficiency also changes. Finally, I produce mock radio images and P-D tracks for simulations with different outburst numbers in Section 4.4 and Section 4.5 respectively, to show the implications of jet outburst number on observational signatures.

4.1 Morphology

The basic Fanaroff-Riley type II morphology discussed in Section 3.1 (such as the collimated jet, jet shock, hotspot, and bow shock) is reproduced for the $n = 4$ outburst jet in both environments; however there are clear differences between the $n = 1$ and $n = 4$ jets. Later jet outbursts are expected to be affected by earlier ones due to the preconditioning of the environment into which the jet is propagating.

4.1. MORPHOLOGY

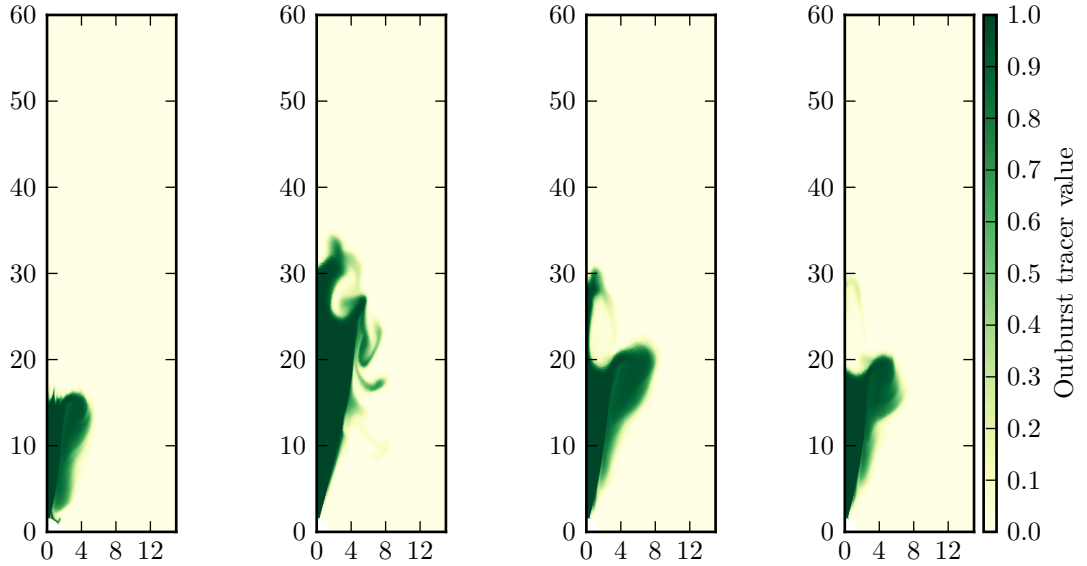


Figure 4.2: Outburst tracer map for the $n = 4$ jet in the poor group environment, run **m12.5-M25-n4**. Each panel shows the simulation as an outburst is finishing. The times from left to right are 10 Myr, 60 Myr, 110 Myr, and 160 Myr. The axes are in kpc.

This can be seen by looking at the tracer maps for each outburst. Each outburst is tagged with a corresponding tracer particle, as discussed in Section 2.5. The jet material is injected with a tracer value of 1.0, which then decreases due to mixing with the environment. Figure 4.1 shows a map of each outburst’s tracer at the time the jet is switching off for that outburst, for the $n = 4$ simulation in the cluster environment. The leftmost panel shows the tracer of the first outburst at time $t = 10$ Myr, while the rightmost panel shows the tracer of the fourth outburst at time $t = 160$ Myr.

The initial outburst evacuates a jet channel and material surrounding the core; this evacuation does not occur to the same degree for later outbursts. Refilling of the jet channel and material surrounding the core occurs once the jet is switched off as was predicted by Kaiser et al. (2000) from observations of double-double radio galaxies, with a filling timescale of ~ 10 Myr. The second outburst travels further than the other outbursts in the same amount of time. The jet of the second outburst is propagating into this partially refilled jet channel and the fact that it

4.1. MORPHOLOGY

propagates further than the other outbursts for the same time confirms that the jet finds it easier to propagate through a partially refilled channel. This behaviour is not seen for the third or fourth outbursts. By the time the third outburst begins the jet channel has almost completely refilled and so the jet propagates in a manner similar to the initial outburst.

The gradual refilling of the jet channel is evident in the outburst tracer map for the $n = 4$ simulation in the poor group, shown in Figure 4.2; the time in each panel is the same as in Figure 4.1. As with the jet in the cluster environment, the second jet outburst in the poor group environment travels further for the same amount of time (panel 2, Figure 4.2). This is again due to the partially refilled jet channel through which the jet is propagating. In addition to causing the second outburst to propagate further, the predisturbed environment from the initial outburst means that the jet in the second outburst collimates at a larger radius from the centre. Outburst four behaves more like the initial outburst, as the jet channel is almost completely refilled by this point; it still collimates at a larger radius from the centre; however this is only a few kpc later than the initial outburst. That leaves the third outburst, shown in panel 3. This outburst appears to be the case in-between outburst two and outburst four, collimating at a larger radius than outburst four, but at a smaller radius than outburst two.

The evolution of the radio lobe length as a function of simulation time for different numbers of outbursts is shown in Figures 4.3 and 4.4 for the jet in the cluster and poor group environments respectively, where the lobe length is calculated using the method described in Section 3.1. The time evolution for the $n = 4$ jet in the cluster environment is shown with the density and pressure maps in Figures 4.6 and 4.8 respectively, and for the poor group environment in Figures 4.7 and 4.9 respectively. Each outburst produces a corresponding bow shock, and these are visible in both environments. The later bow shocks overtake the previous ones in the axial direction for both environments, as well as overtaking in the transverse direction for the poor group environment. The restarted jet catches up with the previous outbursts due to the partially refilled jet channel, which makes it easier

4.1. MORPHOLOGY

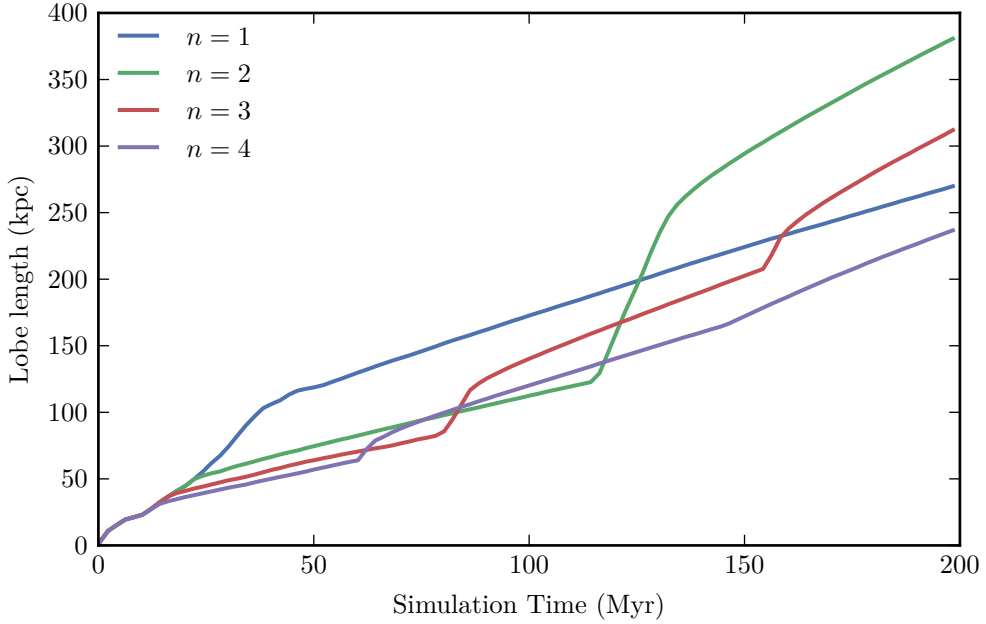


Figure 4.3: Jet lobe length as a function of simulation time for $n = 1$, $n = 2$, $n = 3$, $n = 4$ jet outbursts in the cluster environment, run codes **m14.5-M25-n1**, **m14.5-M25-n2**, **m14.5-M25-n3**, and **m14.5-M25-n4**.

for the jet to propagate.

The $n = 2$ and $n = 3$ simulations in the cluster environment produce larger lobe lengths at later times than the $n = 1$ and $n = 4$ simulations. This is not realistic, and is caused by having insufficient resolution across the jet head and working surface at large radii; this can be seen in Figure 4.5, which shows an $r - \theta$ density map comparison for the $n = 2$ standard and high resolution simulations in the cluster, runs **m14.5-M25-n2** and **m14.5-M25-n2-high-res**. The top panel is the standard run, while the lower panel is the high resolution run, with double the resolution in the θ direction. From the $r - \theta$ plot it is clear that the standard run begins to resemble the low resolution examples shown in Figure 3.11, and fails to capture the instabilities properly. The lack of instabilities leads to the jet propagating further as discussed in Section 3.1.5, and a similar result is found for the $n = 3$ jet in the cluster environment. This behaviour is not observed for the $n = 1$ and $n = 4$ jets in the cluster because the current outburst does not reach a

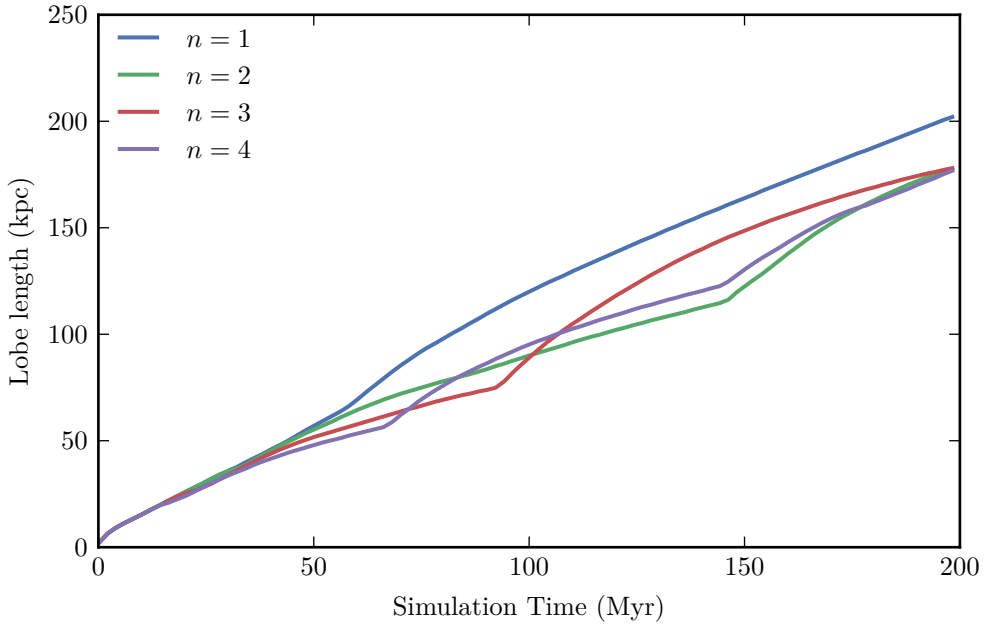


Figure 4.4: Jet lobe length as a function of simulation time for $n = 1$, $n = 2$, $n = 3$, $n = 4$ jet outbursts in the poor group environment, run codes **m12.5-M25-n1**, **m12.5-M25-n2**, **m12.5-M25-n3**, and **m12.5-M25-n4**.

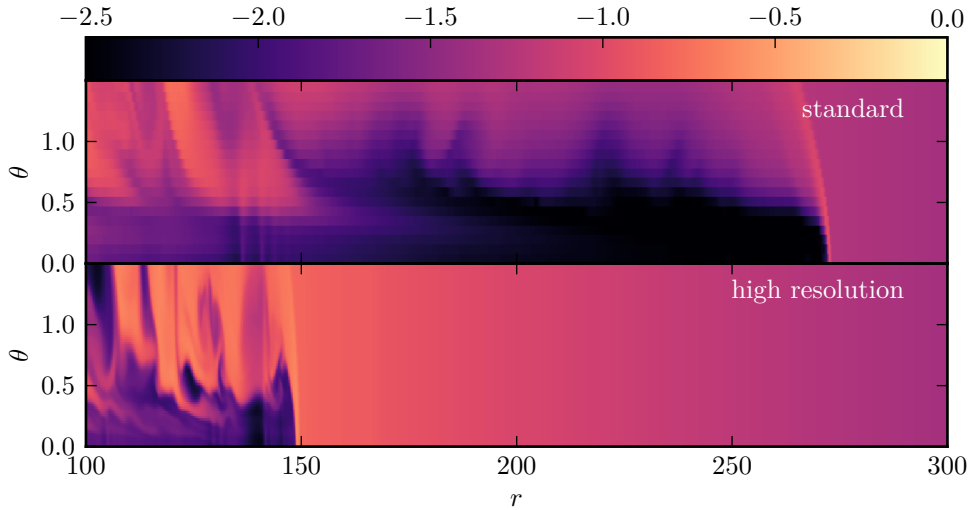


Figure 4.5: $r - \theta$ density map for the $n = 2$ simulation in the cluster environment, both standard and high resolution runs (**m14.5-M25-n2** and **m14.5-M25-n2-high-res**), at $t = 140$ Myr, $t = 20$ Myr after the second jet outburst has finished. The high resolution run has double the resolution in the θ direction. The θ axis is in degrees, the r axis in simulation length units. The colour map units are \log_{10} simulation density.

4.1. MORPHOLOGY

large enough radius during the active time for resolution to become an issue.

The length of the radio lobe in the poor group environment is bounded by the $n = 1$ simulation at later times. This implies that multiple outbursts in the poor group environment are less effective at expanding the radio source than a single outburst of the same duration. This is likely because of the larger collimated width for later outbursts shown in Figure 4.2 creating a larger working surface and decreasing the efficiency with which the jet travels through the environment. A similar situation is seen when comparing the $n = 1$ and $n = 4$ simulations in the cluster environment; again multiple outbursts are less effective at expanding the radio source than a single outburst of the same duration.

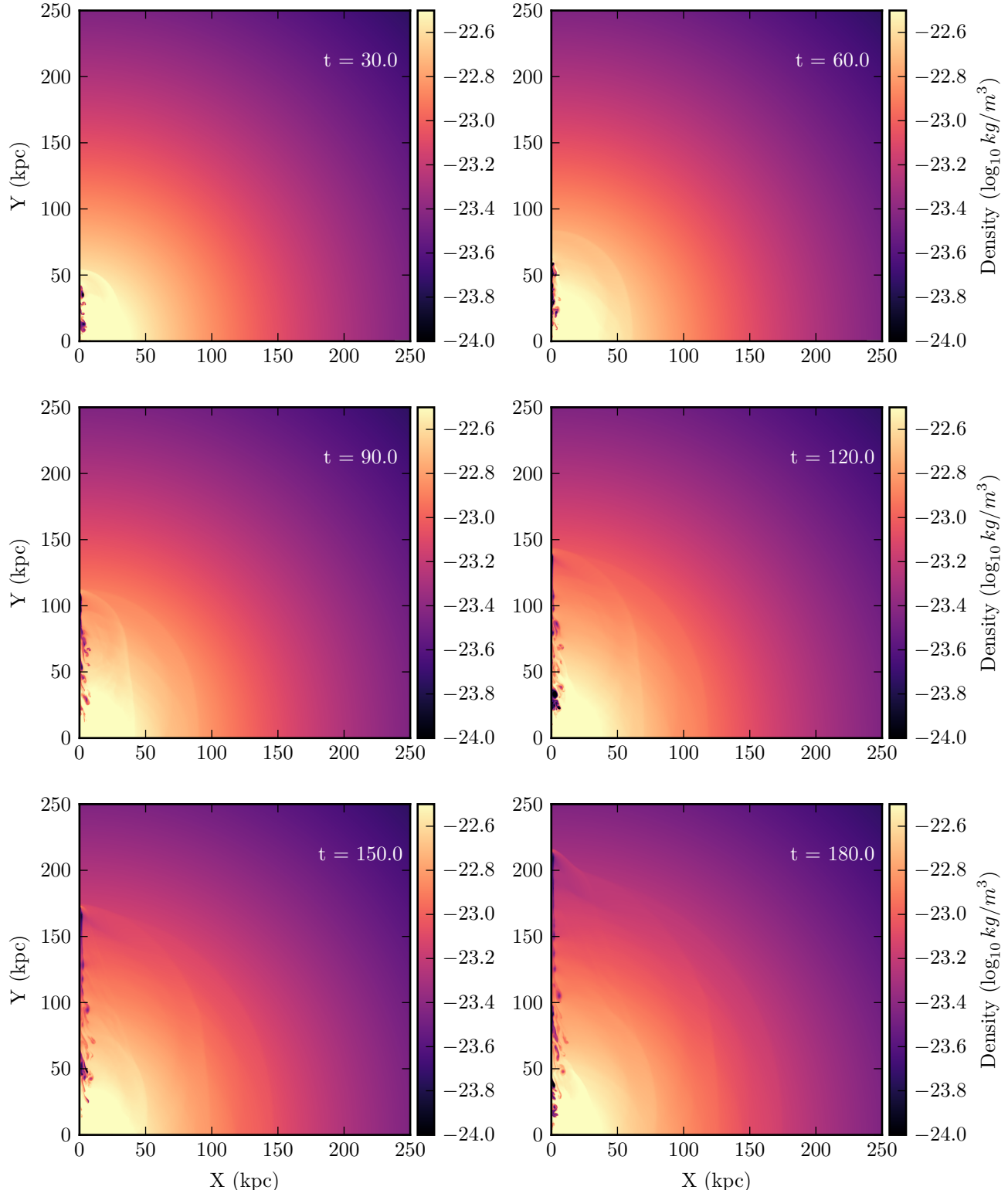


Figure 4.6: Density maps for 6 different simulation times, $t = 30, 60, 90, 120, 150$ and 180 Myr for $n = 4$ in a cluster environment, run code **m14.5-M25-n4**. The jet is switched on for: $t = 0 - 10$ Myr; $t = 50 - 60$ Myr; $t = 100 - 110$ Myr; and $t = 150 - 160$ Myr.

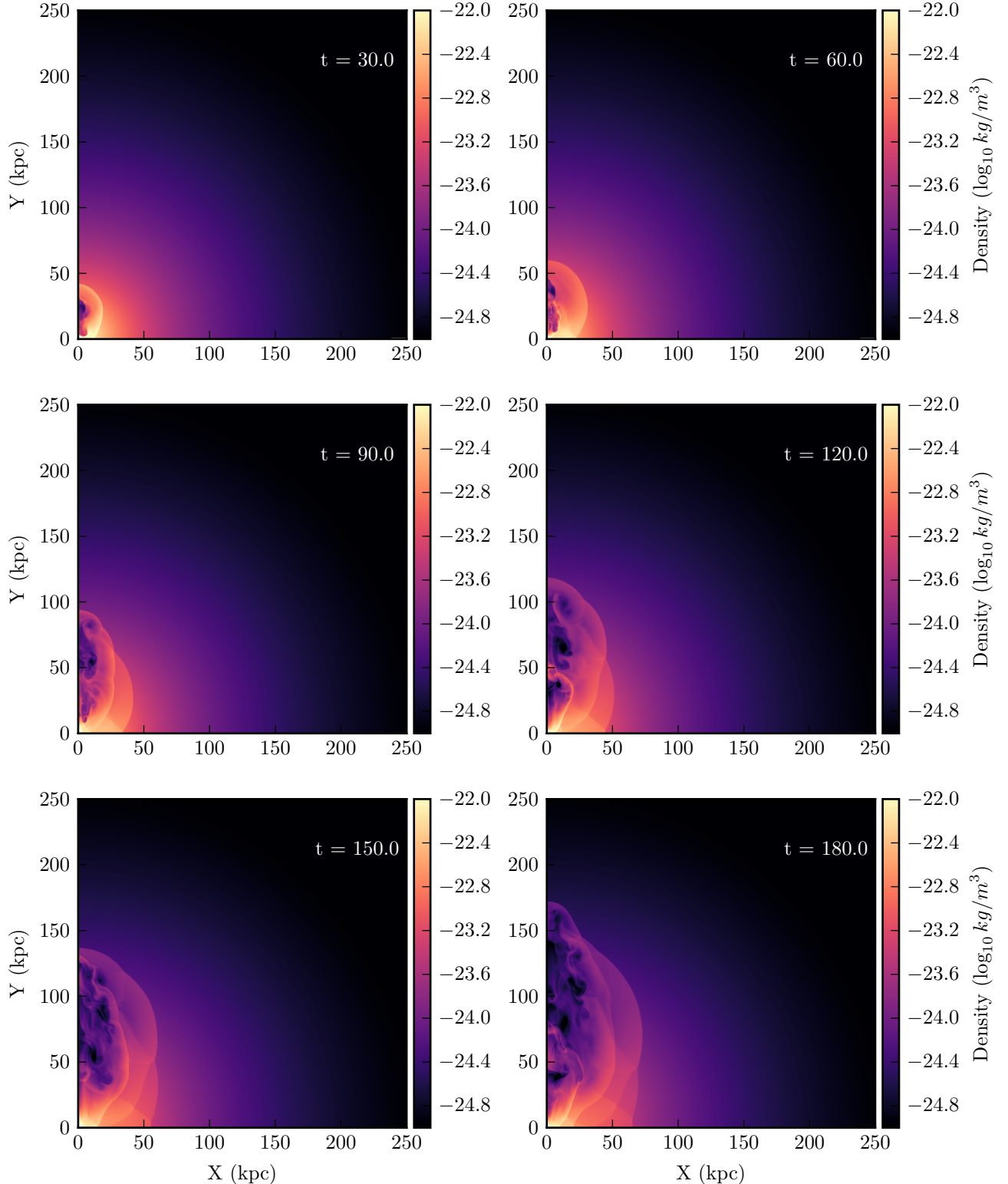


Figure 4.7: Density maps for 6 different simulation times, $t = 30, 60, 90, 120, 150$ and 180 Myr for $n = 4$ in a poor group environment, run code **m12.5-M25-n4**. The jet is switched on for: $t = 0 - 10 \text{ Myr}$; $t = 50 - 60 \text{ Myr}$; $t = 100 - 110 \text{ Myr}$; and $t = 150 - 160 \text{ Myr}$.

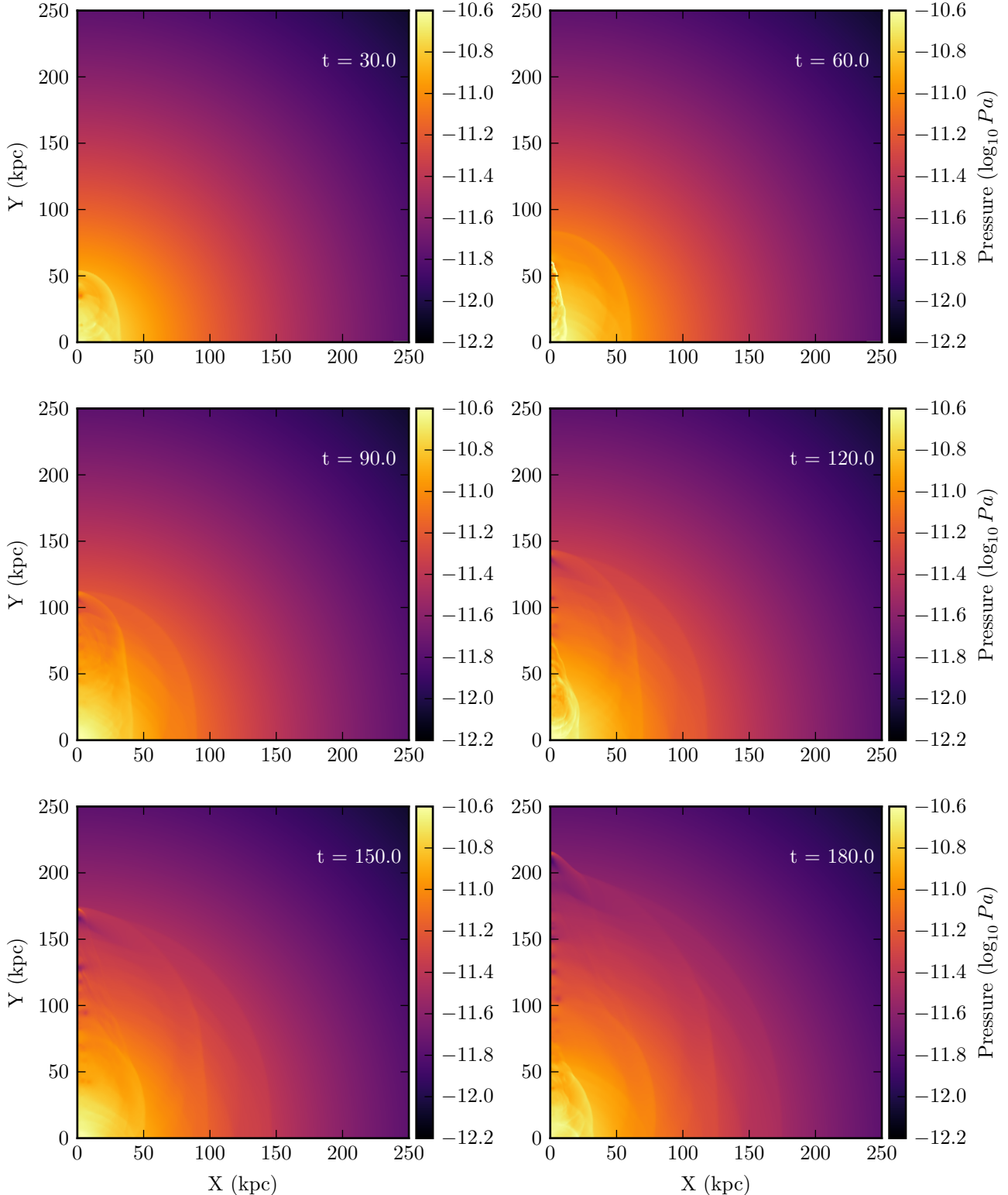


Figure 4.8: Pressure maps for 6 different simulation times, $t = 30, 60, 90, 120, 150$ and 180 Myr for $n = 4$ in a cluster environment, run code **m14.5-M25-n4**. The jet is switched on for: $t = 0 - 10$ Myr; $t = 50 - 60$ Myr; $t = 100 - 110$ Myr; and $t = 150 - 160$ Myr. Multiple bow shocks are visible in the later panels. The final outermost bow shock has a pinched shape at the head, due to a later bow shock punching through the earlier ones.

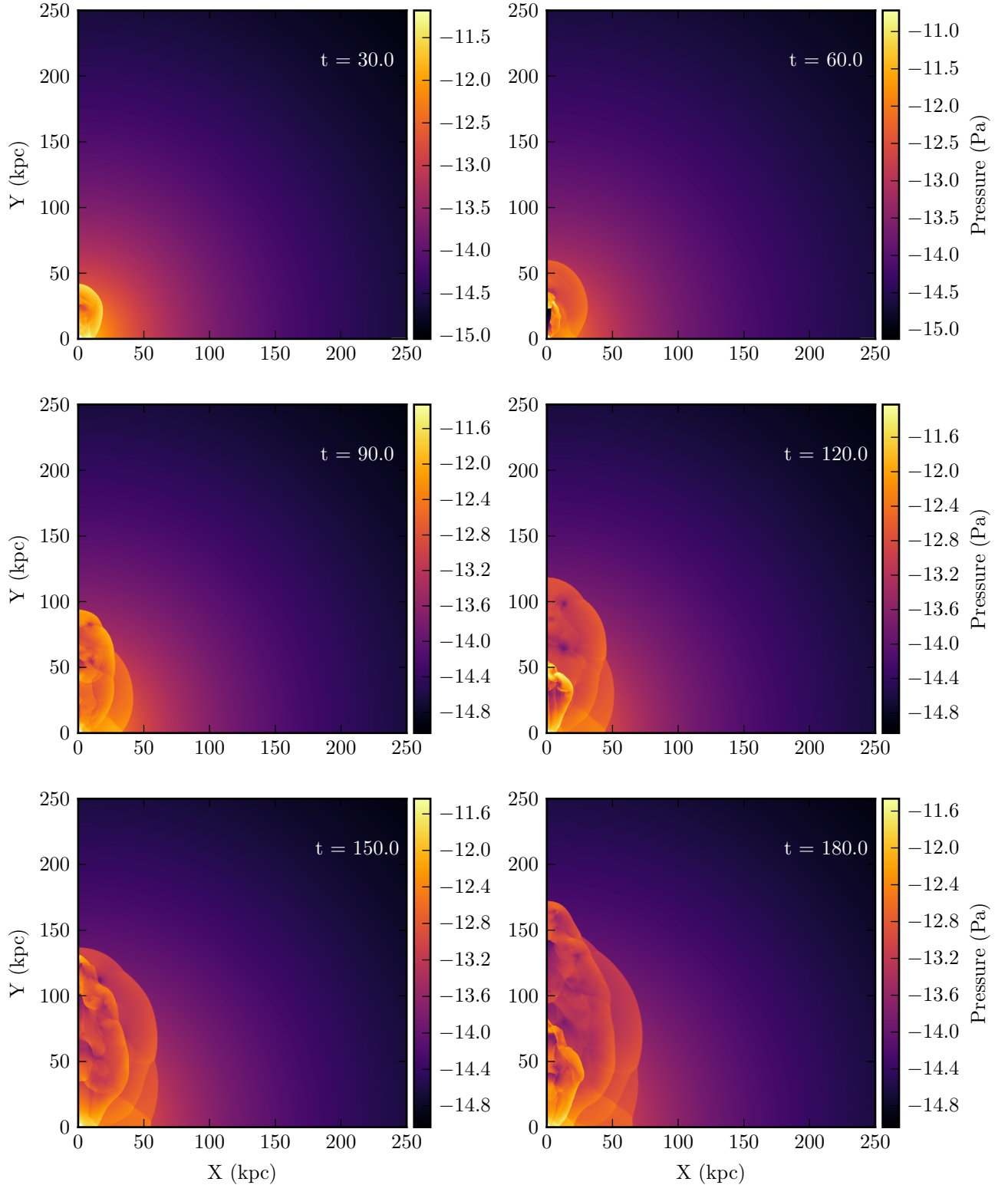


Figure 4.9: Pressure maps for 6 different simulation times, $t = 30, 60, 90, 120, 150$ and 180 Myr for $n = 4$ in a poor group environment, run code **m12.5-M25-n4**. The jet is switched on for: $t = 0 - 10$ Myr; $t = 50 - 60$ Myr; $t = 100 - 110$ Myr; and $t = 150 - 160$ Myr. Multiple bow shocks are visible in the later panels. The final outer shock structure is significantly different from the nearly spherical bow shock obtained for the corresponding $n = 1$ simulation.

4.2 Energy Components and Distribution

The energy injected onto the grid by the jet is calculated for the $n = 4$ runs in both the cluster and poor group environments following the methods outlined in Section 3.2. The resulting energy component plots are shown in Figures 4.10 and 4.11. The dotted total energy curve is obtained by summing up the energy in the three components; energy is clearly conserved as the total energy is constant when the jet is switched off, and increases linearly when the jet is switched on.

The restarting nature of the jet is evident in the total energy curves for both environments. The thermal and kinetic energy components are expected to be the most affected by restarting the jet, compared to the gravitational potential component. This is because restarting the jet does not dramatically affect the uplifting of gas from the centre, but it does increase the thermal and kinetic energy components.

Comparing Figures 4.10 and 4.11 with Figures 3.14 and 3.15, this expectation is correct. Looking at the gravitational potential energy curves, the gravitational potential energy component for the jet in the poor group environment is not significantly affected by the jet's restarting nature, while it is only slightly affected in the cluster environment. Gas near the core is swept up by the jet outburst, and then begins to refill close to the core once the jet is switched off; this could provide an explanation for the difference in environments. The refilling occurs faster in the cluster environment due to the higher halo mass, which means that subsequent outbursts in the cluster environment have more gas to uplift compared to subsequent outbursts in the poor group environment.

4.3 Feedback Efficiency

The comparison of feedback efficiency between $n = 1$ and $n = 4$ for the cluster environment is shown in Figure 4.12, while the comparison for the poor group environment is shown in Figure 4.13. The feedback efficiency is calculated as de-

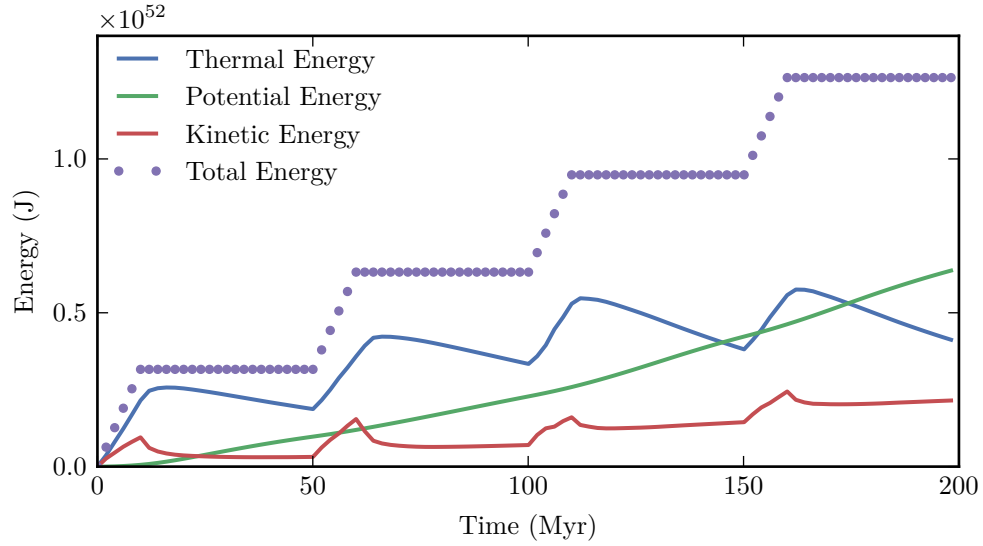


Figure 4.10: Total change of energy in the thermal, gravitational potential and kinetic energy components as well as the overall sum as a function of simulation time for $n = 4$ in the cluster environment, run code **m14.5-M25-n4**.

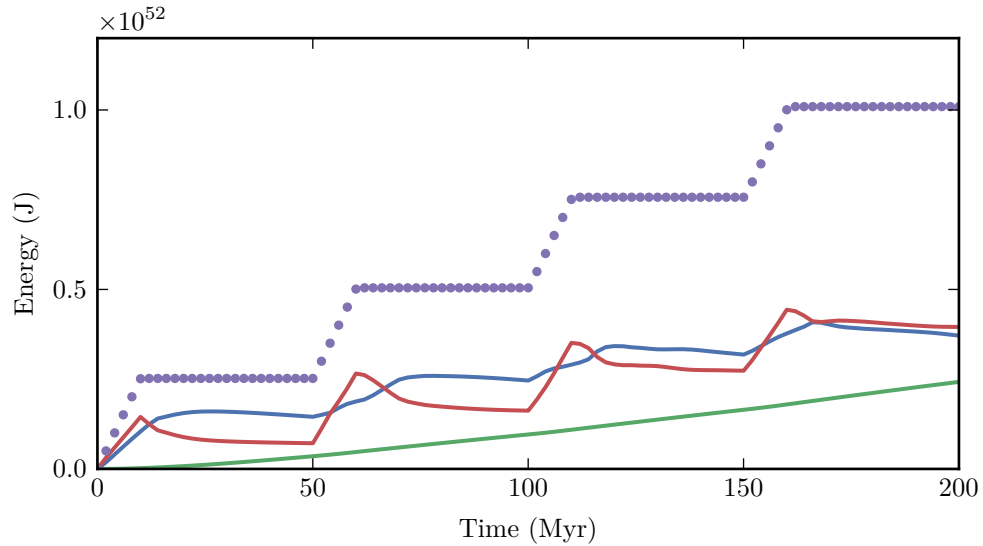


Figure 4.11: Total change of energy in the thermal, gravitational potential and kinetic energy components as well as the overall sum as a function of simulation time for $n = 4$ in the poor group environment, run code **m12.5-M25-n4**. The legend is the same as the one in Figure 4.10.

4.3. FEEDBACK EFFICIENCY

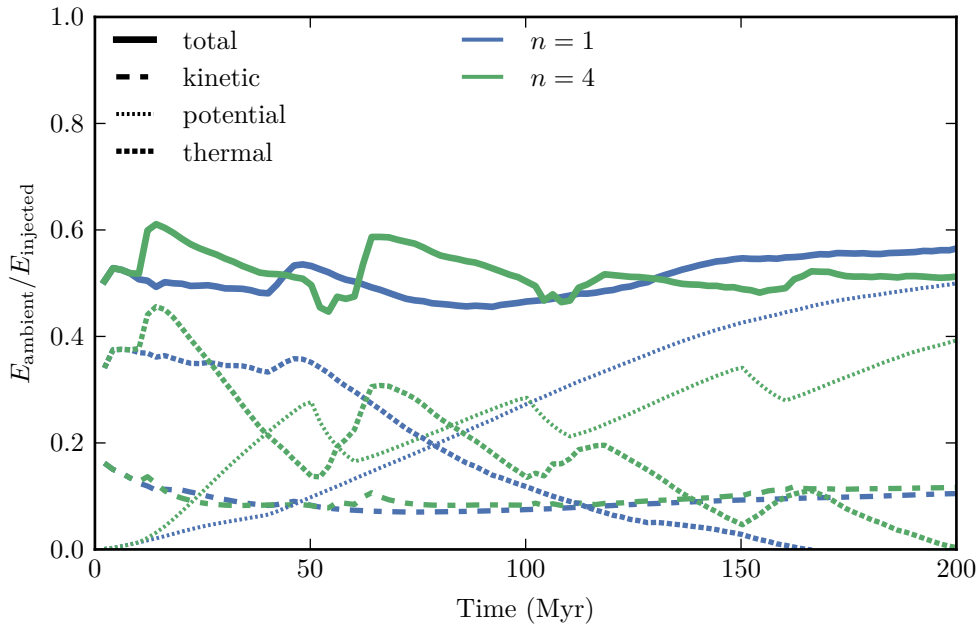


Figure 4.12: Feedback efficiency (fraction of injected energy that couples to ambient gas) as a function of simulation time for $n = 1$ and $n = 4$, in a cluster environment, run codes **m14.5-M25-n1** and **m14.5-M25-n4**.

scribed in Section 3.3, by taking the ratio of injected energy coupled to the ambient medium and total energy injected by the jet. It is clear that the feedback efficiency in the poor group environment is affected significantly by the changing number of outbursts, when compared to the cluster environment. A likely explanation for this is that, in the cluster, a large portion of the ambient energy that couples to the environment does so as gravitational potential energy. This agrees with the higher total gravitational potential energy for the cluster environment shown in Figure 4.10 compared to the poor group environment (see Figure 4.11), which is because the cluster environment has a higher total gas mass for the jet to do work against. The gravitational potential energy component is less affected by changing the number of outbursts due to the fact that all jet activity is going to be uplifting gas.

Meanwhile, the ambient energy in the poor group environment is more evenly distributed throughout the different components, and in particular much less energy

4.3. FEEDBACK EFFICIENCY

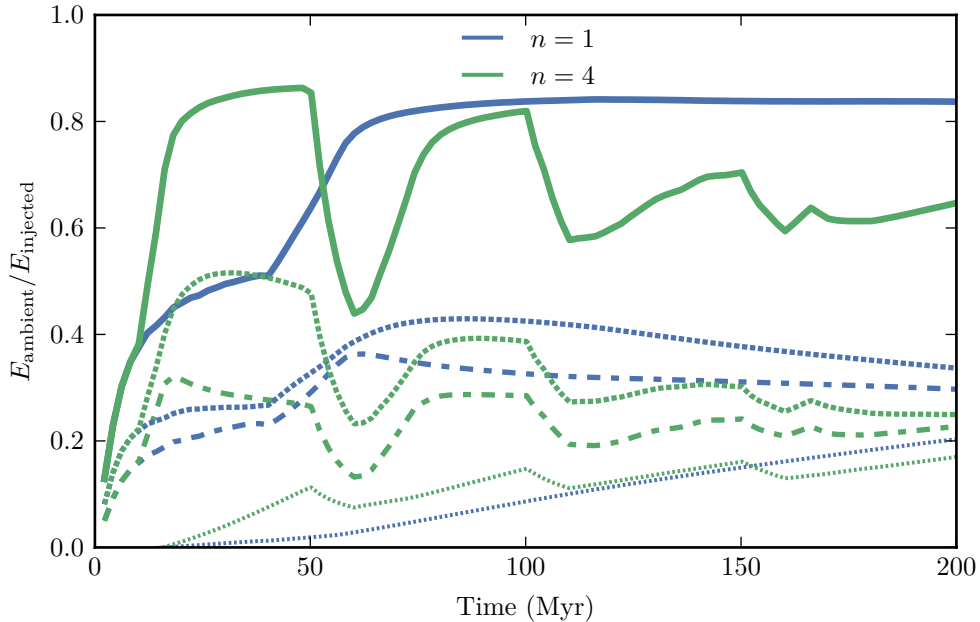


Figure 4.13: Feedback efficiency (fraction of injected energy that couples to ambient gas) as a function of simulation time for $n = 1$ and $n = 4$, in a poor group environment, run codes **m12.5-M25-n1** and **m12.5-M25-n4**. The legend is the same as the one shown in Figure 4.12.

is found in the gravitational potential energy component when compared with the cluster environment. The kinetic and thermal energy components are expected to be more affected by changing the number of outbursts; this is due to the lower average density and ambient temperature in the poor group environment, meaning that shocks have a greater effect on the energetics. It is not surprising that in the poor group environment where these components dominate, the total feedback efficiency is generally lower for later times in the $n = 4$.

There is a large difference in overall feedback efficiency between the two environments, which is true for both the $n = 1$ and $n = 4$ simulations. The feedback efficiency for the cluster is around 50 – 60%, while it is around 50 – 80% for the poor group. As discussed in Section 3.3 the absolute feedback efficiency for the cluster is dependent on the tracer cutoff used; however the basic result that the feedback efficiency is largely unaffected by the number of outbursts for the cluster

4.4. SURFACE BRIGHTNESS

environment remains true for a range of tracer cutoffs.

The sharp rise in feedback efficiency seen in both environments when the jet switches off is due to the mixing of the cocoon with ambient material, as discussed in Section 3.3. The feedback efficiency in the poor group environment decreases sharply at the beginning of each outburst, and never recovers to the original 80% for the latter two outbursts. The sudden decrease over the jet active time is because a large portion of injected energy for later outbursts does not couple with the ambient medium initially, and only couples through mixing once the jet is switched off. The feedback efficiency never recovers to the original 80% for later outbursts due to the dynamics of subsequent outbursts, as described in Section 4.1. Because subsequent outbursts are propagating into a predisturbed environment, the kinetic and thermal energy injected by these outbursts is transferred mostly to material from older outbursts, rather than the ambient medium. This is not seen in the feedback efficiency for the cluster due to the larger impact of the gravitational potential energy component. In the poor group, earlier outbursts are more effective than later ones at heating the ambient medium, which could mean that later outbursts need to be longer in order to maintain the heating/cooling balance discussed in Section 1.1.4.

4.4 Surface Brightness

The surface brightness plots for the simulations with multiple outbursts are calculated as outlined in Section 3.4. The comparisons of the $n = 1$ and $n = 4$ surface brightness maps are shown in Figure 4.14 and Figure 4.15 for the cluster and poor group environments respectively. There is a difference between the $n = 1$ and $n = 4$ simulations for both environments, however it is more pronounced in the poor group environment.

The $n = 1$ simulation in the group environment produces a surface brightness map that contains what could be an invisible lobe; where there is a physical structure in e.g. the density and pressure; however the radio source emission is very faint.

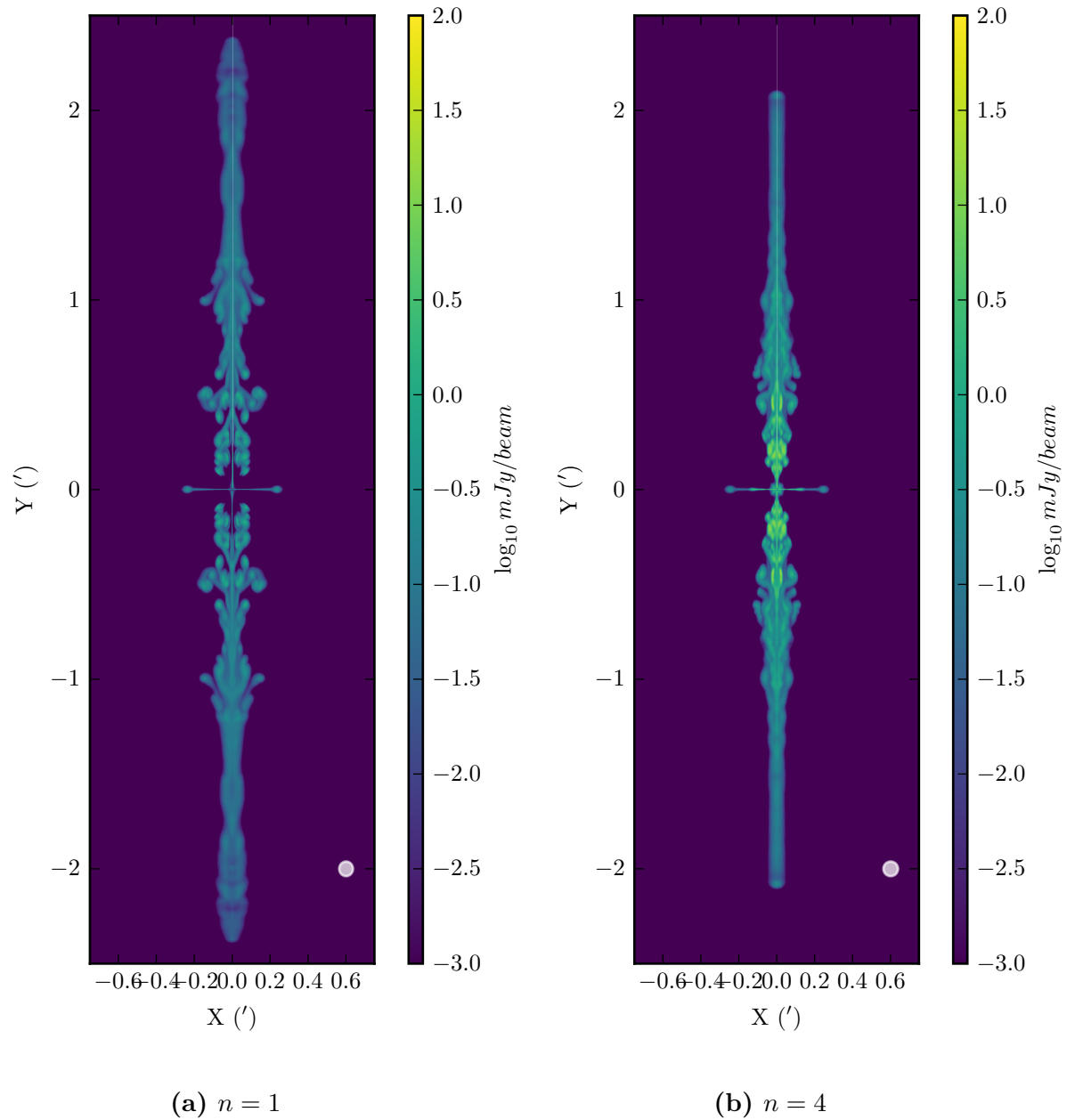


Figure 4.14: Surface brightness maps for the $n = 1$ and $n = 4$ jets in the cluster environment at the end of the simulation, time $t = 200$ Myr.

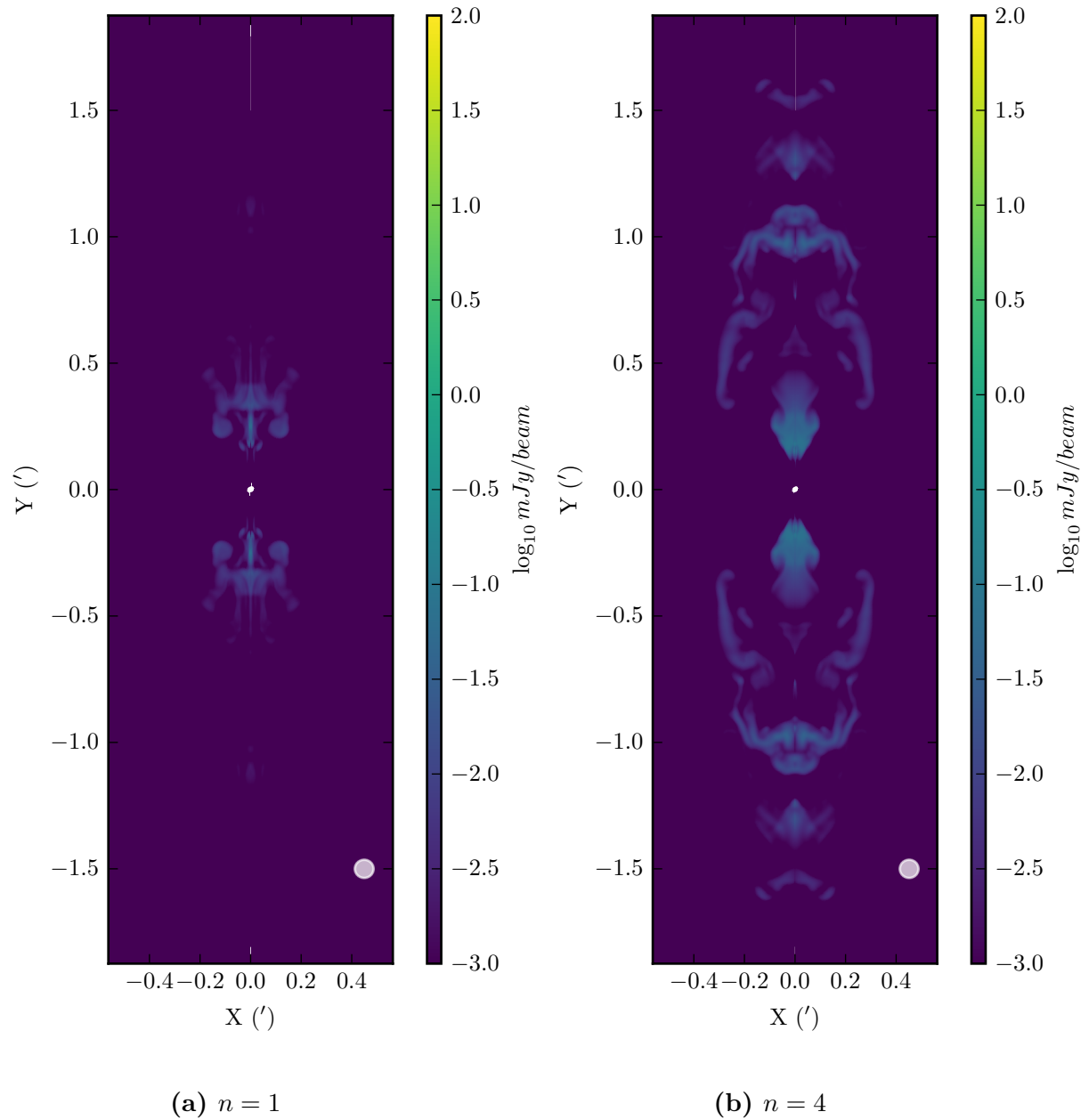


Figure 4.15: Surface brightness maps for the $n = 1$ and $n = 4$ jets in the poor group environment at the end of the simulation, time $t = 200$ Myr.

4.5. SIZE-LUMINOSITY DIAGRAM

Emission from this radio source would only be visible in observations sensitive to low surface brightness objects, such as the GLEAM survey using the Murchison Widefield Array (Wayth et al., 2015). One such low surface brightness object has already been found by Hurley-Walker et al. (2015) using this survey, NGC 1534, which at the time of discovery was the lowest surface brightness radio galaxy observed.

The $n = 1$ and $n = 4$ surface brightness distributions for the cluster environment both show roughly the same overall source length, however the $n = 4$ simulation is brighter near the core due to recent jet activity. This could have observational implications, since if a radio source were observed with FR II morphology but were brighter near the core, it could be due to restarted jet activity. If the cluster was at a higher redshift then dimmer parts of the surface brightness map would turn into invisible lobes as with the poor group.

Despite representing the underlying morphology, the surface brightness maps do not make it obvious that there is intermittent jet activity occurring. There are multiple structures present for the $n = 4$ simulation in the poor group environment, however they do not correspond directly to an outburst and are instead a function of the pressure in the turbulent cocoon as shown in Figure 4.9. The multiple bow shocks discussed in Section 4.1 would be visible in X-ray images as shown by Hardcastle & Krause (2013), however calculation of these is beyond the scope of this thesis.

For both environments later outbursts catch up to earlier ones, and there is no clear separation between outbursts. Classic double-double morphology is not reproduced due to the timescales simulated. The separation between outbursts would need to be an order of magnitude greater than that used for the simulations in this thesis.

4.5. SIZE-LUMINOSITY DIAGRAM

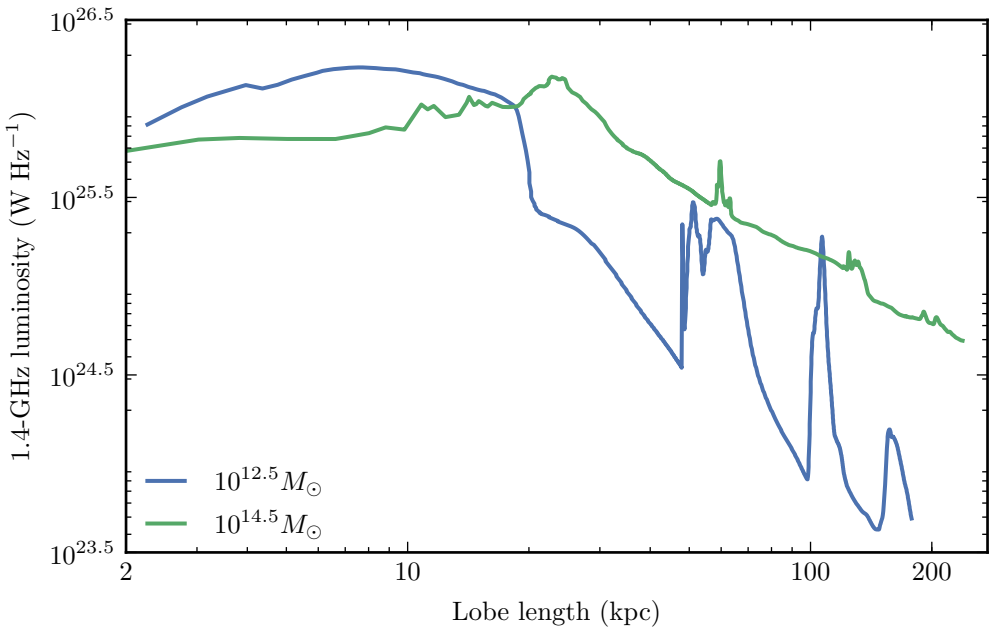


Figure 4.16: Size-luminosity diagram for the $n = 4$ jet in both the poor group and cluster environment, run codes **m12.5-M25-n4** and **m14.5-M25-n4**.

4.5 Size-Luminosity Diagram

In Section 3.5 I described the P-D diagram, which was introduced by Shklovskii (1963) as a tool for studying the temporal evolution of radio sources. As well as giving information about the jet power and duty cycle, the evolution of an intermittent jet through the P-D diagram gives insight into how the total source luminosity evolves with subsequent outbursts. The tracks in the P-D diagram are calculated using the same method described in Section 3.5, and the total luminosity is plotted as a function of lobe size for $n = 4$ simulations in the cluster and poor group environments in Figure 4.16.

It is expected that the P-D track for both environments will initially be the same as the tracks for the $n = 1$ jet, shown in Figure 3.20; however once the jet is switched off, the total luminosity of the source is expected to drop rapidly. Both of these features are reproduced in Figure 4.16: initially the P-D track for both environments matches the $n = 1$ tracks, and it then declines steeply as the jet is

4.5. SIZE-LUMINOSITY DIAGRAM

switched off and the source fades. The $n = 4$ jet in the poor group fades much more rapidly than the corresponding jet in the cluster once the jet is switched off. Because the synchrotron emission is calculated using pressure as a proxy for magnetic field, the reason for this difference is likely due to the lower average pressure in the poor group environment. This is supported by the $n = 4$ surface brightness maps for the cluster and poor group shown in Figures 4.14 and 4.15 respectively: the jet in the cluster has a much higher average surface brightness when compared to the jet in the poor group.

Outbursts after the initial one do not dramatically affect the P-D track for the jet in the cluster environment, however they do for the jet in the poor group environment. This could be because the total luminosity is already quite high in the cluster environment at later times, so subsequent outbursts have less effect. In contrast the poor group environment has a much lower total luminosity at later times, so the brief periods of jet activity have a much larger impact on the P-D track. Subsequent outbursts never increase the total luminosity to equal the initial peak, and later outbursts are always less luminous than the previous ones. This is due to the predisturbed environment into which later outbursts are propagating; if the quiescent time between outbursts were to be increased and the environment began to return to the initial state, I would predict that further active outbursts would reproduce the P-D track of the initial outburst.

As with the $n = 1$ jets, there is a very large evolution of the total luminosity over time, spanning approximately 3 dex. The number of outbursts that have previously occurred greatly affects the position of the source in the P-D diagram. An active source may appear to have the total luminosity equal to or less than that of an inactive source, which has implications for the observations of double-double radio galaxies. This is where the aforementioned surveys that are sensitive to low surface-brightness objects are important; I would predict that these surveys are likely to observe intermittent radio galaxies with short quiescent times (like those simulated in this thesis) that were previously undetected due to the lower effectiveness of later outbursts at increasing the total source luminosity.

4.6. SUMMARY

Finally, the simulations presented in this thesis do not provide any mechanism for handling electron losses. These losses could be accounted for using e.g. the luminosity model developed by Turner et al. (2016) that takes into account loss mechanisms and can be applied to any simulation source; or directly within the simulations by extending PLUTO to account for relativistic electrons, such as the REACON code, which is currently being developed by M. Krause, W. English and M. Hardcastle. If losses were accounted for, the evolution of spectral index over time could be tracked. The spectral index is expected to change as electrons are accelerated in shocks and lose energy via synchrotron and adiabatic losses.

4.6 Summary

In this chapter I examined how the number of outbursts a jet undergoes affects the morphology, energetics and observations. I compared $n = 1$ and $n = 4$ simulations in both the cluster and poor group environments. Simulations with $n = 2$ and $n = 3$ outbursts were also carried out, however they are generally intermediate cases between $n = 1$ and $n = 4$, so were not discussed in detail.

The preconditioning of the intracluster medium through earlier outbursts plays an important role in the resulting morphology of later outbursts. For both environments the total lobe length of the $n = 1$ simulation was greater than that of the $n = 4$ simulation, indicating that multiple outbursts are less effective than a single outburst at inflating a radio lobe. Additionally the evacuation of gas near the core by the initial outburst increases the collimation distance of subsequent outbursts, which in turn affects the morphology.

The number of outbursts also affects the energetics and feedback efficiency of the jets. The feedback efficiency of the jet in the poor group environment is greatly affected by subsequent outbursts: the initial outburst has a high feedback efficiency of around 80%, while later outbursts are always lower, with a final feedback efficiency of roughly 65% after all four outbursts. In contrast, the feedback efficiency of the jet in the cluster environment is minimally affected by the intermittent

4.6. SUMMARY

nature of the jet (this feature is reproduced for a range of tracer cutoff values), and is always roughly 50 – 60% for a tracer cutoff value of 0.005.

The observational signatures of restarting jets are subtle for the quiescent times simulated in this thesis: the key signature in the surface brightness maps is the brighter central region produced at later times due to recent jet activity in both the cluster and poor group environments. Each outburst produces a corresponding bow shock in the environment; these could be observed with X-ray images. Finally, the P-D diagram shows that the total source luminosity of later outbursts is never as high as the total source luminosity during the initial outburst, due to the preconditioning of the environment. This has implications for surveys sensitive to low surface-brightness, which may detect intermittent radio sources (with similar quiescent times to those simulated in this thesis) that have previously gone unobserved.

CHAPTER 5

Conclusions

In this thesis I carried out and analysed numerical simulations of radio jets. The environment into which the radio jet propagated was set by one of two gas density profiles: the first was the hydrostatic equilibrium gas density profile by Makino et al. (1998), while the second was the empirical β profile from King (1962). Two different dark matter halo masses were simulated, $M_{\text{halo}} = 10^{14.5} M_{\odot}$ corresponding to a cluster environment, and $M_{\text{halo}} = 10^{12.5} M_{\odot}$. A method of restarting the jet was developed, and different numbers of jet outbursts were examined.

Jets in the cluster environment produced longer and narrower lobes compared to those in the poor group environment, due to the smaller working surface for the cluster. Pre-processing the intracluster medium through earlier jet outbursts causes subsequent outbursts to collimate at later radii. This pre-processing also affects the energetics of the simulation for both environments. The thermal and kinetic energy components show increases when the jet is restarted, however no such change is seen in the gravitational potential component. The feedback efficiency of the jets is also affected: the feedback efficiency of the jet in the poor group is lower for later outbursts compared to the first one as later outbursts are less effective at transferring their thermal and kinetic energy to the ambient medium. This is not true for the jet in the cluster environment however, where the feedback efficiency does not change significantly with a different number of outbursts. The jets in the King environment were similar in morphology to their corresponding jets in the

Makino environment.

The surface brightness maps of the radio lobes show signs of intermittency for different numbers of jet outbursts. For $n = 4$ outbursts in a cluster environment, the radio lobe is brighter near the centre (see Figure 4.14). This indicates that an observation of a radio source showing this same brighter centre could be evidence for recent intermittent jet activity. While none of the simulations exactly reproduced a double-double radio galaxy morphology, restarting jets in the poor group environment produced something similar, see Figures 4.15 and B.16. Reproducing a more accurate DDRG structure would require longer jet active times with a shorter duty cycle. Observations of the jet width and lobe length can be used to determine the environment of the radio source, as shown with the different jet morphologies compared in Section 3.1. The P-D tracks produced from the simulations presented in this thesis agree qualitatively with dynamical models of radio sources (see Kaiser et al. (1997)), however the simulations would need to include electron acceleration and aging for a full comparison to be made.

The simulations were tested for convergence and reliability in Section 3.1.5. The simulation resolution was justified, along with the time scale used to ramp up or down the jet, and the injection radius used. The reproduction of FR II morphologies was confirmed in Section 3.1.

The uncertainties surrounding AGN feedback is a crucial issue in galaxy formation models, since it is the dominant mode of feedback for $z < 1$. Knowledge of how much energy the jet is injecting into the environment, and the efficiency with which this couples to the ambient medium, is needed to produce realistic distributions of galaxies. Numerical simulations are able to quantify the feedback efficiency, which can then be fed in to semi-analytic galaxy formation models. An obvious extension of this work would be to run a detailed suite of numerical simulations that covered a large range of parameters for environment, jet power, intermittency, jet opening angle and redshift, with the aim of creating a catalogue of feedback efficiencies for different environments. The environments used in these simulations would come from semi-analytic models.

Other possible extensions to the work carried out in this thesis include the inclusion of magnetic fields in simulations (which would provide polarisation information), cooling, simulating the entire plane with a counter-jet in order to break axial symmetry, 3D simulations, and longer timescales. It is likely that these extensions will be the subject of future studies.

APPENDIX A

The Hydrostatic Equilibrium Gas Density Profile

The profile for gas density derived by Makino et al. (1998) is obtained by putting the gas in hydrostatic equilibrium with the gravitational potential from the dark matter halo. The general hydrostatic equilibrium equation is

$$\nabla P = -\rho \nabla \Phi$$

which simplifies to

$$\frac{dP}{dr} = -\rho \frac{d\Phi}{dr}$$

for spherical symmetry. Here P is the pressure of the gas, ρ is the gas density, and Φ is the gravitational potential, given by

$$\Phi = \frac{-GM(r)}{r}$$

where G is the gravitational constant and $M(r)$ is the mass enclosed within the radius r . Finally, the hydrostatic equilibrium equation is

$$\frac{dP}{dr} = \frac{-\Phi}{r} \rho = \frac{-\rho GM(r)}{r^2}$$

This can be integrated as

$$\int_{P_0}^P \frac{1}{\rho(P')} dP' = - \int_{\Phi_0}^{\Phi} d\Phi' = -G \int_0^r \frac{M(r')}{r'^2} dr'$$

to give

$$\frac{\rho(r)}{\rho_0} = \exp \left[-G \frac{\rho_0}{P_0} \int_0^r \frac{M(r')}{r'^2} dr' \right] \quad (\text{A.1})$$

where an ideal isothermal gas is assumed, giving

$$P = \frac{k_B T}{\mu m_H} \rho = \frac{P_0}{\rho_0} \rho(r)$$

and k_B is the Boltzmann constant, T is the virial temperature of the gas, μ is the mean molecular mass and m_H is the mass of hydrogen.

This can be simplified by assuming that the gas does not contribute to the gravitational potential, and furthermore by considering a system containing only gas and a dark matter halo. Now Φ is simply due to the gravitational potential of the dark matter halo, which has a density profile given by Navarro et al. (1997) as

$$\rho_{\text{DM}} = \frac{\delta_c \rho_c}{(r/r_s)(1+r/r_s)^2}$$

where δ_c is the concentration parameter, ρ_c is the critical density, and r_s is the scale radius.

The mass function $M(r)$ is then just the integral

$$M(r) = \int_0^r 4\pi r'^2 \rho_{\text{DM}}(r') dr'$$

which gives

$$M(r) = 4\pi r_s^3 \delta_c \rho_c \left[\ln \left(1 + \frac{r}{r_s} \right) - \frac{r}{r + r_s} \right]$$

This can be substituted into Equation (A.1) to give the gas density ρ (Makino et al., 1998) as

$$\rho(r) = \rho_0 e^{-27b/2} \left(1 + \frac{r}{r_s}\right)^{27b/(2r/r_s)} \quad (\text{A.2})$$

where

$$b = \frac{8\pi G \mu m_H \delta_c \rho_c r_s^2}{27 k_B T}$$

The central density, ρ_0 , can be found by integrating Equation (A.2) for $\rho(r)$ out to the virial radius and setting it equal to the total baryonic mass in the system, which is known through the virial mass, baryonic matter fraction Ω_b , and the gas fraction f_{gas} .

APPENDIX B

Radio Jets with Two and Three Outbursts

This appendix contains plots for the evolution of density, pressure, energy components and feedback efficiency for jets with $n = 2$ and $n = 3$ outbursts in the cluster and poor group environments, runs **m14.5-M25-n2**, **m14.5-M25-n3**, **m12.5-M25-n2**, and **m12.5-M25-n3**.

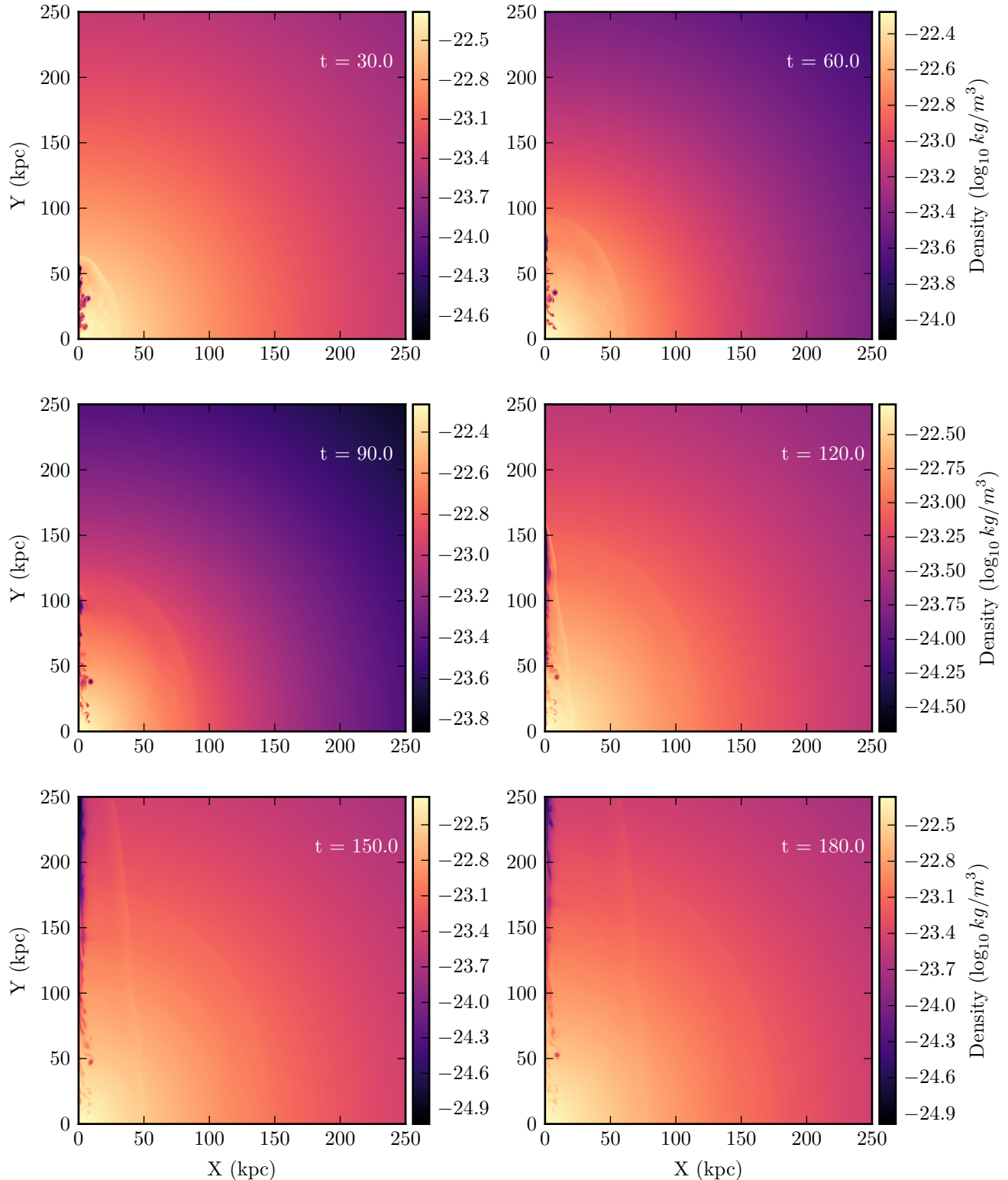


Figure B.1: Same as Figure 3.7 but for $n = 2$, run code m14.5-M25-n2.

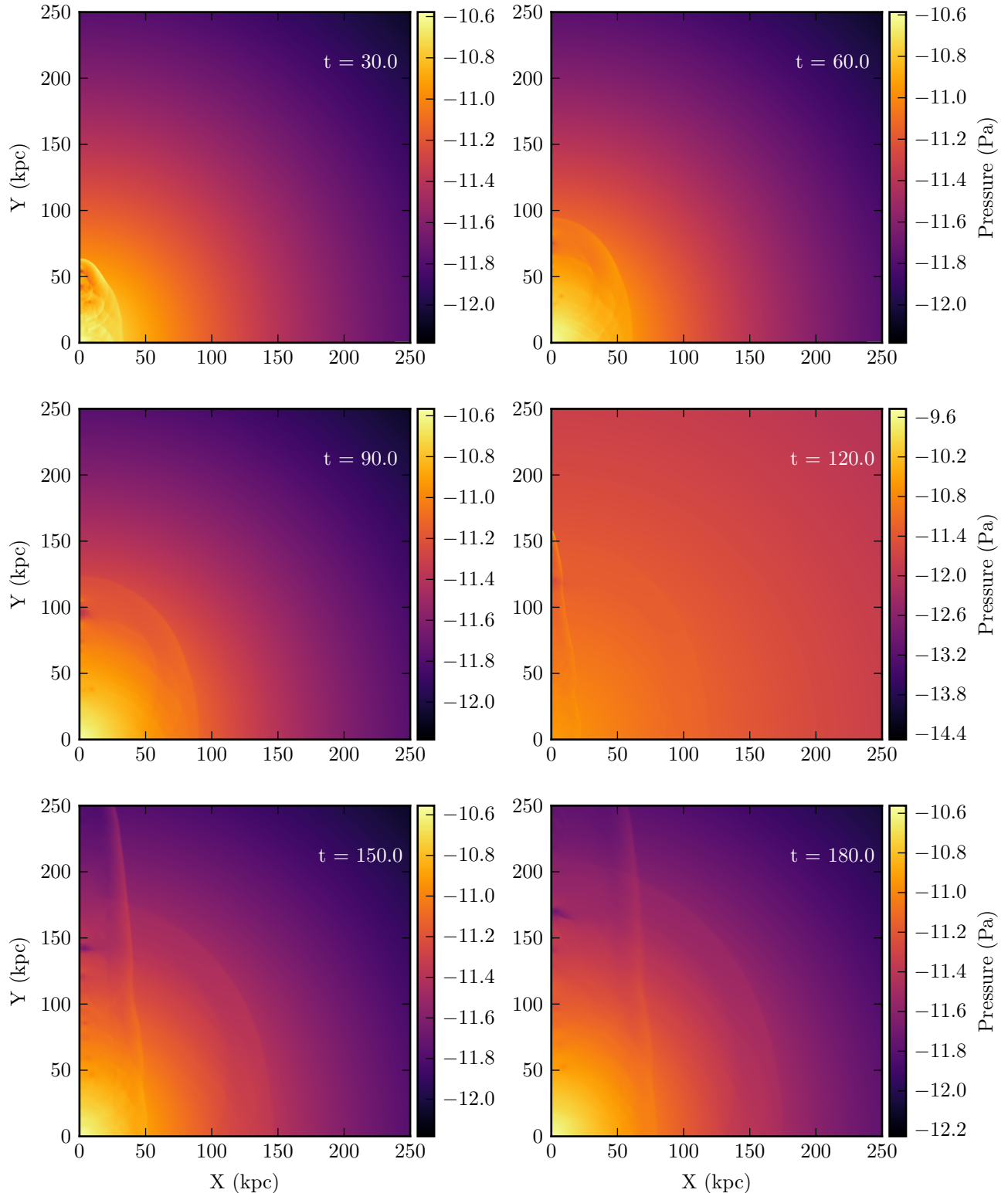


Figure B.2: Same as Figure 3.9 but for $n = 4$, run code m14.5-M25-n2.

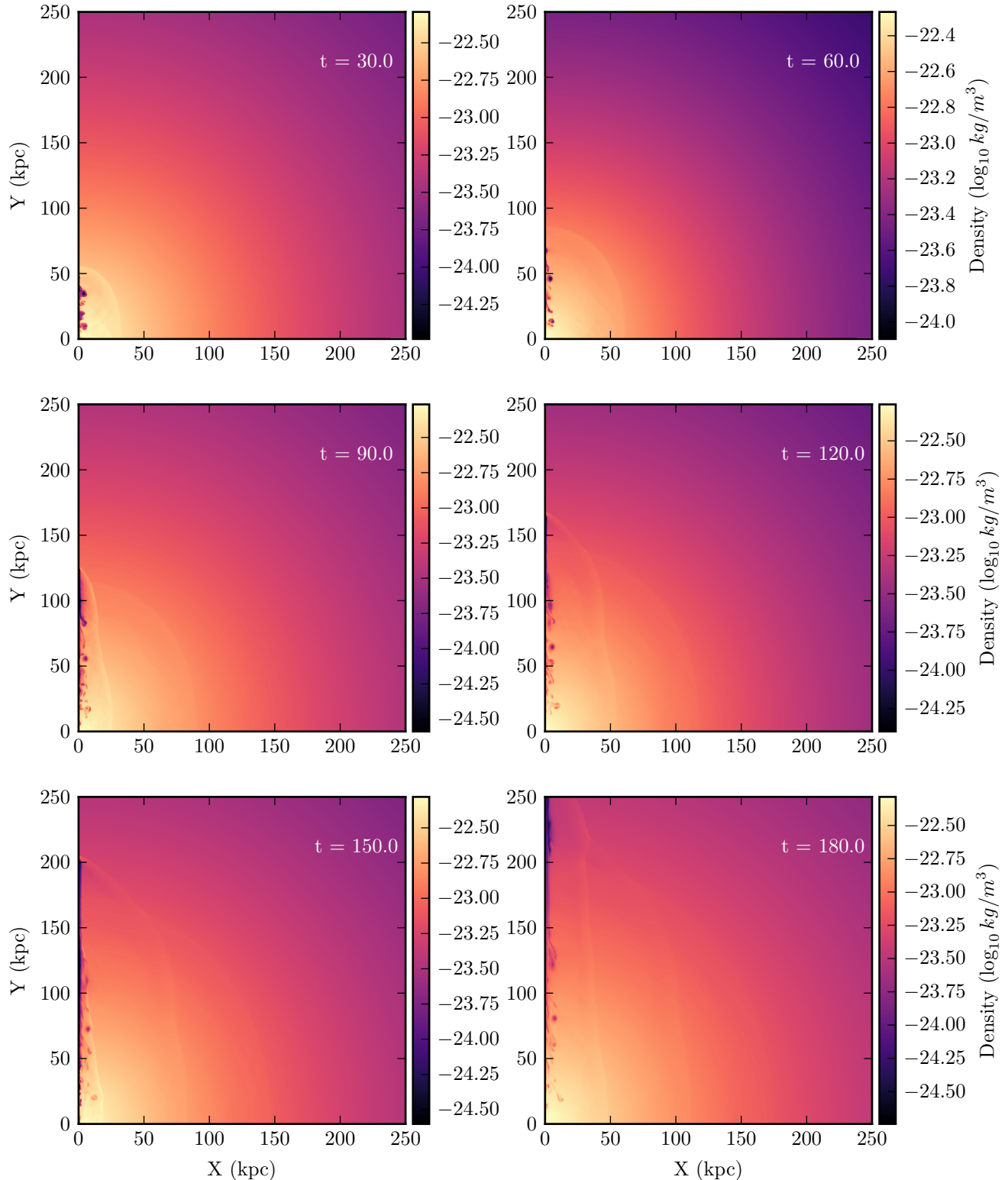


Figure B.3: Same as Figure 3.7 but for $n = 4$, run code m14.5-M25-n3.

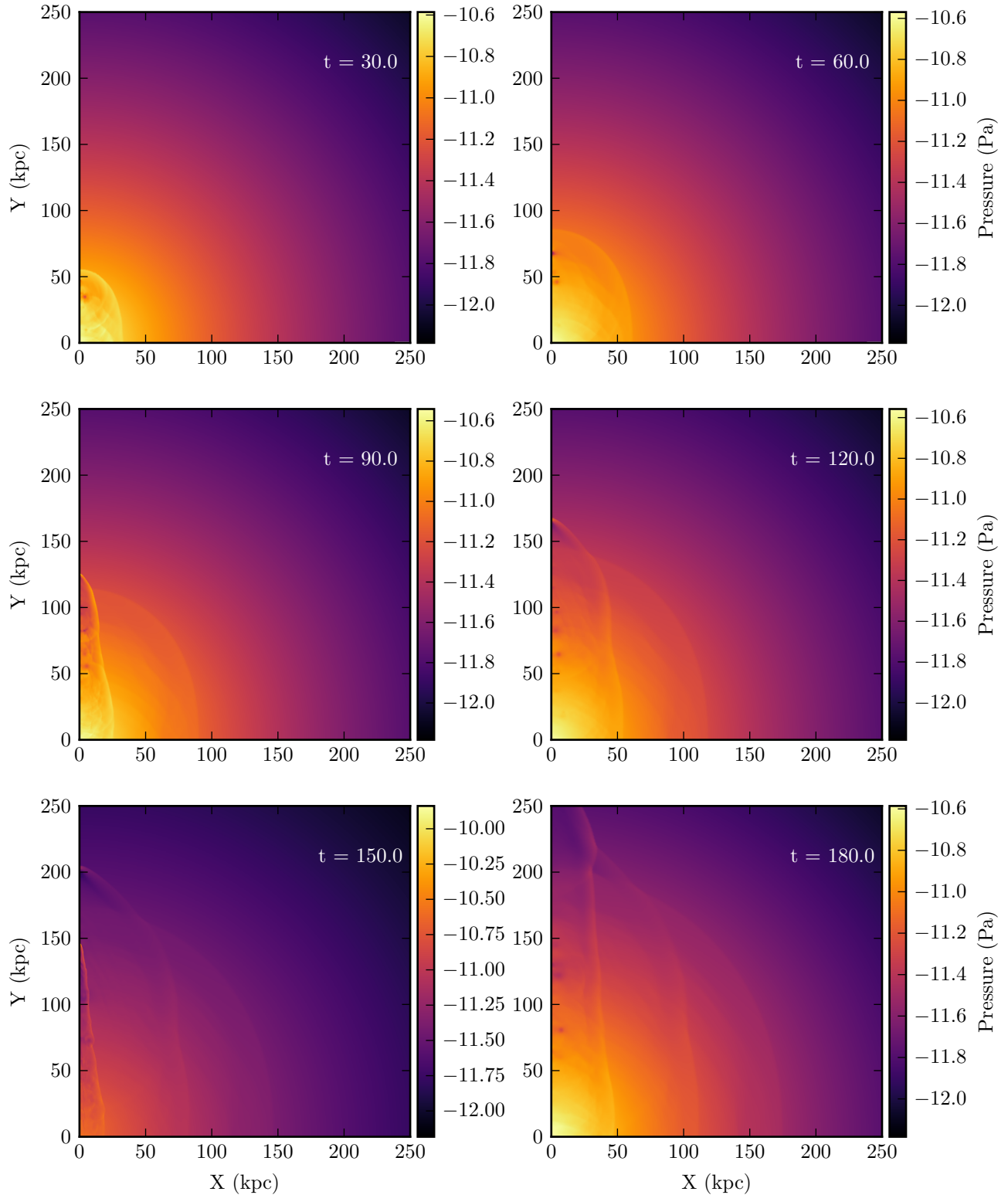


Figure B.4: Same as Figure 3.9 but for $n = 4$, run code m14.5-M25-n3.

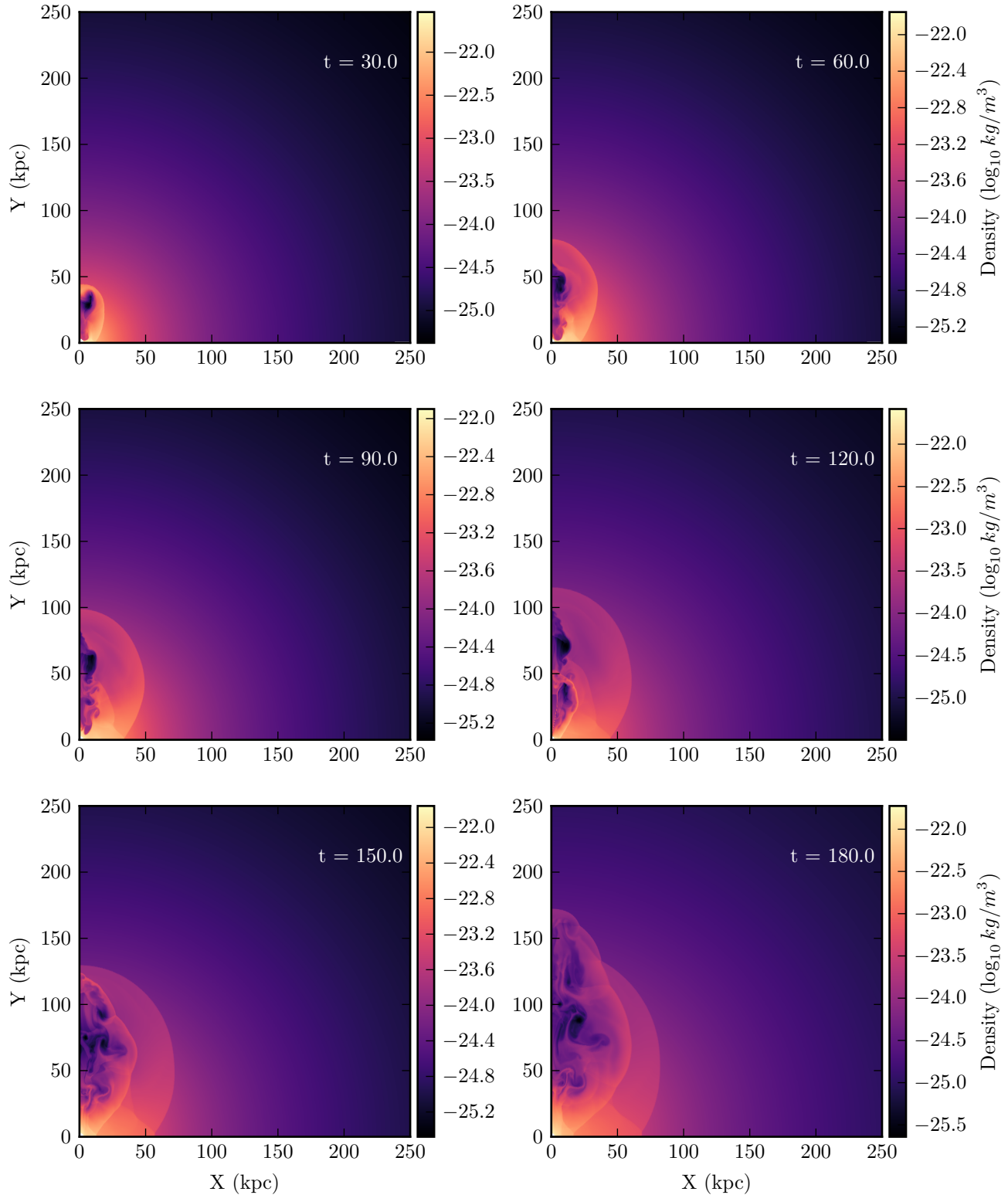


Figure B.5: Same as Figure 3.8 but for $n = 4$, run code m12.5-M25-n2.

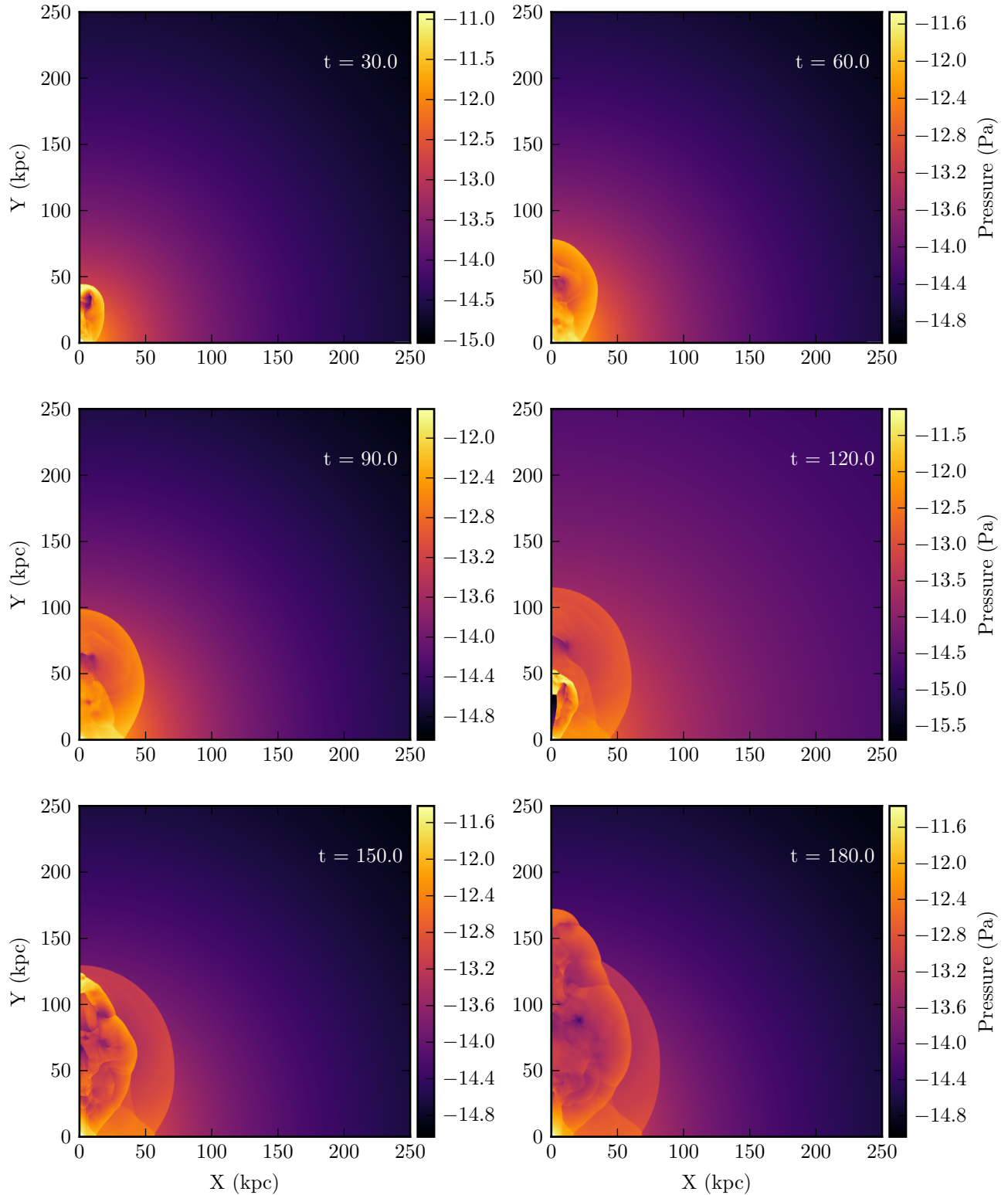


Figure B.6: Same as Figure 3.10 but for $n = 4$, run code m12.5-M25-n2.

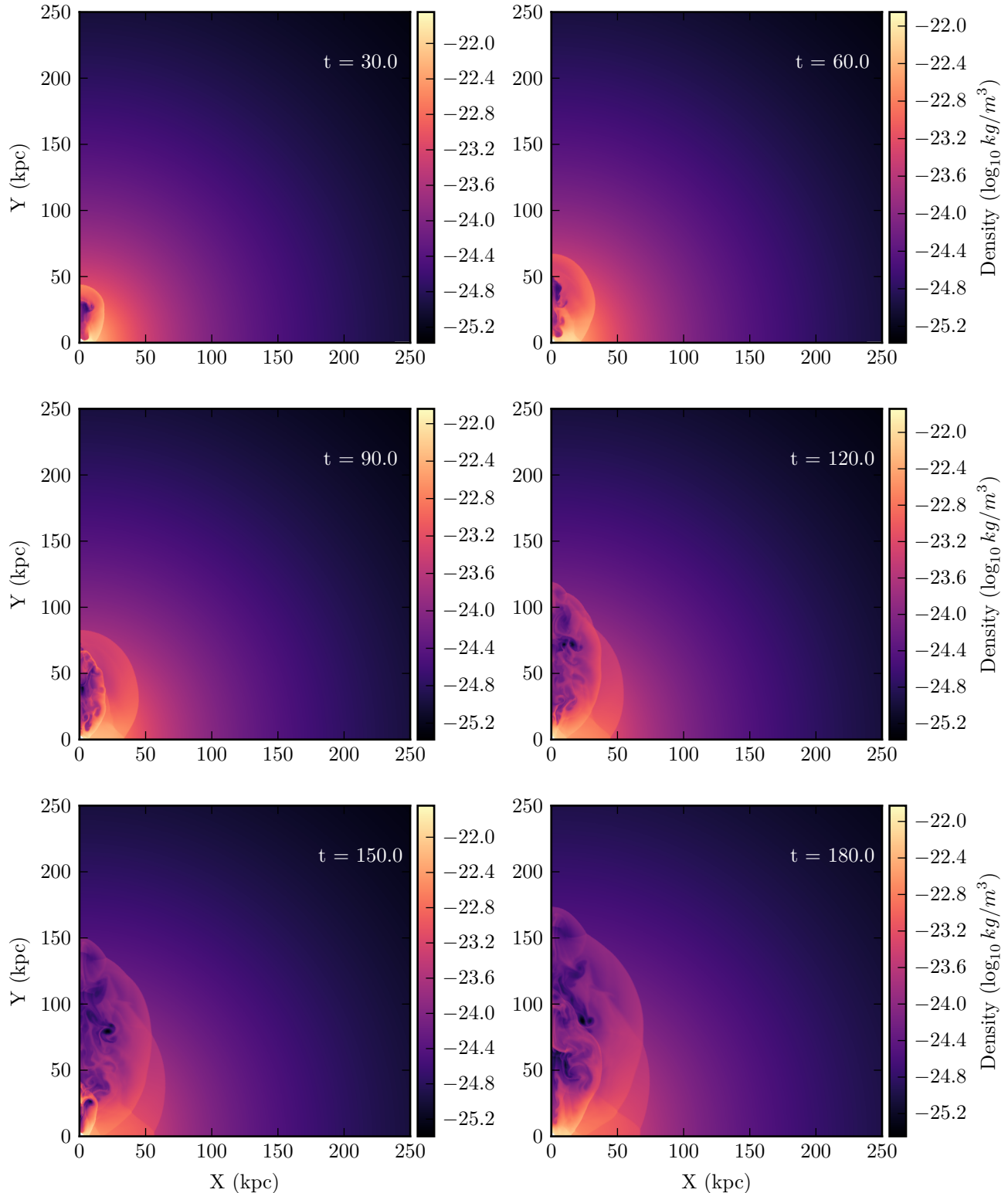


Figure B.7: Same as Figure 3.8 but for $n = 4$, run code m12.5-M25-n3.

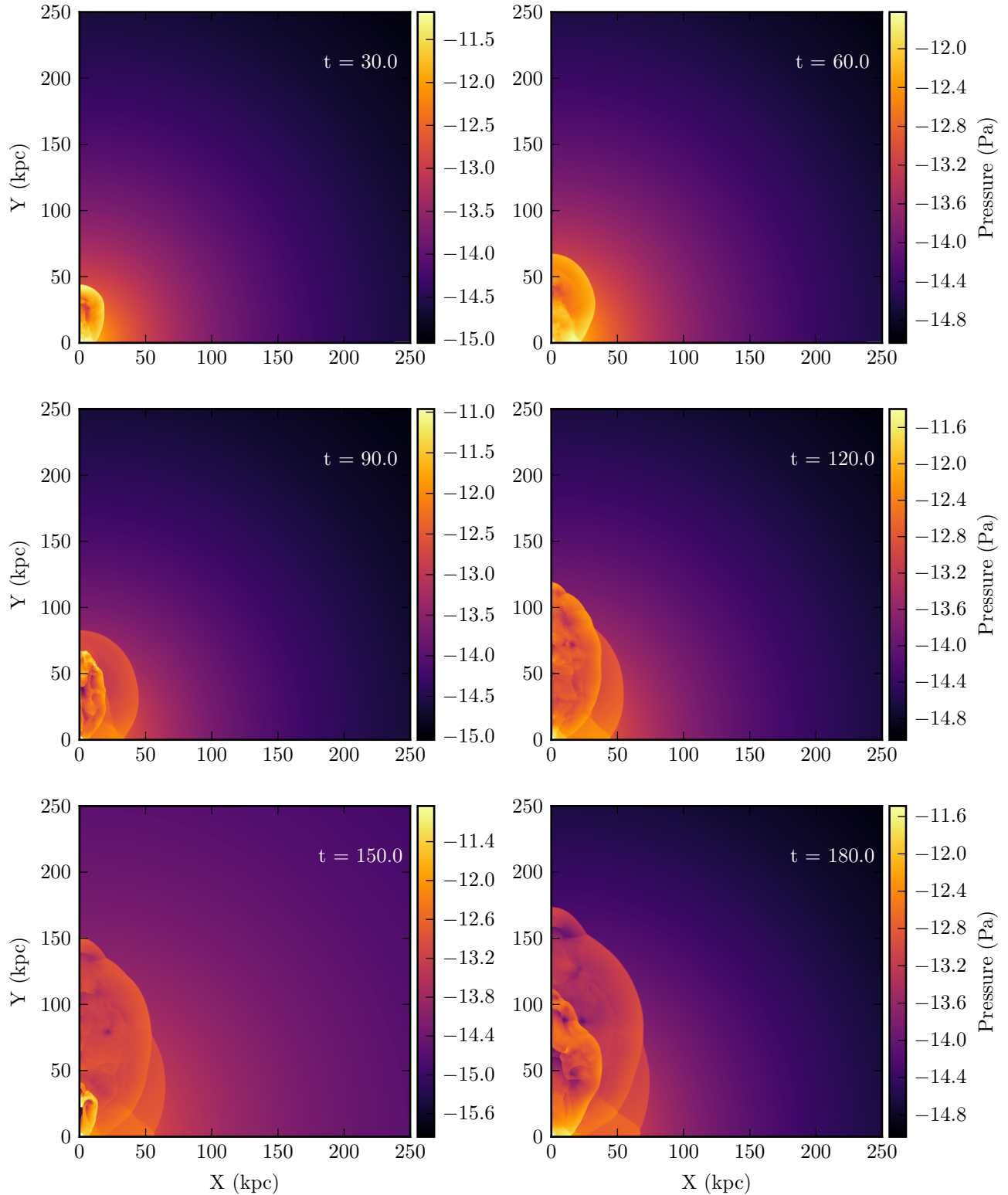


Figure B.8: Same as Figure 3.10 but for $n = 4$, run code m12.5-M25-n3.

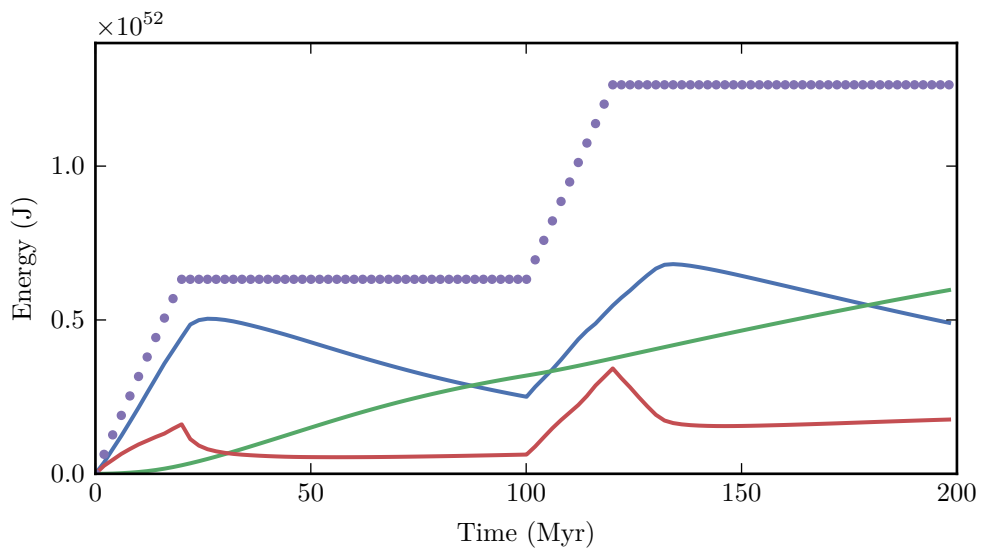


Figure B.9: Same as Figure 3.14 but for $n = 2$.

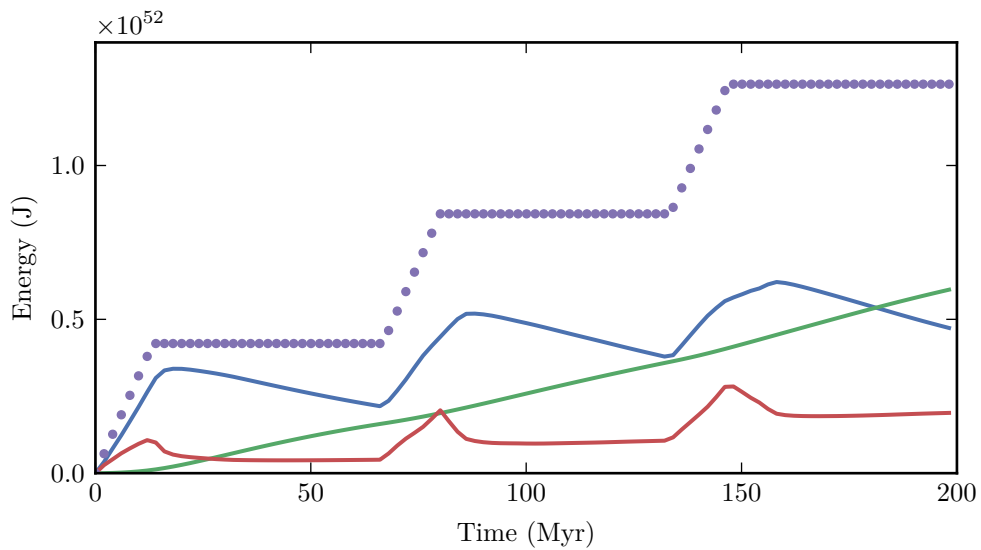


Figure B.10: Same as Figure 3.14 but for $n = 3$.

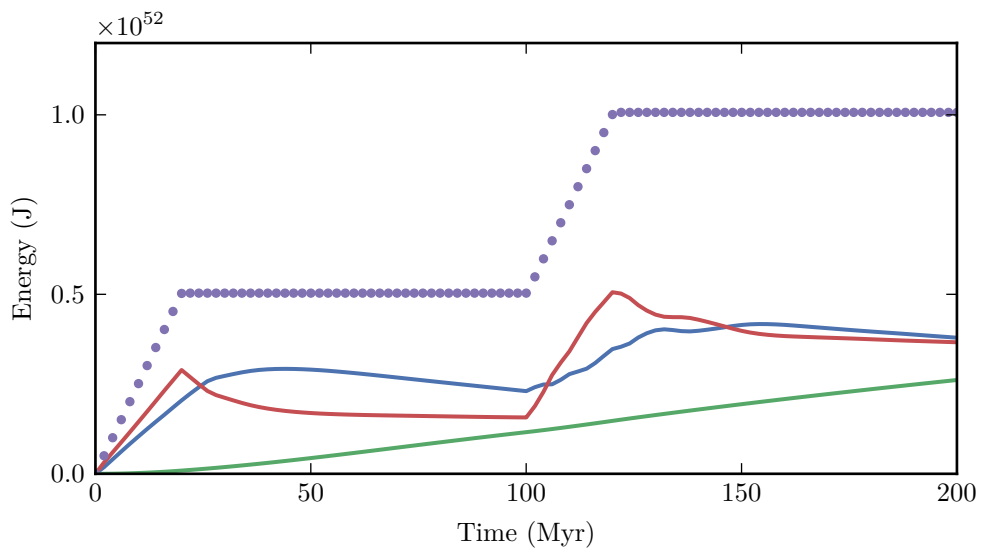


Figure B.11: Same as Figure 3.15 but for $n = 2$.

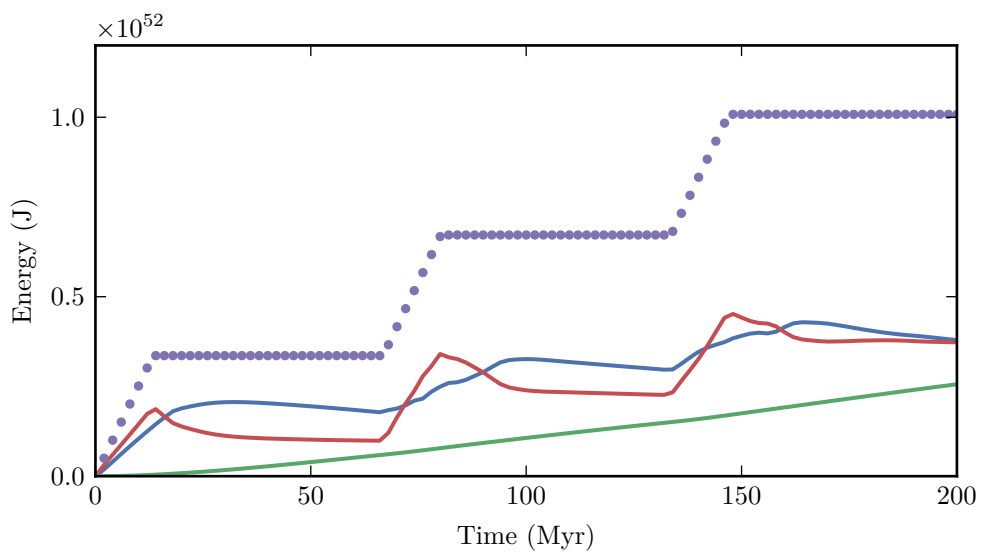


Figure B.12: Same as Figure 3.15 but for $n = 3$.

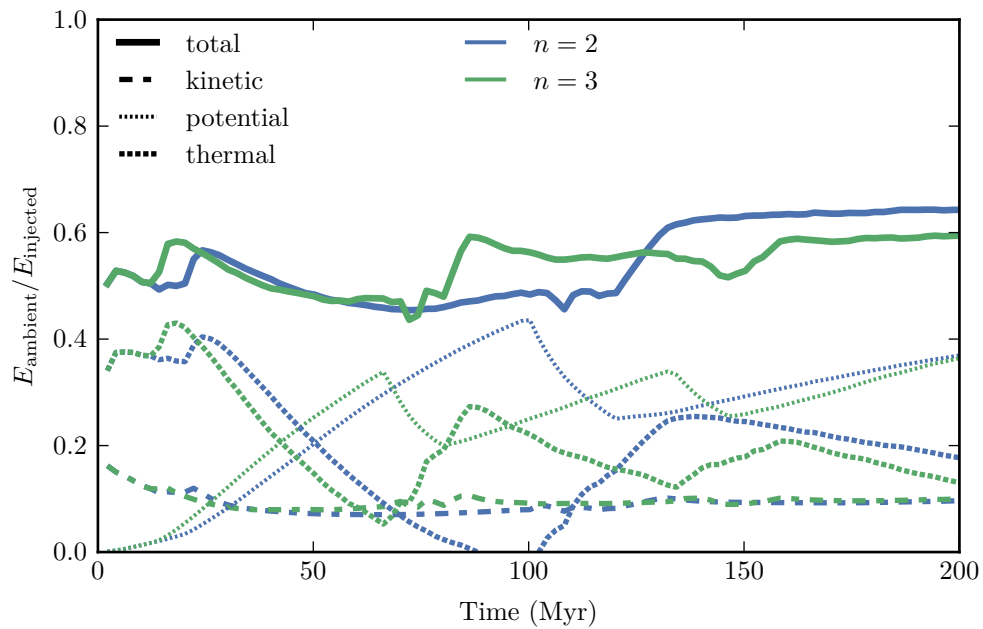


Figure B.13: Feedback efficiency (fraction of injected energy that couples to ambient gas) as a function of simulation time for $n = 2$ and $n = 3$, in a cluster environment, run codes m14.5-M25-n2 and m14.5-M25-n3.

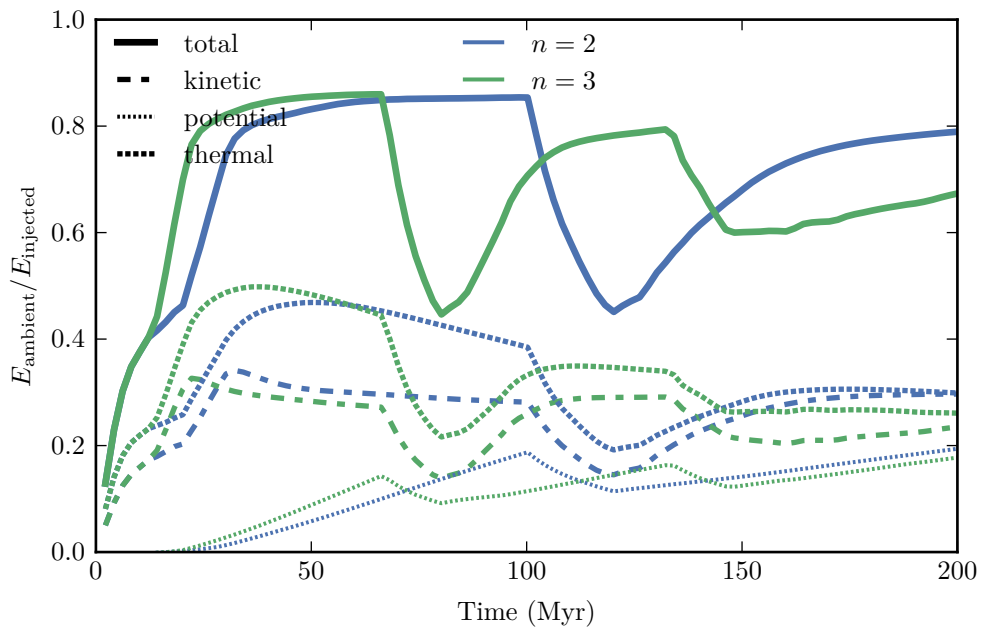


Figure B.14: Feedback efficiency (fraction of injected energy that couples to ambient gas) as a function of simulation time for $n = 2$ and $n = 3$, in a poor group environment, run codes m12.5-M25-n2 and m12.5-M25-n3.

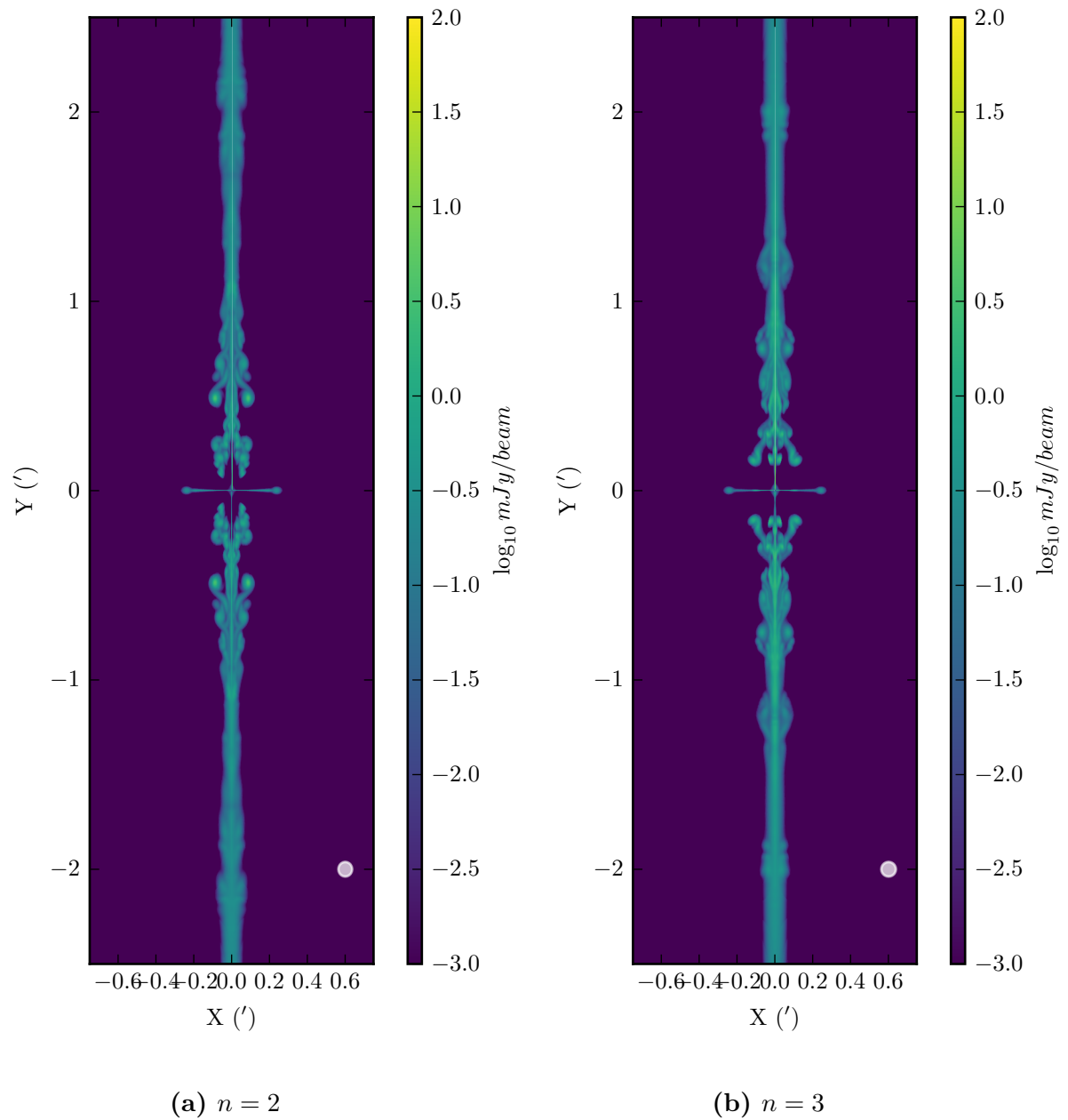


Figure B.15: Same as Figure 4.14 but for $n = 2$ and $n = 3$.

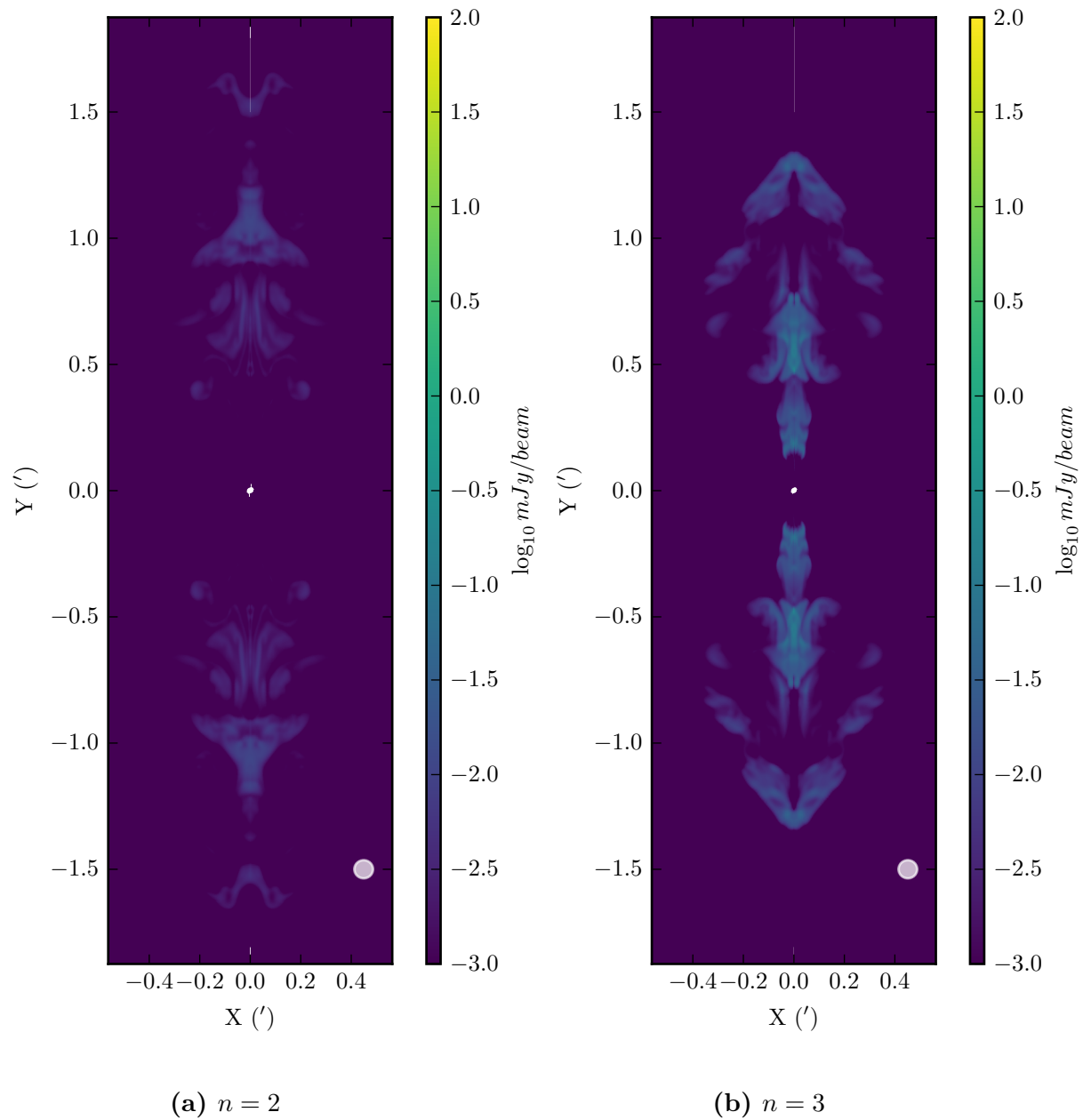


Figure B.16: Same as Figure 4.15 but for $n = 2$ and $n = 3$.

BIBLIOGRAPHY

- Aghanim, N., Arnaud, M., Ashdown, M., et al. 2016, *Astronomy & Astrophysics*, 594, A11
- Alexander, D., & Hickox, R. 2012, *New Astronomy Reviews*, 56, 93
- Alexander, P. 2002, *Monthly Notices of the Royal Astronomical Society*, 335, 610
- . 2006, *Monthly Notices of the Royal Astronomical Society*, 368, 1404
- Alexander, P., & Pooley, G. G. 1995, Cygnus A – Studay of a Radio Galaxy
- Alouani Bibi, F., Binney, J., Blundell, K., & Omma, H. 2007, *Astrophysics and Space Science*, 311, 317
- Becker, R. H., White, R. L., & Helfand, D. J. 1995, *The Astrophysical Journal*, 450, 559
- Belan, M., De Ponte, S., Massaglia, S., & Tordella, D. 2004, *Astrophysics and Space Science*, 293, 225
- Belan, M., De Ponte, S., & Tordella, D. 2008, *Experiments in Fluids*, 45, 501
- . 2010, *Physical Review E - Statistical, Nonlinear, and Soft Matter Physics*, 82, 1
- Belan, M., Massaglia, S., Tordella, D., Mirzaei, M., & de Ponte, S. 2013, *Astronomy & Astrophysics*, 554, A99
- Best, P. 2009, *Astronomische Nachrichten*, 330, 184
- Best, P. N., Von Der Linden, A., Kauffmann, G., Heckman, T. M., & Kaiser, C. R. 2007, *Monthly Notices of the Royal Astronomical Society*, 379, 894
- Blandford, R. D., & Rees, M. J. 1974, *Monthly Notices of the Royal Astronomical Society*, 169, 395
- Boehringer, H., Voges, W., Fabian, A. C., Edge, A. C., & Neumann, D. M. 1993, *Monthly Notices of the Royal Astronomical Society*, 264, L25

BIBLIOGRAPHY

- Bondi, H. 1952, Mnras, 112, 195
- Bryan, G. L., Norman, M. L., O'Shea, B. W., et al. 2014, The Astrophysical Journal Supplement Series, 211, 19
- Bullock, J. S., Kolatt, T. S., Sigad, Y., et al. 2001, Monthly Notices of the Royal Astronomical Society, 321, 559
- Capelo, P. R., Natarajan, P., & Coppi, P. S. 2010, Monthly Notices of the Royal Astronomical Society, 407, 1148
- Carniani, S., Marconi, A., Maiolino, R., et al. 2016, arXiv:1604.04290
- Cattaneo, a., Faber, S. M., Binney, J., et al. 2009, Nature, 460, 213
- Cavaliere, A., & Fusco-Femiano, R. 1978, Astronomy and Astrophysics, 70, 677
- Chon, G., Boehringer, H., Krause, M., & Truemper, J. 2012, Arxiv.Org, 3, 4
- Churazov, E., Brüggen, M., Kaiser, C. R., Boehringer, H., & Forman, W. R. 2001, The Astrophysical Journal, 554, 261
- Clarke, D. A., & Burns, J. O. 1991, The Astrophysical Journal, 369, 308
- Crockett, R. M., Shabala, S. S., Kaviraj, S., et al. 2012, Monthly Notices of the Royal Astronomical Society, 421, 1603
- Croston, J. H., Hardcastle, M. J., Harris, D. E., et al. 2005, The Astrophysical Journal, 626, 733
- Croton, D. J., Springel, V., White, S. D. M., et al. 2006, Monthly Notices of the Royal Astronomical Society, 365, 11
- De Lucia, G., & Blaizot, J. 2007, Monthly Notices of the Royal Astronomical Society, 375, 2
- Donohoe, J., & Smith, M. D. 2016, Monthly Notices of the Royal Astronomical Society, 458, 558
- Dutton, A. A., & Maccio, A. V. 2014, Monthly Notices of the Royal Astronomical Society, 441, 3359
- English, W., Hardcastle, M. J., & Krause, M. G. H. 2016, Monthly Notices of the Royal Astronomical Society, 443, stw1407
- Fabian, A. 2012, Annual Review of Astronomy and Astrophysics, 50, 455
- Fabian, A. C., Sanders, J. S., Allen, S. W., et al. 2003, Monthly Notices of the Royal Astronomical Society, 344, L43

BIBLIOGRAPHY

- Fanaroff, B. L., & Riley, J. M. 1974, Monthly Notices of the Royal Astronomical Society, 167, 31P
- Fryxell, B., Olson, K., Ricker, P., et al. 2000, The Astrophysical Journal Supplement Series, 131, 273
- Giodini, S., Pierini, D., Finoguenov, A., et al. 2009, The Astrophysical Journal, 703, 982
- Hardcastle, M. J., & Krause, M. G. H. 2013, Monthly Notices of the Royal Astronomical Society, 430, 174
- . 2014, Monthly Notices of the Royal Astronomical Society, 443, 1482
- Hardcastle, M. J., Worrall, D. M., Birkinshaw, M., Laing, R. A., & Bridle, A. H. 2002, Monthly Notices of the Royal Astronomical Society, 334, 182
- Hardcastle, M. J., Lenc, E., Birkinshaw, M., et al. 2015, Monthly Notices of the Royal Astronomical Society, 455, 3526
- Heckman, T. T. M., & Best, P. N. P. 2014, Annual Review of Astronomy and Astrophysics, 52, 589
- Hurley-Walker, N., Johnston-Hollitt, M., Ekers, R., et al. 2015, Monthly Notices of the Royal Astronomical Society, 447, 2468
- Kaiser, C. R., & Alexander, P. 1997, Monthly Notices of the Royal Astronomical Society, 286, 215
- Kaiser, C. R., Dennett-Thorpe, J., & Alexander, P. 1997, Monthly Notices of the Royal Astronomical Society, 732, 8
- Kaiser, C. R., Schoenmakers, A. P., & Rottgering, H. J. A. 2000, Monthly Notices of the Royal Astronomical Society, 315, 381
- King, I. 1962, The Astronomical Journal, 67, 471
- Klypin, A., Yepes, G., Gottlöber, S., Prada, F., & Heß, S. 2016, Monthly Notices of the Royal Astronomical Society, 457, 4340
- Komissarov, S. S., & Falle, S. A. E. G. 1998, 1108, 1087
- Krause, M. 2003, Astronomy and Astrophysics, 398, 113
- Krause, M., Alexander, P., Riley, J., & Hopton, D. 2013, Monthly Notices of the Royal Astronomical Society, 427, 3196
- Krause, M., & Camenzind, M. 2001, Astronomy and Astrophysics, 380, 789

BIBLIOGRAPHY

- Longair, M. S. 2011, High Energy Astrophysics, 3rd edn. (Cambridge University Press), 880
- Luo, Q., & Sadler, E. M. 2010, *The Astrophysical Journal*, 713, 398
- Makino, N., Sasaki, S., & Suto, Y. 1998, *The Astrophysical Journal*, 497, 555
- McGaugh, S. S., Schombert, J. M., de Blok, W. J. G., & Zagursky, M. J. 2010, *The Astrophysical Journal*, 708, L14
- Mignone, A. 2014, *Journal of Computational Physics*, 270, 784
- Mignone, A., Bodo, G., Massaglia, S., et al. 2007, *The Astrophysical Journal Supplement Series*, 170, 228
- Mignone, A., Zanni, C., Vaidya, B., et al. 2015, PLUTO User's Guide
- Navarro, J. F., Frenk, C. S., & White, S. D. M. 1994, 11
- . 1996, *The Astrophysical Journal*, 462, 563
- . 1997, *The Astrophysical Journal*, 490, 493
- Nawaz, M. A., Bicknell, G. V., Wagner, A. Y., Sutherland, R. S., & McNamara, B. R. 2016, *Monthly Notices of the Royal Astronomical Society*, 458, 802
- Nawaz, M. A., Wagner, A. Y., Bicknell, G. V., Sutherland, R. S., & McNamara, B. R. 2014, *Monthly Notices of the Royal Astronomical Society*, 444, 1600
- Norman, M. L., Winkler, K.-H. a., Smarr, L., et al. 1982, *Astronomy and Astrophysics*, 113, 285
- Omma, H., Binney, J., Bryan, G., & Slyz, A. 2004, *Monthly Notices of the Royal Astronomical Society*, 348, 1105
- Oosterloo, T. a., & Morganti, R. 2004, *Astronomy and Astrophysics*, 475, 7
- Owen, F. N., & Ledlow, M. J. 1994, *The First Stromlo Symposium: The Physics of Active Galaxies*. ASP Conference Series, Vol. 54, 319
- Perucho, M., & Marti, J. M. 2007, *Monthly Notices of the Royal Astronomical Society*, 382, 526
- Perucho, M., Marti, J.-M., Quilis, V., & Ricciardelli, E. 2014, *Monthly Notices of the Royal Astronomical Society*, 445, 1462
- Scheuer, P. a. G. 1974, *Monthly Notices of the Royal Astronomical Society*, 166, 513

BIBLIOGRAPHY

- Schoenmakers, A. P. 2001, Particles and Fields in Radio Galaxies Conference, ASP Conference Proceedings, 250, 408
- Schoenmakers, A. P., de Bruyn, A., Röttgering, H., - van der Laan, H., & Kaiser, C. 2000a, Mon. Not. R. Astron. Soc, 315, 317
- Schoenmakers, A. P., de Bruyn, A. G., Rottgering, H. J. A., & van der Laan, H. 2000b, Monthly Notices of the Royal Astronomical Society, 315, 395
- Shabala, S. S., Ash, S., Alexander, P., & Riley, J. M. 2008, Monthly Notices of the Royal Astronomical Society, 388, 625
- Shabala, S. S., Kaviraj, S., & Silk, J. 2011, Monthly Notices of the Royal Astronomical Society, 413, 2815
- Shklovskii, I. S. 1963, Soviet Astronomy, 6, 465
- Soltan, a. 1982, Monthly Notices of the Royal Astronomical Society, 200, 115
- Somerville, R. S., & Davé, R. 2015, Annual Review of Astronomy and Astrophysics, 53, 51
- Springel, V., White, S. D. M., Jenkins, A., et al. 2005, Nature, 435, 629
- Stone, J. M., Mihalas, D., & Norman, M. L. 1992, The Astrophysical Journal Supplement Series, 80, 819
- Stone, J. M., & Norman, M. L. 1992a, The Astrophysical Journal Supplement Series, 80, 753
- . 1992b, The Astrophysical Journal Supplement Series, 80, 791
- Sutherland, R. S., & Bicknell, G. V. 2007, The Astrophysical Journal Supplement Series, 173, 37
- Suto, Y., Sasaki, S., & Makino, N. 1998, The Astrophysical Journal, 509, 544
- Teyssier, R. 2015, Annual Review of Astronomy and Astrophysics, 53, 325
- Tordella, D., Belan, M., Massaglia, S., et al. 2011, New Journal of Physics, 13, 043011
- Tortora, C., Antonuccio-Delogu, V., Kaviraj, S., et al. 2009, Monthly Notices of the Royal Astronomical Society, 396, 61
- Turner, R. J., Rogers, J. G., Shabala, S. S., & Krause, M. G. H. 2016
- Turner, R. J., & Shabala, S. S. 2015, The Astrophysical Journal, 806, 59
- Vernaleo, J. C., & Reynolds, C. S. 2007, The Astrophysical Journal, 671, 171

BIBLIOGRAPHY

- Vikhlinin, A., Kravtsov, A., Forman, W., et al. 2006, *The Astrophysical Journal*, 640, 691
- Vogelsberger, M., Genel, S., Springel, V., et al. 2014, *Monthly Notices of the Royal Astronomical Society*, 444, 1518
- Wagner, A. Y., & Bicknell, G. V. 2011, *The Astrophysical Journal*, 728, 29
- Wayth, R. B., Lenc, E., Bell, M. E., et al. 2015, *Publications of the Astronomical Society of Australia*, 32, e039
- White, S. D. M., & Frenk, C. S. 1991, *The Astrophysical Journal*, 379, 52
- White, S. D. M., & Rees, M. J. 1978, *Monthly Notices of the Royal Astronomical Society*, 183, 341
- Ziegler, U. 1998, *Computer Physics Communications*, 109, 111
- Zwicky, F. 1933, *Helvetica Physica Acta*, 6, 110
- . 2009, *General Relativity and Gravitation*, 41, 207